EXPERIMENTAL CHARACTERIZATION AND MULTI-SCALE MODELING OF ELECTROPLASTIC ELASTOMERS

by

Mark P. Delaney

Bachelor of Science in Physics, Allegheny College, 2006

Submitted to the Graduate Faculty of

Swanson School of Engineering in partial fulfillment

of the requirements for the degree of

Master of Science in Mechanical Engineering

University of Pittsburgh

2010

UNIVERSITY OF PITTSBURGH

SWANSON SCHOOL OF ENGINEERING

This thesis was presented

by

Mark P. Delaney

It was defended on

December 10, 2009

and approved by

Dr. William W. Clark, Professor, Department of Mechanical Engineering and Materials Science

Dr. Tara Meyer, Associate Professor, Department of Chemistry

Thesis Advisor: Dr. Lisa Mauck Weiland, Assistant Professor, Department of Mechanical Engineering and Materials Science

EXPERIMENTAL CHARACTERIZATION AND MULTI-SCALE MODELING OF ELECTROPLASTIC ELASTOMERS

Mark P. Delaney, M.S.

University of Pittsburgh, 2010

Active materials, and their subsequent use in adaptive structures, have been the subject of increasing attention recently. For example, the ability of shape memory polymers to switch between relatively low and high elastic moduli makes them attractive candidates for implementation in ambitious engineering designs requiring deformable components capable of withstanding various types of loading. However, numerous designs are hindered by the use of a thermal activation stimulus to initiate property change in SMPs. This thesis details the initial development and characterization of a new class of active materials with electrically controlled mechanical property altering characteristics. These "electroplastic elastomers" are polymer-based materials which emulate the property change features of SMPs via cross linking properties of counter ions with varying redox states. The use of an electric-based stimulus would not require a continuous supply of energy to hold state, allow for simpler stimulus control and delivery systems, and provide better user control over material state changes.

Characterization tests are performed to determine the compressive properties of cubic-based and thin film electroplastic elastomer samples prepared by the synthesis team consisting of Dr. Tara Meyer and Tianqi Pan of the University of Pittsburgh Chemistry Department. This thesis details the experimental procedures, results, and interpretations of such tests. In addition, the foundations of a multi-scale model utilizing Rotational Isomeric State theory in conjunction with a Monte Carlo methodology are adapted to simulate the effects of increased cross link density

characteristics pertaining to electroplastic elastomers. Modeling and simulation development, adaptation, and results are presented as well as methods to further adapt the model once the scope of material developmental parameters is narrowed.

TABLE OF CONTENTS

LIST OF TABLES

LIST OF FIGURES

ACKNOWLEDGMENTS

I would first and foremost like to thank my research and thesis advisor Dr. Lisa Weiland from the University of Pittsburgh. I often remind myself how lucky I am that not only did you find my application, but that you also took a chance on a physics student who had spend the previous year and a half out of school. It's almost worrisome to think where I would be had these events not transpired as such. I thank you for your patience with me as well as the occasional nudge that I am well aware I occasionally need.

I would also like to thank Dr. William Clark and Dr. Tara Meyer for not only for agreeing to be on my thesis committee, but for their aid, guidance, and suggestions relating not only to this thesis, but to the Mutable Materials project as a whole.

Finally, I would like all the members of the Mechanics of Active Materials Laboratory. In particular, Fei Gao for helping me get started when I first arrived and Rich Beblo for being there to answer any questions I have had during my first two years in the lab.

I should probably thank my family as well. After all, they have put up with me for almost 26 years now.

1.0 INTRODUCTION

As modern engineering systems have become more ambitious in terms of function and design, so too have the demands for new materials which exhibit more exotic properties than traditional engineering materials. To this end, active materials have been receiving increasing attention due to their potential implementation in such designs. Active materials such as electroactive polymers and piezoelectric materials for example, are found to be instrumental in modern energy harvesting devices due to their ability to generate electric current as a result of mechanical deformation. Similarly, shape memory polymers (SMPs), polymeric materials capable of switching between low and high moduli while preserving a "memorized" shape in response to an external stimulus, (usually thermal) have generated interest for their potential use in adaptive structures requiring deformable components. In many engineering designs however, the use of a thermal activation stimulus may be a limiting factor when exploring the implementation of SMPs. This is often due to the high energy costs associated with the heating and cooling processes of SMPs as well as the continuous energy input needed to maintain the polymer's soft state. Also, satisfactory delivery and control of the thermal stimulus may require complex or inefficient heating and cooling systems that are quite difficult to implement into the overall design.

The current research aims to facilitate creation of a new class of materials, dubbed "Electroplastic Elastomers", which combine the mechanical property changing characteristics of SMPs with an electrical activation mechanism. These materials are polymeric in nature, utilizing cross linking properties of polyelectrolytes for material stiffness control as well as redox

reactions of metal counter ions to account for changes in cross link density via manipulation of counter ion valencies. The research effort presented here is part of a collaborative effort between the University of Pittsburgh Mechanical Engineering Department (materials characterization and modeling, applications design and systems integration) and the University of Pittsburgh Chemistry Department (materials synthesis, electrochemistry and physical chemistry). As the current form of the project still resides in the preliminary stages, experimental characterization of material stiffness is of importance in order to establish a basic proof of concept, and thus is the primary focus of this thesis along with establishing the foundations of a multi-scale modeling technique for prediction of material stiffness.

1.1 THESIS OUTLINE

The following chapter presents a literature review in which different types of active materials with characteristics pertaining to the development of electroplastic elastomers are detailed. A complete description of electroplastic elastomers relating to design, functionality, theory, and applications is then presented followed by a materials characterization chapter with detailed explanations of the experimental set-ups, procedures, tests, and types of samples tested. The experimental results are then presented in the following chapter. Finally, a chapter devoted to multi-scale modeling techniques is presented with model developmental details followed by computational results and discussion.

2.0 LITERATURE REVIEW

Active or “smart” materials have garnered a considerable amount of attention in the past few decades and have a wide-ranging array of applications spreading across various fields and disciplines. While an active material is a broad term applied to any significant coupling between energy domains (electrical to mechanical, for instance), this thesis will ultimately explore the development of a novel polymer system displaying mechanical properties that are controllable with an electric stimulus. There is currently no existing literature base for this type of material. Thus, this section instead offers motivation for the creation of such a material including an overview of numerous active materials including pertinent properties and applications. Each active material detailed will include allusion to the property of interest as compared to the current developmental effort.

2.1 ACTIVE MATERIALS

Active materials, also known as smart, intelligent, or adaptive, may be defined as materials that exhibit coupling between multiple domains [1]. In other words, these materials have one or more properties that may be significantly altered in the presence of an external stimulus such as electric or magnetic fields, stress, pH, temperature, etc. The most common active materials usually cited are piezoelectric materials, shape memory materials, and electroactive polymers. Additional known types which will not be detailed in this thesis include fiber optics, magnetostrictive materials, and electrochromic materials [1].

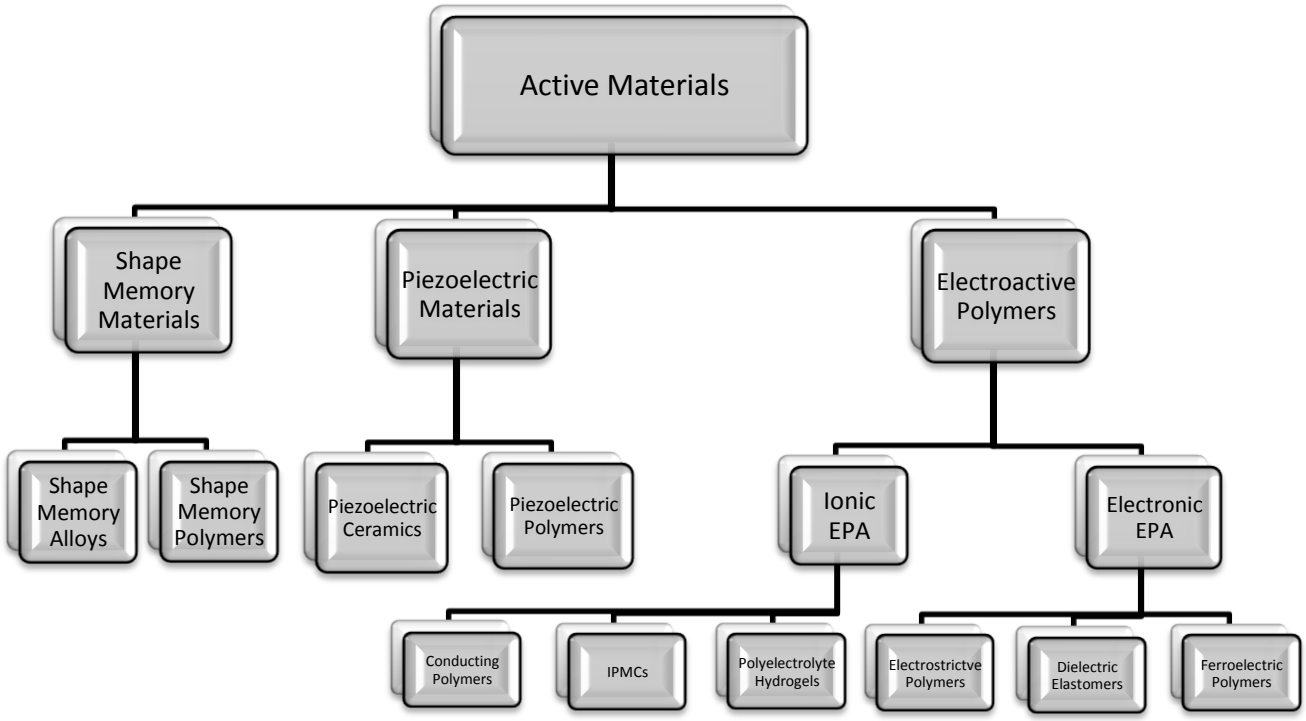

Figure 2.1: Organizational diagram of active materials presented in this thesis

2.1.1 History

The history of active materials dates back to the 1880's in France. Brothers Pierre and Jacques Curie discovered that several naturally occurring materials, in particular quartz and Rochelle salt, would produce a weak electric current when mechanically deformed. They were able to measure this signal and its strength by placing electrodes across the material and imposing varying degrees of deformation. The Curies named this effect the piezoelectric effect. It was not until years later however, that the reciprocal effect was discovered; piezoelectric materials also undergo a mechanical deformation when an electrical stimulus is applied. Applications of these materials were limited due to the weak electromechanical coupling exhibited by the piezoelectric materials available at this time in addition to the fact that precise measurements of electrical or mechanical output were not possible due to a lack of precision instrumentation [1]. It was not until the twentieth century that interest in active materials increased with direct application results including sonar development.

In the 1960's, the Naval Ordnance Laboratory discovered that an alloy composed of nickel and titanium exhibited shape memory properties, by which a sample would return to its original shape when heated after numerous induced mechanical strains. Although shape memory effects were already well known, this was the first actual demonstration of such an effect. The alloy was given the name Nitinol (for Nickel Titanium Naval Ordnance Laboratories) and was the first shape memory alloy to be put into mass production. Nitinol is currently one of the most commonly used shape memory alloys. Around the same time it was discovered that certain polymeric materials were capable of significant volume changes when placed into solutions of varying pH [2]. This breakthrough is considered to be amongst the earliest works in the field of electroactive polymers as it demonstrated that mechanical deformation could result from

chemical stimulation in such materials. In the 1970s, approximately two decades later, the first investigations into the use of electroactive polymers as actuators and sensors were conducted by Grodzinsky [3] laying the foundation for the most common applications of electroactive polymers today.

2.1.2 Types and Applications of Active Materials

As has been noted, active materials are defined as materials that exhibit coupling between multiple physical domains such as mechanical, thermal, magnetic, optical, etc. The three classes of active materials which will be detailed here are piezoelectric materials, shape memory materials, and electroactive polymers. Generally, they are considered to be the most commonly utilized active materials.

2.1.2.1 Piezoelectric Materials

Piezoelectric materials exhibit electromechanical coupling, meaning they are capable of converting energy between mechanical and electrical domains. The mechanical deformation of a piezoelectric material results in the distortion of dipoles within the material, which in turn produces a measurable electric signal. Dubbed the piezoelectric effect, the reverse is also true in that the addition of an electrical stimulus will result in an induced mechanical strain. This is known as the converse piezoelectric effect [4]. *The main properties of interest with regard to the current research are the electric-based activation mechanism as well as the existence of electric dipoles within the material.*

Electric dipoles arise as a result of polarity in the unit cell structure of piezoelectric materials, which are considered crystalline solids. This polarity produces a separation of positive and negative charges throughout the unit cell, giving rise to electric dipoles. The electric dipoles are uniformly distributed resulting in an electrically neutral material. Upon application of stress, the material will deform causing dipole rotation which upsets the electroneutrality of the material, producing a measurable charge flow. Conversely, if an external electric field is applied, the dipoles will rotate in an attempt to align themselves with the electric field. As a result of this rotation, a mechanical strain is induced. Figure 2.2 gives a detailed visual explanation of the physical nature of piezoelectric materials.

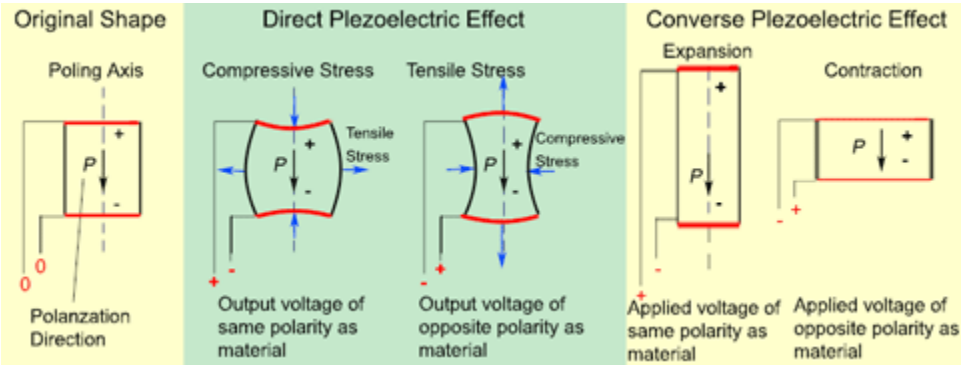

Figure 2.2: Visual representation of direct and converse piezoelectric effects [5]

Piezoelectric materials are generally durable, consisting of mostly hard ceramics. On average their elastic modulus and densities range from roughly 10 to 100 GPa and 7000 to 8000 kg/m^3 respectively. They are only capable of small strains on the order of 0.001 or 0.1% but have a rapid time response with some ceramics responding on the order of microseconds [6]. Piezoelectric materials occur naturally in the form of Rochelle salt, quartz, topaz, or berlinite. However, a majority of piezoelectric materials used today are synthetically produced, allowing

for stronger coupling properties. The most common synthetic piezoelectric material is lead-zirconate-titinate or PZT. However, single crystal PZN-PT has been garnering increasing attention in recent years [7]. While the classic definition of piezoelectricity includes reference to crystalline material structure, the notion that this term is an appropriate descriptor for certain electroactive polymers has also been gaining acceptance. The most commonly employed piezoelectric polymer is polyvinylidene fluoride or PVDF [8].

One of the most rapidly growing applications of piezoelectric materials pertains to the field of energy harvesting in which the direct piezoelectric effect, when appropriately coupled to electrical storage, is utilized to convert, capture and store electrical energy from the environment. For example, the incorporation of piezoelectric materials into clothing would allow for energy to be harnessed from simple human movement [9]. This "intelligent" clothing could power wearable devices such as phones, radios, or mp3 players, potentially eliminating the need for batteries. Rainfall is another potentially untapped source of energy. A recent raindrop energy study incorporates a smooth, flexible piezoelectric polymer PVDF subject to deformation via raindrop impact [10]. Design optimization is implemented with the goal of maximizing PVDF deformation and thus, energy production. Other energy harvesting applications of piezoelectric materials include, but are not limited to utilization of wind energy via piezoelectric material mounted on windmills, harvesting acoustic energy by mounting a PZT disc on a Helmholtz resonator, and more generally, using piezoelectric beams which produce energy when subject to bending and vibration [11 - 13].

2.1.2.2 Shape Memory Materials

Shape memory materials are capable of producing and recovering considerable mechanical strains in response to the addition or removal an appropriate stimulus (typically thermal). For the purposes of this thesis, shape memory alloys (SMAs) and shape memory polymers (SMPs) will be the materials considered. Following high degrees of deformation, a shape memory material, when stimulated, will "remember" its pre-deformed configuration and recover its original shape [14]. SMAs also exhibit the non-linear pseudoelastic effect. When an SMA is loaded beyond a critical stress, the result is a seemingly plastic deformation characterized by large strains in response to very small increases in stress. Pseudoelastic materials are able to recover this strain upon unloading. In addition, thermally activated shape memory materials are capable of transitioning between "hard" and "soft" states in conjunction with appropriate temperature levels. *This mechanical property altering characteristic is the primary function of shape memory materials motivating the current research.*

Physically, the shape memory effect and psuedoelastic properties of SMAs may be described by a solid state phase transformation. At high temperatures, SMAs exist in the stronger, austenitic phase while the lower temperature, more deformable phase is known as the martensitic phase. Transitions between austenite and martensite phases account for the shape memory and pseudoelastic properties of SMAs. Such transitions in this case are dependent only on stress and temperature [15].

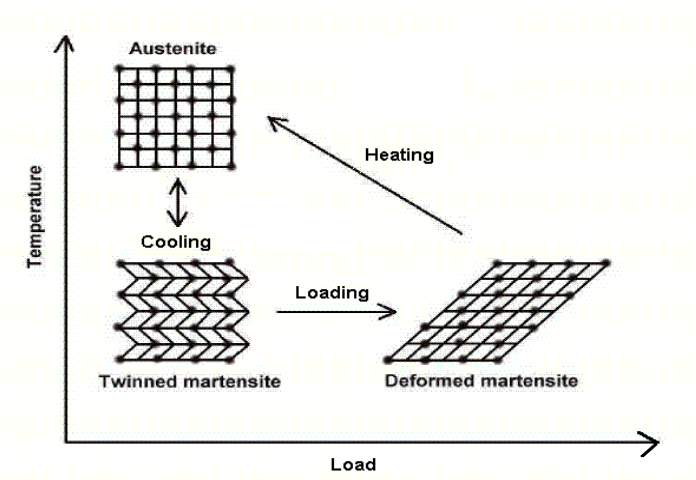

Figure 2.3: Solid state phase transitions of SMAs [15]

SMA's are generally strong materials as their elastic moduli range from approximately 10 to 100GPa with a density range of 6000 to 8000kg/m^3 [16]. In addition, they are capable of undergoing large strains (4% - 8%) compared to materials with similar mechanical properties such as piezoelectric ceramics (~0.1%). With regard to response, SMAs are limited in that they are dependent on the ability of the stimulus to initiate changes in molecular structure, a process which tends to occur more slowly with thermal stimuli. As a result, the time response of SMAs may vary on the order of milliseconds to seconds [16]. SMA applications range from aeronautical and biomedical industries, to everyday household items such as air conditioners, sporting goods, and even rice cookers [14, 17]. A majority of SMAs are nickel-titanium based, copper based, or iron based with Nitinol, a nickel-titanium based alloy being one of the most widely used today [14].

Functionally similar to SMAs, shape memory polymers (SMP's) have the ability to "remember" their original configuration after sustaining high degrees of mechanical deformation. However, in contrast to SMAs, the more compliant SMP state occurs at an elevated temperature. More specifically, SMPs operate in one of two temperature dependent phases

relative to their glass transition temperature, T_g. Below T_g, an SMP is said to be in a fixed phase wherein the polymer is very robust, capable of withstanding complex loading. When heated above T_g, the SMP will become very soft and ductile with a significantly reduced Young's modulus, as seen in Figure 2.3 In this thermally reversible phase, the polymer may be deformed into multiple configurations, any of which will be held upon cooling below T_g. If the SMP is again heated above T_g, the shape memory effect will take hold, returning the polymer to its pre-deformed configuration, provided no external load is applied.

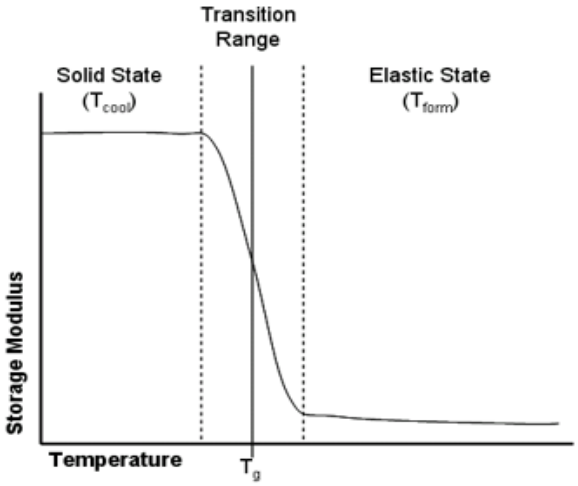

Figure 2.4: Thermo-elastic response of a typical SMP [18]

Although shape memory alloys and polymers are functionally similar, the primary differences lie within their respective base materials and physical properties. This difference accounts for the fact that SMAs are generally stronger and more durable materials while SMPs are capable of inducing much larger strains (~800%). Table 2.1 briefly details some of the contrasting characteristics of SMPs and SMAs.

Table 2.1: SMPs versus SMAs [16]

	Shape Memory Polymers (SMPs)	Shape Memory Alloys (SMAs)
Density	0.9 – 1.1 g/cm^3	6 – 8 g/cm^3
Extent of Deformation	Up to 800%	< 8%
"Hard" State Young's Modulus	0.01 – 3 GPa	83 GPa (NiTi)
"Soft" State Young's Modulus	0.1 – 10 MPa	28 – 41 GPa
Stress Required for Deformation	1 – 3 MPa	50 – 200 MPa
Generated Stress During Recovery	1 – 3 MPa	150 – 300 MPa
Recovery Speeds	< 1 s – Several Minutes	< 1 s
Cost	< $10 per lb	~ $250 per lb

Because this thesis explores development of a novel polymer, some expanded consideration of SMPs and polymers in general is appropriate. Consider first that polymers are defined as molecules (macromolecules) composed of repeating species of atoms (monomers) linked together via chemical bonding [19]. They may be categorized as either linear, branched, or network polymers in terms of their topologies. A chain of repeating monomers bonded together without branching may be described as linear while branched polymers contain side chains that are bonded to the main chain at junctions called branch points. In a network polymer configuration, these side chains may chemically bond to other polymer chains, forming cross links. The amount of cross linking in a polymer has a significant influence on its mechanical properties [19]. As one might expect, increased cross linking has been shown to result in increased polymer stiffness. Vulcanization of rubber is a classic example of this phenomenon.

When an SMP is transitioned from the more robust fixed state to the soft ductile state, existing cross-links are weakened by an activation stimulus. The weakening and/or destruction of cross links are the physical mechanisms responsible for mechanical property change in SMPs [20]. Weakened cross links allow the bonds between polymer chains to be easily stretched, thus diminishing the mechanical integrity of the polymer. In fact, in the soft ductile state, the Young's

modulus of an SMP may decrease by multiple orders of magnitude. When the activation stimulus is removed, cross links are strengthened and the stretched bonds return to their initial configurations, restoring the original configuration and modulus of the polymer [20].

Although activation stimuli for SMPs are typically thermal in nature, research efforts are currently being devoted towards alternative modes. One possibility being explored is using optical stimulation [21]. Light activated shape memory polymer (LASMP) utilizes different wavelengths of light to transition the polymer, requiring less energy to achieve transition. The search for alternative activation modes is fueled by potential shortcomings of thermal stimuli. While some SMP based devices such as cardiovascular stents are dependent on ambient temperature changes for stimulation, for others significant design issues may arise from an engineering standpoint. Effective delivery and control of thermal stimuli usually requires complex heating and cooling designs which are not energy efficient. Cooling itself is an inefficient, slow, energy expending procedure requiring bulky equipment which is often difficult to integrate into engineering systems. In addition, the high temperatures required by some SMPs may risk damage to the surrounding equipment or structure. Finally, thermally activated SMPs require a continuous input of energy to hold the thermally reversible, ductile state resulting in high energy requirements. Finding an efficient, safe and quick activation mechanism would be a key step towards further implementation of SMPs. In addition, these attributes would be desirable features of any other property changing materials, the development of which is the goal of this thesis.

2.1.2.3 Electroactive Polymers

The final class of active materials to be discussed here are electroactive polymers. Functionally similar to piezoelectric materials, electroactive polymers also exhibit electromechanical coupling. However, their differences lie within the materials respective response times, mechanical properties, and the physical mechanisms governing their electromechanical properties. Electroactive polymers are generally much softer materials capable of inducing significantly larger strains and possessing a wide range of response times varying from microseconds to minutes [8]. While a majority of active polymers are electrically responsive, there also exist numerous polymers whose activation mechanisms may include chemical, thermal, optical, or magnetic stimuli. Electroactive polymers are the only active material discussed here to be directly incorporated into the research at hand. Their primary function with regard to this thesis however, differs from previous research efforts, as will be discussed in a later section.

Electromechanical electroactive polymers are usually categorized into either electronic or ionic materials depending on the nature of their activation mechanisms, as seen in Figure 2.5. Although classification of electroactive polymers has proven to be difficult due to the wide ranging properties and coupling phenomena they exhibit, the ionic/electronic convention used in this thesis is currently well accepted and widely utilized.

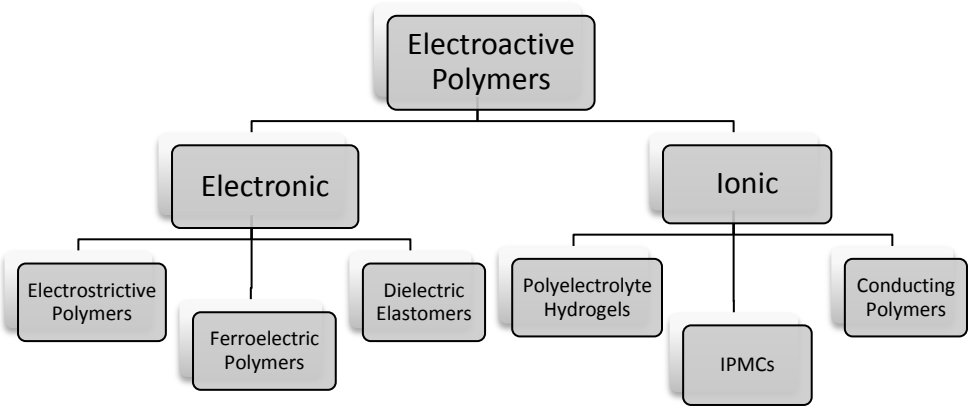

Figure 2.5: Classification of electroactive polymers

Electronic electroactive polymers are driven by electrostatic Coulomb forces. Some disadvantages of such materials are that they generally require high voltages (~150 MV/m) and often necessitate a compromise between stress and strain. However, they are capable of operating at room temperature at fast response times, and can hold induced displacements under a DC voltage for long periods of time [8]. Some examples include ferroelectric polymers, electrets, and dielectric electroactive polymers. In contrast, ionic electroactive polymers rely on the diffusion of ionic species throughout their polymer network to drive their electromechanical properties. Ionic electroactive polymers usually require very low operating voltages (as low as 1-5 V) and are capable of large bending displacements. However, the resulting force from bending actuation is relatively small and the response time is slow, on the order of seconds, compared to electronic materials. Ionic electroactive polymers also display considerable performance degradation if not kept wet and are not able to hold strain under a DC voltage. Examples include ionomeric polymer-metal composites (IMPC's), ionic polymer gels, or hydrogels, and carbon nanotubes [8].

2.2 POLYELECTROLYTES

Electroactive polymers, previously defined as active materials characterized by large strain capabilities, are typically classified into two subgroups: electronic and ionic. When employed as an active material, polyelectrolytes fall within the ionic electroactive polymer category. However, there are significant instances when this class of materials displays functionality of interest outside the realm of electromechanical materials and adaptive structures. Because manipulation of polyelectrolyte material systems will play an important role in this thesis, it is instructive to consider the broader polyelectrolyte range.

2.2.1 Definitions

Polyelectrolytes are defined as polymers or macromolecules, containing numerous ionizable groups which, when dissolved in a suitable solvent, dissociate into polyvalent macroions and an equal number of small ions of opposite charge known as counter ions [22]. The counter ions may be freely mobile within the polymer network or bound to either the general region occupied by a macroion or the charged groups of the macroion, forming ion pairs. Bound counter ions are attracted by the strong electrostatic field of the macroions, giving rise to many characteristic electrochemical properties of polyelectrolytes [23]. In addition, the fixed electronic charges on the polymer backbone chain tend to repel each other, greatly contributing to the conformation of the chain. If a small amount of charge is present, repelling forces will be minimal and a contracted, random coil conformation will result. Increasing the amount of charge will cause chain expansion and with a large enough charge quantity, a rod-like conformation may result. For example, when a solvent of low pH is added to polyacrylic acid (PAA), the

backbone chain conformation will reside in a spherical random coil configuration, with a low end radius of approximately 200Å. As the pH of the solution is increased, the chain will reconfigure itself into an extended shape with a maximum length of approximately 2500Å.

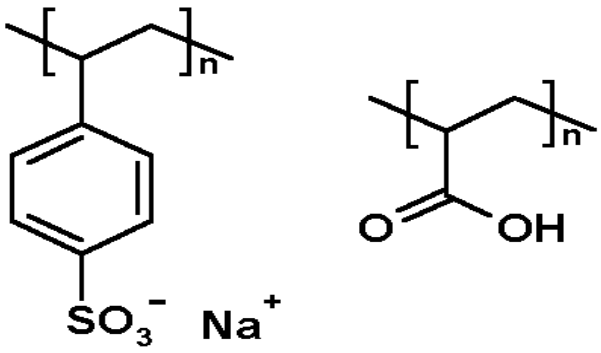

Figure 2.6: Chemical structures of negatively charged polyelectrolytes;

[poly(sodium styrene sulfonate) (left), and polyacrylic acid (right)]

Slight changes in these interactions between ionizable groups and counter ions may have a profound influence on the overall properties of polyelectrolytes, thus making them sensitive to both structure and environment [22].

The above definition identifies polyelectrolytes as polymers containing many ionizable groups. Figure 2.6 illustrates two common examples of negatively charged polyelectrolytes (PSS and PAA). However, there exists a series of materials known as ionomers which contain both electrically neutral repeating units as well as ionic groups. For the purposes of this thesis, materials described as ionomers will be included in the larger class of polyelectrolytes.

2.2.2 Ionomers

A universally accepted definition of the word ionomer has been elusive due to uncertain boundaries between materials described as polyelectrolytes and those described as ionomers. One recent distinction defines ionomers as "polymers in which the bulk properties are governed by ionic interactions in discrete regions of the material, or the ionic aggregates" [24]. In this manner, ionomers are not defined by composition, but rather by their properties. Similarly, polyelectrolytes are defined as "materials in which the solution properties in solvents of high dielectric constants are governed by electrostatic interactions over distances larger than typical molecular dimensions" [24]. Again, the differences between the two materials as defined above are expressed via physical properties as opposed to composition. However, a specific definition has yet to be universally adopted and so it is also quite common for ionomers to be categorized as a sub-group of polyelectrolytes in which a small percentage (up to 15 mol %) of ionic groups are located along the backbone polymer chains [23]. Ionomers will be defined as such for the purposes of this thesis.

The basic ionomer structure consists of a polymer chain with electrically neutral units as well as units containing pendant chains which terminate in ionic groups. The simplest types of ionomers consist of a polymer chain with a single ion placed at either end of the chain, or both. These materials are known as monochelics and telechelics respectively. More complicated structures include block copolymers and simple random copolymers as seen in Figure 2.7. Simple random copolymers make up a significant portion of ionomers which have been subjected to extensive studies due to the fact that almost any polymer can be prepared as a random ionomer as well as the substantial range of ionic species that may be attached to the polymer backbone [24].

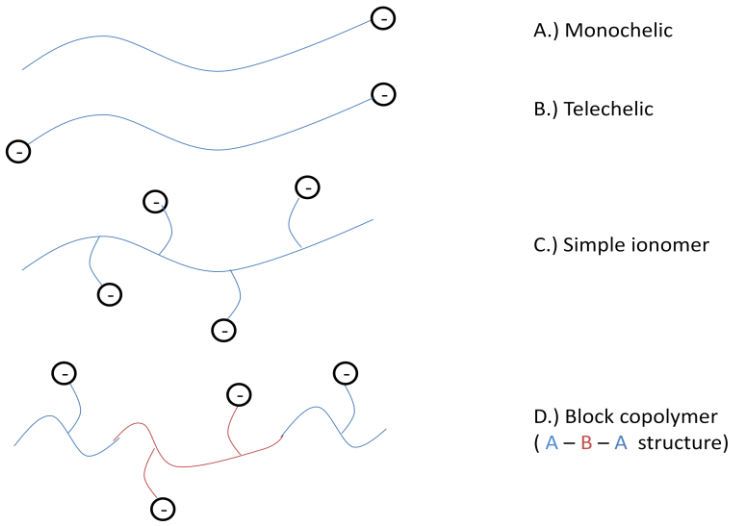

Figure 2.7: Examples of negatively charged ionomer structures

In addition to the structure of the backbone chain, the pendant ions may also be varied. The most common pendant anions used in ionomer synthesis are the carboxylates, sulfonates, and in a smaller capacity, phosphonates while a majority of pendant cations used are pyridine groups. Considering the wide range of possible backbone structures, pendant ionic groups, and available counter ions, it is clear that the ionomer field spans an enormous range of potential structural variations [24].

Since the late 1970's, numerous attempts have been made to model the structure and behavior of ionomers. Most models today still rely on the cluster morphology of a water solvated ionomer proposed by Hsu and Gierke in 1982 [25]. It has been widely accepted that the polymer chains composing ionomer materials contain a hydrophobic backbone with pendant chains that terminate in hydrophilic ionic groups. Thus, the ionomeric macromolecule consists of both a hydrophobic region occupied by the backbones of the polymer chains and a hydrophilic region comprised of ionic terminal groups. Hsu and Gierke's model proposes that when the ionomer is solvated (typically with water), the hydrophilic ionic groups cluster together with solvent

absorbed by the material [25]. These clusters are made up of pendant groups, solvent, and counter ions as is illustrated in Figure 2.8.

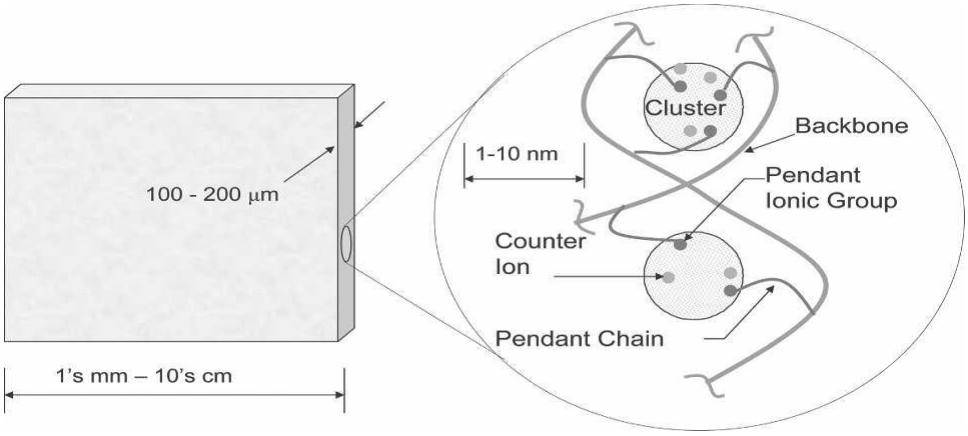

Figure 2.8: Ionic poylmer clustering morphology: Hsu and Gierke model [26].

In the original model, hydrophilic clusters are considered to be spherical, of constant radius, uniformly distributed throughout the polymer matrix, and interconnected by small channels [24]. While Hsu and Gierke's is an elastic energy based model, subsequent models have implemented additional contributing sources to the overall energy state such as electrostatic dipole interaction forces, interaction energy between the fluorocarbon matrix and the ionic clusters, and ionic cluster surface energy [27]. Some models also assume a uniform distribution of ionic side groups over spherical clusters and when counter ions are present, ion paring is assumed to be complete. In other words, each counter ion will form a pseudo-dipole with an ionic pendant group of opposite charge. However, it has also been shown via computational analysis of a single cluster that ion pairing is rarely complete which may help to explain the transport properties of ionomers [28]. In addition, these clusters may serve as backbone cross linking junctions [29]. Via bridging of multiple pendant groups, pendant group cross linking contributes to the overall bulk material stiffness, a property that has been utilized in previous models of the ionomer Nafion® [26, 29-30]. Finally, a recent ionomer model proposes that the morphology of the perfluorinated ionomer

membrane Nafion consists of long, cylindrical, parallel water channels lined with hydrophilic side groups which are outwardly stabilized by hydrophobic backbone polymer chains as seen in Figure 2.9 [31]. This model clearly stands in contrast to that to Hsu and Gierke and has garnered attention for its ability to explain potentially conflicting experimental results.

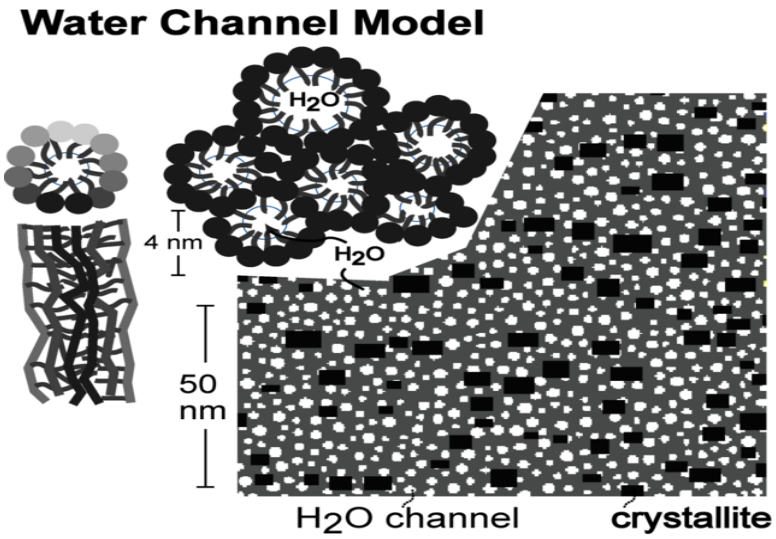

Figure 2.9: Water channel model of Nafion [31]

Per the arguments of Schmidt-Rohr and Chen, small angle x-ray scattering and small angle neutron scattering (SAXS and SANS) data obtained can only be explained by this type of morphology and not the cluster assumption made in previous models. In addition, the larger radius of the water channels predicted serves to better explain the outstanding proton conductivity and water permeability of Nafion.

Ionomer applications vary as broadly as their chemical makeup, ranging from everyday products such as packaging material, adhesives, and bulk plastic materials [24] to sensors/actuators [32] and fuel cells [33]. In the case of fuel cell applications, the property of interest is superpermselectvity.

Depending on the type of ion exchange group present, certain ionomers may be predisposed to cation or anion transport while maintaining a very low diffusivity for oppositely charged ions. This property is most notably employed in the design of polymer electrolyte membrane fuel cells (PEMFCs) such as the one presented in Figure 2.10. The key to fuel cell operation is the ability of the ionomer membrane to separate the fuel and the oxidant as well as to transport protons from the anode to the cathode. Some of the required physical properties of the ionomer membrane include good ion conductivity, flexibility in a dried state, homogeneity, impermeability towards gas, resistance to redox reactions, chemical, thermal, and hydrolytic stability, and good mechanical strength [33]. Nafion is currently the most widely used PEMFC membrane, however no current ionomer exists that fits all of the above specifications; these targets therefore serve as the basis for current PEMFC research initiatives.

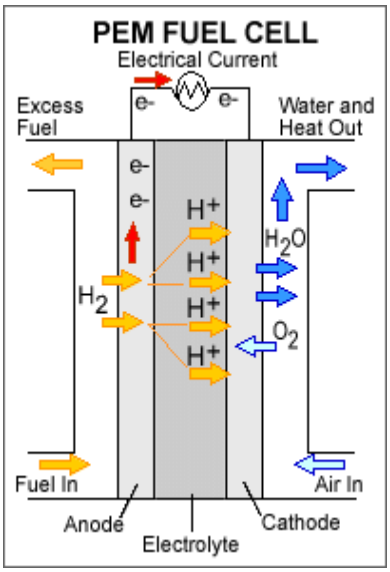

Figure 2.10: Diagram of a typical PEMFC [34]

2.2.3 Ionic Polymer Transducers

When properly electroded, ionic conduction through the sandwiched ionic polymer layer may be stimulated, resulting in the creation of "soft actuators-sensors." This configuration is sometimes described as an ionic polymer metal composite (IPMC), however this thesis will adopt the Ionic Polymer Transducer (IPT) naming convention. When a voltage drop is imposed across the electrodes, an IPT will bend (Figure 2.11). Conversely, if the IPT is deformed (most studies focus on bending) an electrical signal is generated.

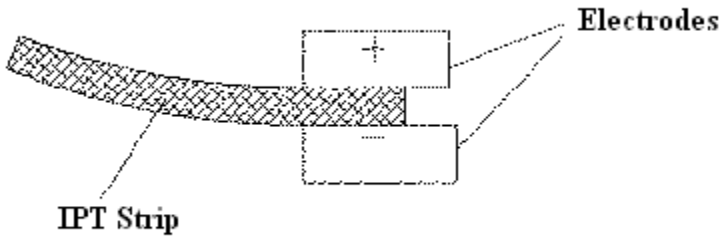

Figure 2.11: IPT sensor placed between two electrodes [35]

Electroding methods may vary [36], but most IPT reports employ noble metals such as gold or platinum at the outermost layer. Further, while a range of other ionic polymers are being explored for use in IPTs [37], most literature reports use of an active layer of ~200μm thick Nafion®. In all cases, the ionic pendant groups of the active layer are neutralized by counter ions, and most applications require that the IPT is solvated (usually with water) to facilitate ion transport [32]. However, recent research has indicated that not only are IPTs still functional in a dehydrated state, but such a condition may result in some advantageous property changes [38]. In addition, the use of suitable solvents other than water has been shown to have varying effects on

the actuation properties of IPTs. [39]. For instance, use of an ionic liquid as a solvent has been shown to expand the range of stable operation up to 10^6 cycles in open air [40].

The role of solvent in IPT sensing/actuation may ultimately have analogous impact in the electroplastic elastomers discussed in this thesis. Consider for instance that when a Nafion® based IPT is exposed to a constant, sudden electric potential (dc), it will quickly bend toward the anode followed by a slow relaxation back towards the cathode. While the details of this process may vary with counter ions, solvent type, solvent uptake, electrode morphology, ionomer backbone properties and chemical structure, as well as the nature of the applied potential [39], the transient nature of the response is directly related to the mechanism of ionic conduction though a solvent. For instance, the use of heavier more viscous solvents and/or bulkier counter ions results in slower actuation response.

2.2.4 Polyelectrolyte Hydrogels

One additional form in which polyelectrolytes often appear is that of a gel-like substance known as a hydrogel. Hydrogels, comprised of a polymer network and solvent, are environmentally sensitive materials and often respond to surrounding stimuli such as solvent pH, temperature, salt concentration, electric field, and general solvent nature, with significant alterations in size, shape, surface characteristics, and mechanical properties [41, 42] These characteristics make polyelectrolyte hydrogels intriguing materials for variety of applications such as control of microfludic flow, artificial muscle-like actuators, drug delivery, and as for use in adaptive structures as electrically activated devices. However, the difficulty in fully utilizing these materials in certain engineering designs stems from the difficulty in predicting material response to a variety of stimuli.

Most relevant to this thesis are the cross linking properties of polyelectrolyte hydrogels. The polymer backbones of these materials contain a significantly larger number of ionic functional groups than typical ionomer membranes such as Nafion®. Manipulation of the cross links formed via ionic bonding between functional groups and high valency counter ions results in mechanical property change. The possibility of actively manipulating these cross links and subsequently the mechanical properties of polyelectrolytes, make them attractive candidates for the current research from a purely mechanical perspective.

3.0 ELECTROPLASTIC ELASTOMERS

The goal of this thesis work is to facilitate development of an active material with fast, low-power mechanical property control. Upon examining the different types of active materials currently in production, it becomes clear that each class has their strengths and drawbacks. However, none meet the 'fast, low-power – mechanical property control' goal. For instance, shape memory alloys and polymers display property variation but via a high power, often slow-acting thermal stimulus. Electroactive polymers exhibit quick time response mechanisms and reversibility, but their property variation is minimal to negligible while force exertion capabilities are limited due to their soft mechanical nature. This thesis explores the development of a new class of active materials utilizing the mechanical property change ability of SMPs, and driven by an electrical stimulus akin to electroactive polymers. Going forward, these materials will be given the moniker "electroplastic elastomers".

3.1 MATERIAL PROPERTIES

3.1.1 Overview

The ability of shape memory polymers to reversibly change their mechanical properties in response to thermal stimuli has drawn interest in the past decades. While these properties have

already been applied within fields such as the biomedical and automotive industries, the use of a heat based activation mechanism is often a limiting factor when considering more ambitious applications [43, 44]. Temperature response, in which the material softens at higher temperatures and stiffens when cooled, is often a convenient mechanism for specific applications, such as the use of SMPs as cardiovascular stents. However, in many other cases, where the design is larger and mobile for instance, thermal stimulation poses significant design hurdles. The energy input for a fully reversible transition is significant and usually requires continuous energy input to retain the soft state. Moreover, if high transition temperatures are required, damage to surrounding equipment is possible. In addition, the time response to temperature change is quite slow, particularly the energy inefficient cooling process.

This thesis explores the use of an electrical stimulus as an activation mode for a synthetic material capable of switching between low and high moduli. Electrical power is relatively safe, easily generated using a number of different sources, and may be stored in batteries. Most importantly, electrical power is reversible. The on/off sequence should allow for superior state to state control while inducing a potential reversal will initiate a reverse state change. There is no need for continuous energy input to retain a stiffness state as the stimulus is only necessary during transition.

In summary, the vision for new electroplastic elastomer materials proposed will operate as follows: Starting from the higher modulus state a voltage will be applied; transitioning the material to a soft state which will be retained after the stimulus is removed. In this phase, the material can be mechanically deformed into a new configuration. Once a desired configuration is achieved, a reverse potential will be introduced and the material will return to the hard state. Again, the new shape will retain its high modulus after the electric stimulus has been removed.

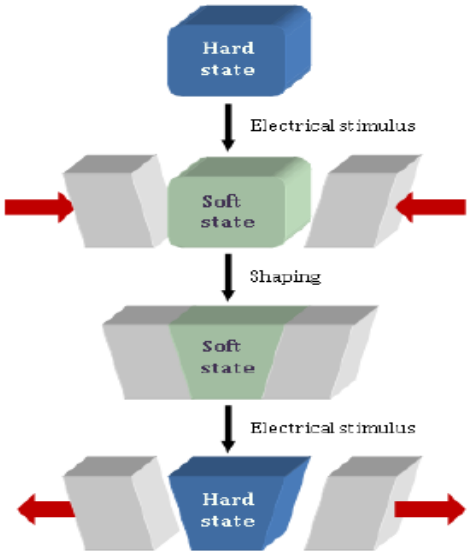

Figure 3.1: Electroplastic response of electroplastic elatomers (Figure courtesy of Meyer Group)

Essentially, the process is indistinguishable from that of SMPs save for 3 considerable differences. First, a voltage acts as the activation mechanism rather than temperature. Second, less power will be needed as the material is able to maintain both soft and hard states without requiring a continuous flow of energy. And finally, since either switching the voltage on or off as well as reversing the polarity happens instantaneously, more effective control over material state changes is possible.

3.1.2 Theory

Fundamentally, the newly proposed electroplastic elastomers emulate the mechanical property change characteristics of shape memory polymers but by exploiting the cross linking effects of counter ion and pendant groups observed in polyelectrolytes. The material design consists of a negatively charged polyelectrolyte hydrogel embedded in a polyurethane foam scaffold. Hydrogel samples currently consist of a styrene sulfonate / acrylic acid copolymer with

PEG-diacrylate used as a cross linking agent. Electroplastic elastomer synthesis is performed by Dr. Tara Meyer and Tianqi Pan of the University of Pittsburgh Chemistry Department. When the hydrogel samples are prepared with monovalent counter ions, such as sodium, they display a gellatin-like consistency and are incapable of supporting even small loads. The mechanical properties of the hydrogel are markedly improved with the addition of a foam scaffold, creating a composite material. Of central importance though, is the nature of the counter ions used. Exchanging the monovalent sodium cations with divalent metal counter ions increases the mechanical strength of the hydrogel via increased cross linking of electrolyte groups. Similarly, using trivalent cations bridges even more electrolyte groups, resulting in an even stronger composite material. Figure 3.2 provides a visual representation of this phenomenon.

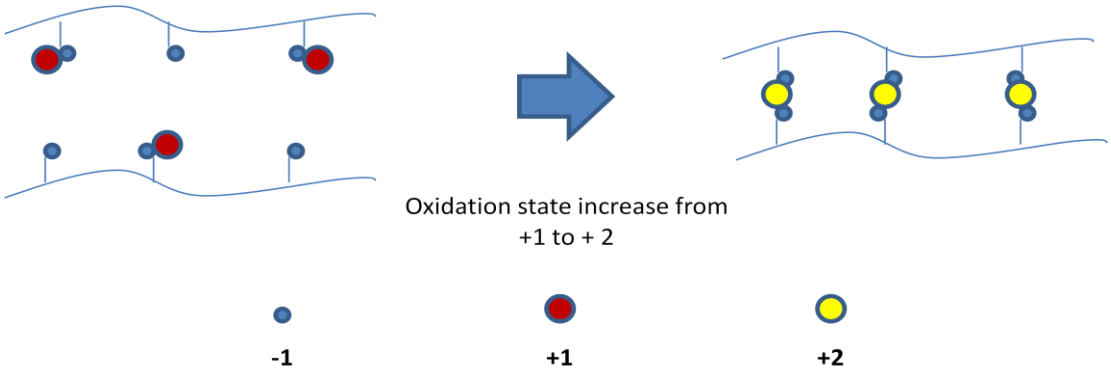

Figure 3.2: Effects of electrochemical redox reactions on polymer cross link density (Higher cross link density results in greater material stiffness)

One of the most attractive properties believed achievable by electroplastic elastomers is reversibility. This is expected to be realized via electrochemical oxidation/reduction reactions which allow the metal counter ions to switch between high and low valence states. For example, consider the composite material in its fixed, rigid state in which the metal counter ions exist at a

high oxidation state as illustrated per the Hsu and Gierke morphology in Figure 3.2. Electrochemical reduction of the metal ions lowers their oxidation state and thus, decreases cross link density. The composite's mechanical properties are in turn reduced, allowing it to be reshaped into multiple configurations by external forces. Once a desired shape is attained, electrochemical oxidation increases the oxidation state of the metal counter ions, resulting in increased cross linking and material stiffness. The new composite configuration will essentially be frozen until the cycle is initiated again. Multiple composite configurations may be achieved due to the repeatability of the redox reaction cycle.

3.2 POTENTIAL APPLICATIONS

Since shape memory polymers have seen increased attention due to their mechanical property changing capacities, it stands to reason that electroplastic elastomers would be fit for similar applications. In the medical field for instance, deformable casts and splints might be a more convenient option for patients. Similarly, cushioning material for wheel chairs, hospital beds, etc. could be reshaped at any point to increase patient comfort levels by reducing high stress points. Advances in automotive technology might include healable body panels. Portions of damaged exterior panels could be repaired by simply stimulating the material, and molding it back into the original panel configuration. Moldable seat cushions are another possibility for the purposes of increasing passenger comfort. In addition, GM is already implementing SMPs in the design of retractable air dams to improve aerodynamics and fuel economy as well as in motor-less door opening mechanisms [45]. Electroplastic elastomers would also be an attractive oprtion for such designs. Industrial applications such as robotic tools, deformable mirrors, and vibration

control devices such as isolation mounts and vibration absorbers are among just a few of exciting designs potentially made possible by electroplastic elastomers.

3.2.1 Morphing Aircraft

Consider a specific adaptive structure concept for illustration of the utility of an electrically stimulated property changing material. Recently, SMPs have been considered as a morphing skin in the design of morphing aircraft wing structures. Motivations behind morphing aircraft research seek to eliminate the need for multiple types of aircraft needed for specific missions and replace them with a single aircraft, capable of performing various types of missions. Different missions require different wing structures; aircraft design for loitering will include a large wing span and high surface area for optimally low fuel consumption while a smaller, more compact wing span is required of aircraft designed for higher speed capabilities [46].

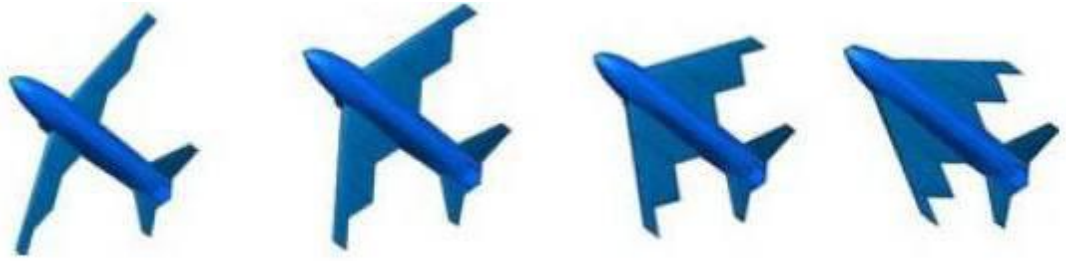

Figure 3.3: Potential configurations of morphing aircraft wing structure (Left to Right: Cruise, Loiter, Take-off, Dash) [47]

While SMPs have received attention as potential morphing skin candidates, one of the primary concerns is their use of a thermally based activation mechanism. More specifically, the long transition time as well as inefficiencies in the cooling portion of the transition cycle greatly

hinders the practicality of the morphing wing concept. If an aircraft in loiter mode discovers an enemy target, waiting 10 to 20 minutes for a complete transformation to attack mode is far from ideal. In addition, the thermal radiation resulting from a large temperature increase makes the aircraft easily detectable. Each of the above issues is readily resolved by using voltage based stimuli to initiate aircraft skin property change. Response time is drastically reduced and without any residual evidence of the transition change, the aircraft's location and actions should remain discrete.

4.0 MATERIALS CHARACTERIZATION

One of the primary objectives of this thesis is to detail the experimental work pertaining to the materials characterization of electroplastic elastomers. Specifically, the experimental value of interest is Young's Modulus which quantifies material stiffness. Both compression testing and indentation testing are employed to this end. The current chapter contains all relevant information regarding experimental tests, experimental procedures, testing apparati, as well as sample creation and preparation information.

4.1 SAMPLE CREATION AND PREPARATION

All electroplastic elastomer samples are prepared by Dr. Tara Meyer and Tianqi Pan of the University of Pittsburgh Chemistry Department. Depending on the intended test, samples are either in the form of a three dimensional cube (compression testing) or a thin film (indentation testing). All samples consist of a negatively charged polyelectrolyte hydrogel prepared via the free radical polymerization of polystyrene sulfonate, polyacrylic acid, and PEG-diacrylate. The resulting polyelectrolyte hydrogel is then soaked in an aqueous solution corresponding to a desired metal counter ion. Different metal counter ions have been shown to affect both the optical and mechanical properties of such gels as seen in Figure 4.1.

Figure 4.1: Polyelectrolyte hydrogel samples prepared with various counter ions
Left to Right: Cu(II), Ba(II), Fe(III), Co(II), Na(I) (Photo courtesy of Meyer Group)

Although the list of potential ions to be used is extensive, the current investigation only utilizes Na^{+}, Fe^{2+} and Fe^{3+} ions. Most three dimensional samples are prepared with a commercially available, high density polyurethane foam scaffold for added structural support. The scaffold is not employed in the production of thin film samples at this time.

As received, 3-D samples are cut using a razor blade to the closest visual approximation of a one inch cubic structure. All dimensions are measured using Marathon electronic digital calipers and five measurements of each dimension are taken and averaged to obtain the final, reported value. The composite samples are stored in de-ionized water as they require constant hydration and are only exposed to air during dry condition compression testing procedures and during the sample cutting process. These time periods are estimated at approximately 30 minutes and 20 minutes respectively. Latex gloves are worn at all times while handing samples with the exceptions being bare, polyurethane foam specimens.

4.2 COMPRESSION TESTING

Compression tests are performed on polyelectrolyte hydrogel-scaffold composite materials as well as blank foam scaffold samples with the aim of measuring Young's Modulus as

well as compressive strength. All tests employed adhere to an adaptation of ASTM D1621-04a Standard Test Method for Compressive Properties of Rigid Cellular Plastics in which the only deviation from the standard concerns sample size. The standard stipulates the minimum dimensions of a sample to be 2" x 2"x 1". Creation of samples of this size represents a significant burden during synthesis, especially with regard to consumption of raw materials. Per the methods described below, a series of tests on systematically smaller samples established that the requisite experimental accuracy is retained with 1'' cubic samples.

4.2.1 Compression Testing Set Up and Procedure

In order to obtain compressive modulus and strength data for a series of samples, compression tests are performed utilizing an MTI-1K (Measurement Technology Inc.) screw driven load frame along with 2.5 lb and 75 lb Transducer Technologies load cells, employed in conjunction with a non-contacting Messphysik ME46-450 video extensometer. All samples are placed in an enclosed, transparent glass cylinder to allow for submergence in solution if desired (Figure 4.2). In addition, the cylinder allows for the inclusion of conducting plates used for the application of an electric field across the sample. In place of standard compression platens, a solid plexiglass piston with a diameter slightly smaller than that of the glass cylinder (~2") is screwed into the load cell which is attached to the crosshead.

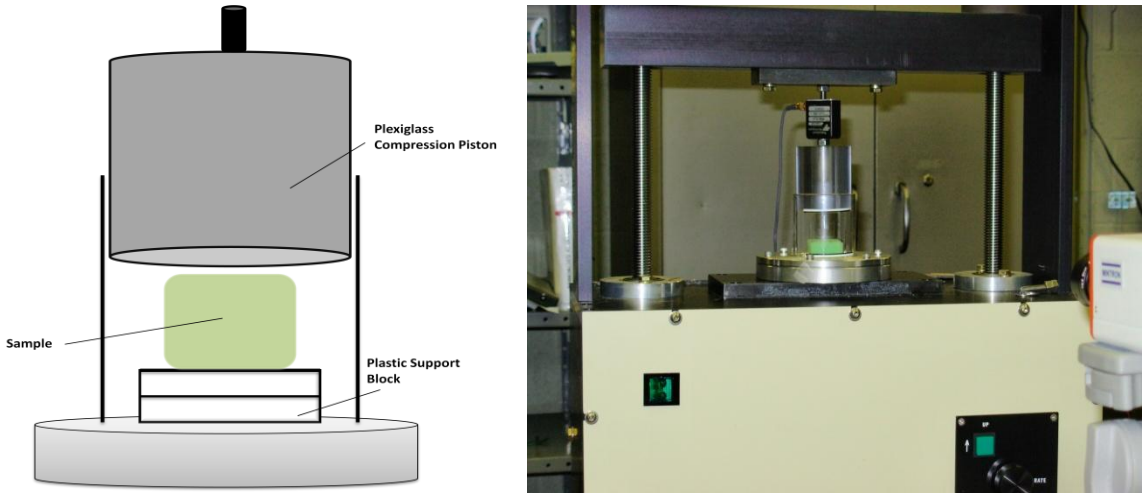

Figure 4.2: (a) Schematic of cylindrical enclosure with sample (b) Experimental set-up

While the chemically inert plexiglass is more compliant than a traditional compression platen (stiffness ranging from 1800 MPa to 3100 MPa) [48], it is significantly stiffer than the EPE samples reported here (> 30 MPa) and therefore adds negligible error. Similarly for the support block (stiffness on the order of 2 to 3 GPA) [48], which is introduced to ensure accurate video extensometry as well as allow for the application of an electric field across the sample. In the current experimental configuration, there has been no observation of significant bulging of the sample; therefore no slip surface has been introduced to date.

Movement of the piston as well as the general testing procedure is controlled via the load frame control software, capable of monitoring load and displacement. However, displacement readings are based on the movement of the crosshead as opposed to deformation of the actual sample. Conversely, the video extensometer monitors only the test sample deformation. Strips of either white or black tape, contrasting with sample color, are placed on the moving piston exactly at the point where contact is made with the sample. As a reference, an identically colored strip of tape is placed on the support block, corresponding to the bottom of the sample. The video extensometer is able to accurately measure the change in distance between the strips over

multiple, small intervals, eliminating compliance issues and leading to more accurate strain measurements compared to simply using crosshead displacement to measure strain. Resolution information for both the load frame and video extensometer is available in Table 4.1.

Table 4.1: Resolution of displacement / strain measuring equipment

Apparatus	Output Type	Resolution
MTI-1K Load Frame	Displacement	0.0000127 mm
Video Extensometer	Strain	At 50mm Axial Field of View > 0.3 µm

Compression testing begins by inputting all relevant parameters into the load frame software program SmallFrameTensileTest. These include sample dimensions, gauge length (if using cross head displacement to measure strain as opposed to the video extensometer), and crosshead velocity as determined by the standard. In addition, maximum allowable values for stress, strain, force, and displacement are entered. Whenever any of these values are reached, testing will immediately terminate. For our purposes, the maximum allowable stress and strain values are set to be large enough as to not disrupt testing. As per the standard, the maximum allowable displacement was set to correspond to approximately 15% strain and the maximum force was set to the capacity of the load cell in use. This prevents damage to the load cell due to excessive load application. All relevant pre-test parameters are listed in Table 4.2 along with the corresponding dimensions of each sample.

Table 4.2: Relevant pre test parameters input into load frame software

Sample	Dimensions (mm) [L x W x H]	Crosshead Velocity (mm / min)	Displacement (mm) [15% Strain]
HD Polyurethane Foam	29.2 x 29.5 x 20.4	2.4	3.60
LD Polyurethane Foam	27.0 x 26.5 x 24.3	2.4	3.65
Sodium Hydrogel	22.1 x 24.8 x 24.0	2.4	3.68
HD-2-Na^{+}	25.2 x 25.9 x 24.5	2.4	3.56
HD-2-Fe^{2+}	23.6 x 28.3 x 23.7	2.3	3.72
HD-2-Fe^{3+}	19.9 x 24.2 x 24.8	2.4	3.60

Once the appropriate parameters are set, the crosshead is lowered until the compression piston barely makes contact with the sample. Initially, a compression test with a small preload force, typically ~ .1 to .25 N, is performed as to ensure the crosshead zero position corresponds to a solid contact point between the piston and the sample for all subsequent tests. The preload force is then removed and testing in groups of 5 are performed (each test results in a single modulus measurement) with a window of approximately two to five minutes in between tests. It is important to note that each sample is tested five times as opposed to five different samples being tested. Collected data includes force readings, crosshead displacement, and strain (via the video extensometer) all of which may be viewed using Microsoft Excel. Compressive stress measurements can be computed by dividing all force readings by the cross sectional area of the sample. At this point, engineering stress and engineering strain are known and stress-strain curves may be plotted. However, because compression tests conducted here result in large strains, engineering stress and strain are not necessarily accurate representations of actual stress and strain due to significant changes in the dimensions of the sample during compression. This issue is resolved by calculating the true stress and true strain which take these changes in dimension into consideration. This is done using the following expressions;

$$\varepsilon_{true} = \ln(1 + \sigma_{engr})$$

$$\sigma_{true} = (1 + \epsilon_{engr})\sigma_{engr}$$

Once true stress and strain values are determined, plots are produced. Figure 4.2 illustrates a typical plot for a single test. Per the standard, the compression modulus may then be measured by taking the slope of the stress-strain curve at its steepest location as illustrated in Figure 4.3. Compressive strength is taken as the compressive stress at either the compression yield point, or at 10% strain if no such yield point exists as stipulated by the standard.

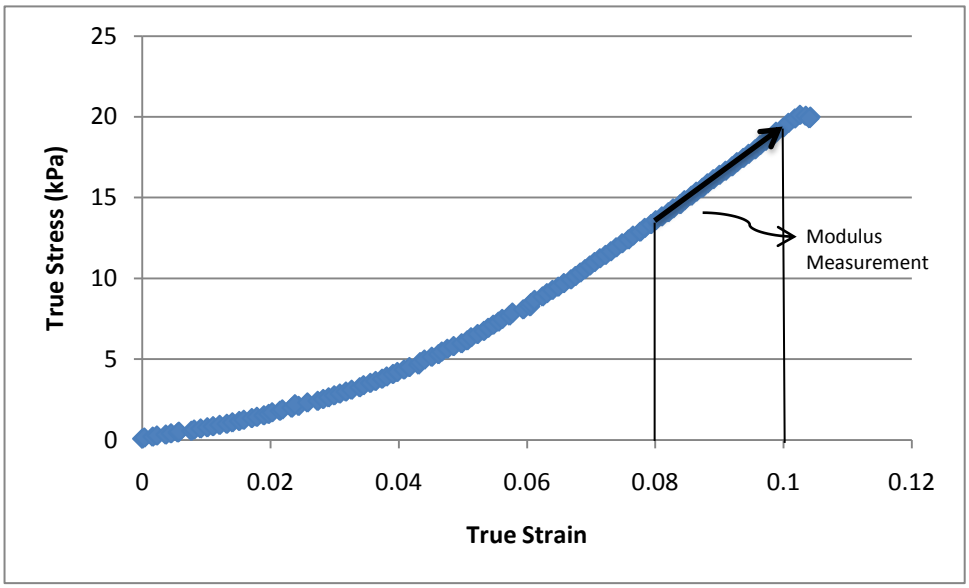

Figure 4.3: Typical stress-strain plot produced via compression testing

4.2.2 Sample Dimensions

In order to determine suitable sample dimensions, the compression modulus of a low density foam scaffold with dimensions of 1.5” x 1 .5” x 1” is measured three times and averaged. The sample dimensions are then modified to 1.25” x 1.25” x 1” and another series of three measurements are performed. Finally, the sample is cut into a one inch cube and a third series of

compression modulus measurement are taken. As Table 4.1 below indicates, the effects related to reducing the sample size are acceptable for the current study.

Table 4.3: Compression testing results; single foam w/systematic dimension reduction..

Sample Dimensions	Compression Modulus	Standard Deviation
1.5” x 1.5” x 1”	58kPa	2kPa
1.25” x 1.25” x 1”	55kPa	5kPa
1” x 1” x 1”	57kPa	4kPa

4.2.3 Samples Tested

For bookkeeping purposes, a simple naming convention is developed for different sample types. Each sample is prepared with a polyurethane foam scaffold, classified as either high density (HD) or low density (LD), along with one of three types of counter ions, Na^{+}, Fe^{2+}, and Fe^{3+}. Thus, the naming convention goes as follows:

(Scaffold Type)-2-(Counter Ion Type)

So, a sample prepared using a high density foam scaffold along with Fe^{2+} counter ions would be documented as HD-2-Fe^{2+}. In all, compression tests were performed on six types of samples consisting of high and low density bare scaffolds (HD and LD), sodium hydrogel, high density sodium hydrogel composites (HD-2-Na^{+}), high density iron (II) hydrogel composites (HD-2-Fe^{2+}), and high density iron (III) hydrogel composites (HD-2-Fe^{3+}). Of notable importance are the mechanical properties of the iron composite samples. As previously stated, electroplastic elastomers are being developed as a class of synthetic materials capable of switching between

high and low moduli. This is to be achieved via reversible redox reactions of metal counter ions within the polymer network. Higher valencies corresponding with the oxidation state of the metal ions should increase cross linking within the material, resulting in increased material stiffness. Currently, HD-2-Fe^{2+} samples correspond to the electroplastic elastomer "soft" state while the higher valent HD-2-Fe^{3+} samples will be the "hard" state. Thus, the discrepancies in moduli between the two are of interest.

4.2.4 "Wet" versus "Dry" Testing Conditions

All scaffold-hydrogel composite samples obtained from the synthesis team required constant hydration. They were stored in de-ionized water and only during testing were they left entirely exposed to the environment. However, over the course of multiple compression tests, it was observed that significant amounts of water were "squeezed" out of the sample as a result of sample compression. To this end, "wet" tests were employed in which compression tests are carried out with the sample completely submerged in de-ionized water inside the glass cylinder. The purpose of these tests was to ascertain if the loss of water has any effect of the mechanical properties of the composite sample. Tests performed under such conditions are documented as "wet" tests while compression tests with no external hydration are referred to as "dry" tests.

4.2.5 Electric Current Tests

The electrochemical process responsible for stiffness affecting oxidation and reduction of the metal counter ions has yet to be fully developed. To enable development, electric current tests may be performed to ascertain whether additional electric coupling effects are displayed. To

this end, HD-2-Na^{+} as well as HD-2-Fe^{3+} samples are tested with a small current ranging from 1 to 4 mA passing through them. Figure 4.4 includes a diagram of the experimental set up.

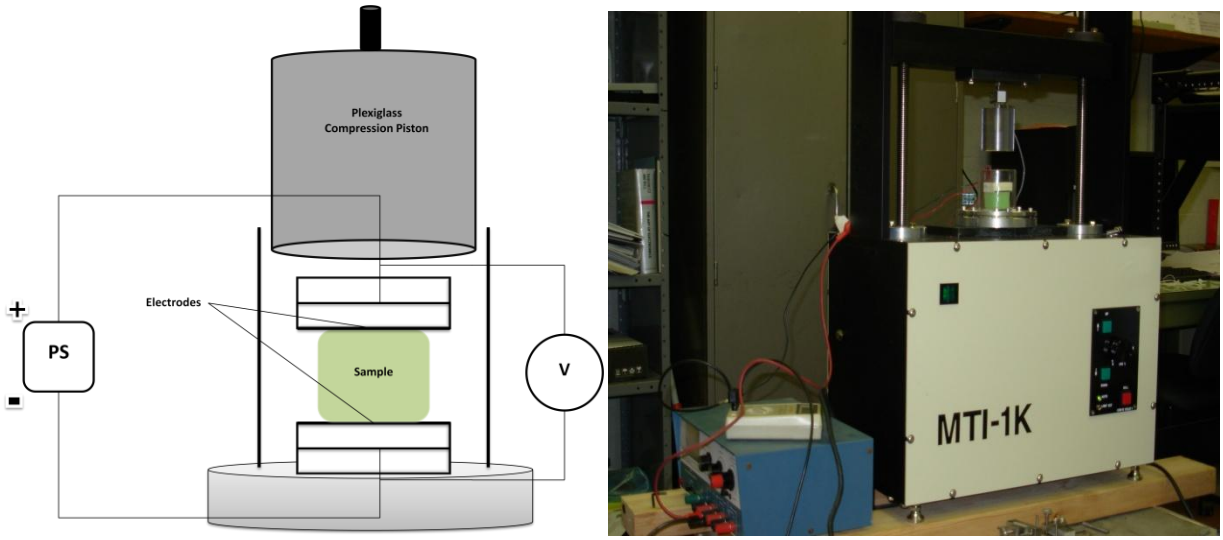

Figure 4.4: (a) Wiring schematic for inclusion of electric current (b) Current test set-up

Tested samples are sandwiched between conducting plates containing small sheets of aluminum cut to be slightly larger than the cross sectional area of the sample. To enhance electrical conductivity as well as establish strong adhesion between the electrodes and the sample, conducting epoxy is used. Each plate is wired to a Heathkit tri-power source as well as a digital multimeter set to read the voltage drop across the electrodes. Coupling is then assessed by simultaneously performing compression tests in the same manner as previously detailed.

Unless otherwise noted, a set of compression tests are initially conducted with the current turned off in order to establish a baseline. The current may be switched on or off as well as varied in magnitude, and compression tests are conducted in sets of five under each condition to produce modulus measurements. Further details of the experimental procedure may be found in Appendix A1.

The compression test procedure includes introduction of a preload, which when continually applied, results in additive deformation prior to each test. This is not preferred because it is incorrectly suggestive of a linear increase in stiffness with subsequent tests. However, this trend is consistent across all electrical current tests, and therefore enables the needed comparative assessment. Consideration of the results in this light reveals that no significant differences can be observed between compression tests with or without the addition of electric current. The result of these tests is that no additional electrical coupling is displayed by electroplastic elastomers. This is encouraging as it will tend to simplify the required electrochemical process development. Details of this null result are available in Appendix A1.

4.3 INDENTATION TESTING

Following the initial rounds of compression testing, it was determined that an additional intermediate test of thin film samples would be introduced. Thin film samples require less material to produce as well as allow for different types of testing procedures such as tensile and indentation tests. In addition, the foam scaffold is not included in the preparation of thin film samples, reducing sample complexity. More importantly, indentation tests allow for a series of "quick" tests. These tests allow the testing of multiple samples prepared using different chemical formulas and thus, provide an indication of which chemical formulas are worth pursuing as 3-D materials for compression testing. In addition, indentation tests yield information regarding sample uniformity. The following sections will detail the process of indentation testing as well as the design and use of the newly created multi-sample indenter (MSI).

4.3.1 Multi Sample Indenter (MSI) Design and Use

Created as part of a senior design project at the University of Pittsburgh under the guidance of Dr. William Clark, the MSI is an instrument capable of performing quick indentation tests on as many as 16 different samples in a time interval of approximately half a minute per test. The primary purpose of the MSI is to accelerate the rate of characterization testing, effectively replacing time consuming compression or tensile testing for large sample quantities. The MSI operates as follows; single indentations of 3mm are made in each sample and corresponding force readings are recorded using LabView-based DAQ software on a nearby computer. From these measurements, an approximate value for Young's Modulus can be extracted using the sample thickness, indentation area, and peak force.

$$E = \frac{\sigma}{\epsilon} = \frac{F/A_0}{\Delta L/L_0} = \frac{FL_0}{A_0 \Delta L} \tag{4.1}$$

F is the peak force, L_o is the sample gauge length, ΔL is the indentation length, and A_o is the original cross sectional area through which the force is applied. In this instance, it is the cross sectional area of the indentation rod. The peak force value is calculated by taking the average value of the 5 largest force readings. Next, the thickness of the each sample, as well as the area of the testing probe tip is measured. Sample thickness is measured by taking the average of 5 measurements using Marathon electronic digital calipers. Once these values are collected, Equation 4.2-1 can be employed to obtain an experimental value for Young's Modulus. A photograph of the MSI is illustrated in Figure 4.4.

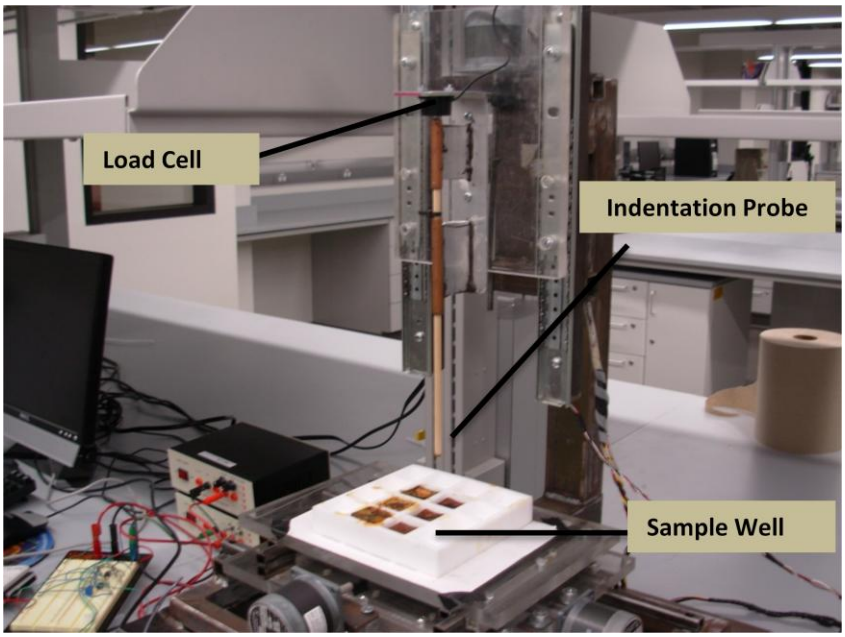

Figure 4.5: The multi sample indenter (MSI)

The MSI is effective for quickly identifying promising formulations, as it can detect relative property variations. However, the MSI is not capable of measuring accurate stiffness values; rather it tends to over-predict material stiffness. For the purposes of the current research, this is not an issue due to the fact that appropriate variation in material stiffness from sample to sample is accounted for via MSI measurements. For instance, based on compression test data, it is known that HD-2-Fe^{3+} composite samples are stiffer than HD-2-Fe^{2+}. Although not nominally accurate, MSI measurements of HD-2-Fe^{3+} are indeed significantly higher than those for HD-2-Fe^{2+}. These types of results are consistent across all samples. Another limitation of the MSI is related to its lower bounds on stiffness measurement. Softer samples which are incapable of supporting the weight of the indenter rod are often subject to pre-test deformation. To address this, the stainless steel indenter rod may be replaced with a lighter, wooden rod. Because the MSI is an in-house, custom device, a detailed operation procedure is provided in the appendix.

4.3.2 Thin Film Samples Tested

Experimental efforts utilizing the MSI are conducted in two phases. The pre-testing phase I goal is to ascertain whether the MSI functions as needed, as well as to define any necessary final design modifications. Four samples are tested: sodium hydrogel films, sodium hydrogel-scaffold composite films, iron (III) hydrogel films, and iron (III) hydrogel-scaffold composite films. Per compression testing on similar cubic samples, the material samples above are listed in order of increasing stiffness. The first series of indentation tests seeks to confirm that the MSI is able to "sense" the relative stiffness variations across these samples. In addition, three control foams are tested for the purposes of investigating the long term operating capabilities of the MSI as well as a typical statistical spread amongst measurements of a homogeneous material. After many continuous indentation tests, it is necessary to confirm that the MSI operates in a consistent manner and that the number of measurements considered as outliers are minimal.

Upon completion of Phase I, Phase II MSI studies are employed as a material development tool. This portion of the research aims to determine optimum chemical formulas used during synthesis. To this point, iron (II) and iron (III) films with varying time periods of chemical cross linking during synthesis are tested using the MSI.

5.0 EXPERIMENTAL RESULTS AND DISCUSSION

Compression tests are performed on multiple samples within each class. It is important to note that any one reported experimental measurement and standard deviation is the result of a series of compression tests performed on a single sample. For instance, the reported compression modulus for the class of samples tagged as HD-2-Fe^{3+} is the result of compression tests performed on one specific sample as opposed to being measured across multiple samples under the HD-2-Fe^{3+} moniker.

5.1 COMPRESSION TEST RESULTS

All compression tests are conducted at room temperature, with each sample subjected to both “wet” and “dry” conditions. A time period of between two and five minutes is allotted between tests depending on how long the sample takes to return to its original configuration following compression. It should be noted that none of the three composite samples demonstrated a yield point on their stress-strain curves as the steepest portions of their stress-strain curves consistently increase with increasing strain. For the purposes of consistency across such samples, compression modulus measurements are calculated as the slope between 8% and 10% strain. Also, per the standard, compressive strength is measured as the true compressive stress at 10% strain. Based on the general nature of their stress-strain curves, compression

moduli measurements for bare, polyurethane foam samples are calculated using slopes ranging from 0% to 3.5% strain (in increments of 2%), depending on the particular curve. Again, because there is no clear compressive yield point present, the compressive strength is taken as the compressive stress value at 10% strain. Each reported measurement is the mean result of a series of five compression tests on a single sample. Statistical errors in the form of 95% confidence intervals are presented using Student's t-distribution. In all, compression test results are reported for six different samples including polyurethane foams (no hydrogel present), sodium hydrogel, and three hydrogel-scaffold composites.

5.1.1 "Dry" Compression Test Results

Table 5.1 provides a summary of all compression tests conducted on six different samples: low density bare polyurethane foam, high density polyurethane foam, sodium hydrogel, and hydrogel-scaffold composites prepared with monovalent sodium counter ions (HD-2-Na^{+}), divalent iron (II) counter ions (HD-2-Fe^{2+}), and trivalent iron (III) counter ions (HD-2-Fe^{3+}). The compression modulus is provided along with the 95% confidence interval calculated using Student's t-distribution. Plots from all compression tests conducted over the course of the project are presented in the appendices.

Table 5.1: Compression test results; "dry" condition

Sample	Compression Modulus (E)	95% Confidence Interval	Compressive Strength ($\sigma_{10\%}$)
HD Scaffold	65.4 kPa	± 4.1 kPa	3.4 kPa
LD Scaffold	42.0 kPa	± 2.9 kPa	2.4 kPa
Sodium Hydrogel	14.0 kPa	± 0.5 kPa	0.9 kPa
HD-2-Na^{+}	182 kPa	± 2.0 kPa	14.9 kPa
HD-2-Fe^{2+}	287 kPa	± 6.0 kPa	19.6 kPa
HD-2-Fe^{3+}	22.4 MPa	± 0.5 MPa	0.83 MPa

Figure 5.1 contains stress-strain curves generated by compression tests on both high density and low density polyurethane foam. Examination of the plots shows that the steepest portion of the stress-strain curve, where the compression modulus is measured, occurs in the range of 0% to ~3.5% strain. The compressive strength is measured as the true stress value at 10% strain or the maximum attained strain if 10% is not reached.

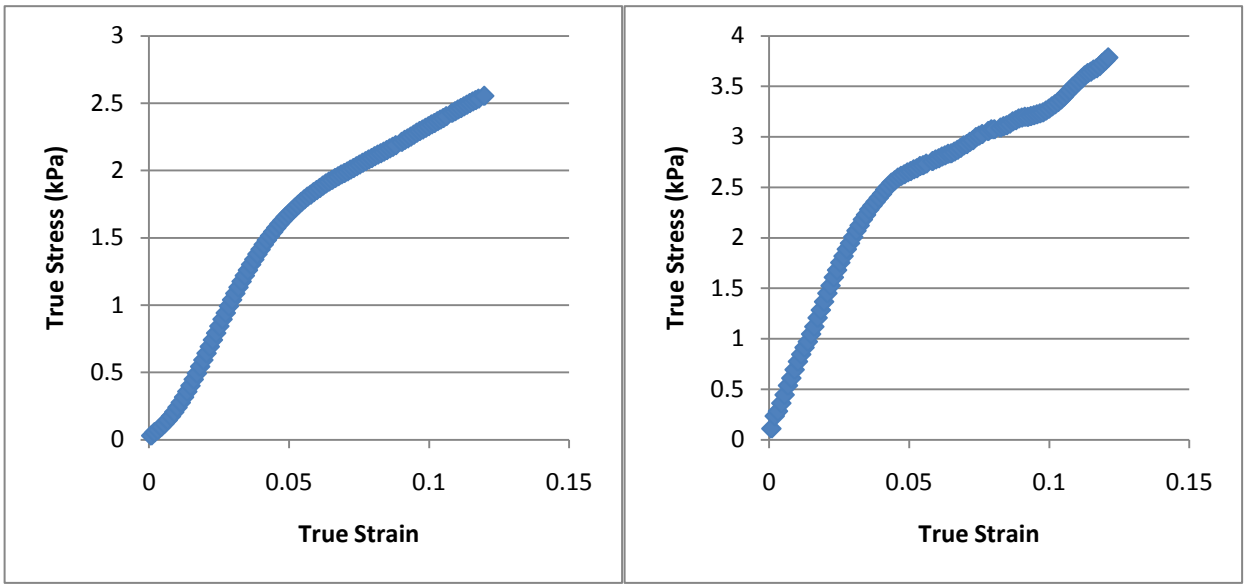

Figure 5.1: Typical stress-strain curves; low (left) and high (right) density polyurethane foams

The compression tests performed on the sodium hydrogel and the sodium-hydrogel composite (HD-2-Na^+) are worth noting as they demonstrate the effect of adding a foam scaffold to form a composite material. Figure 5.2 illustrates a side by side comparison of their stress-strain curves.

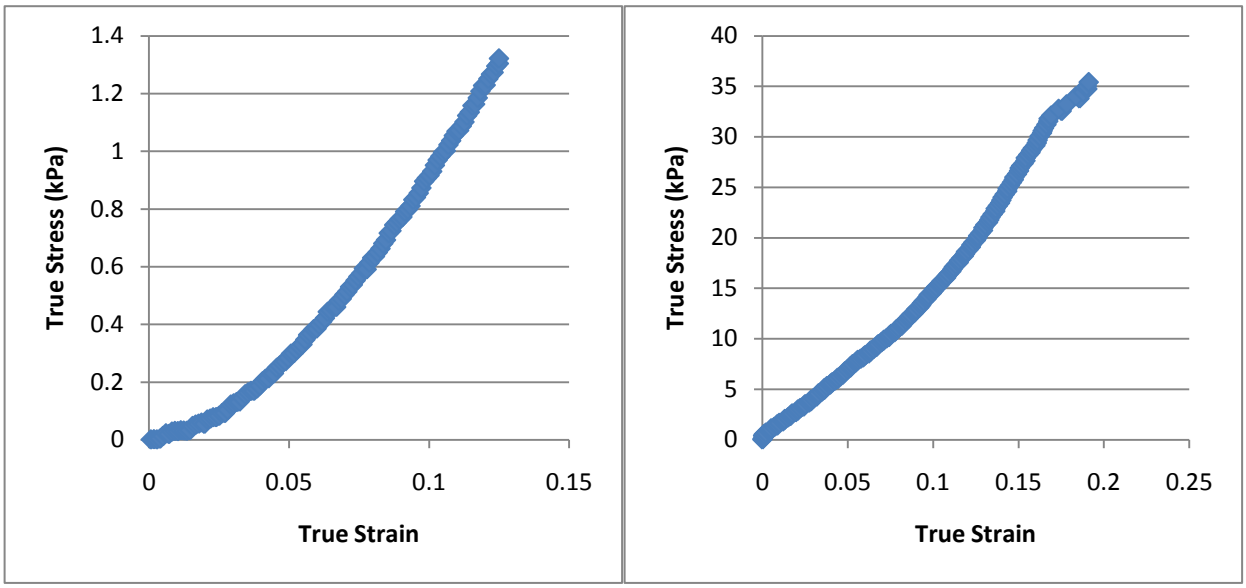

Figure 5.2: Typical stress strain curves; sodium hydrogel (left) and HD-2-Na^{+} (right) samples

Note that unlike the plots displayed in Figure 5.1, the hydrogel and hydrogel-scaffold composite samples in Figure 5.1 exhibit increasing slope with increasing strain.

Figure 5.3 contains stress strain curves generated via compression tests on composite samples HD-2-Fe^{2+} and HD-2-Fe^{3+}. These results are of interest in that they represent the "soft" and "hard" states of electroplastic elastomers respectively. More detailed comparisons will be presented in an upcoming section.

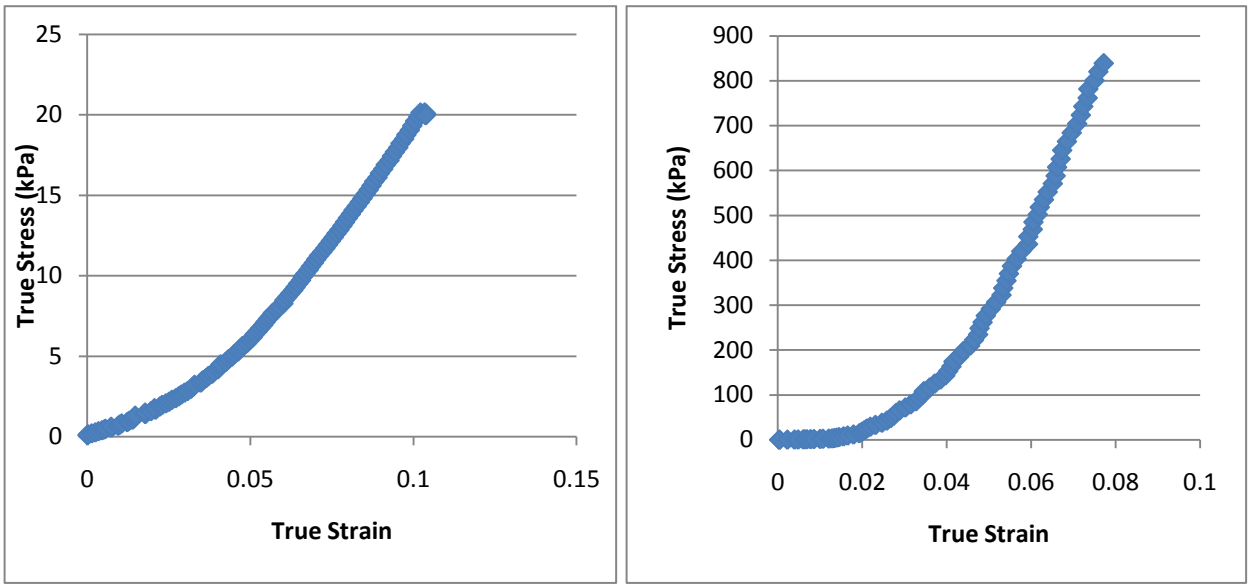

Figure 5.3: Typical stress-strain curves; HD-2-Fe^{2+} (left) and HD-2-Fe^{3+} (right) composites

5.1.2 "Wet" Compression Test Results

As has been noted, the "wet" compression testing procedure differs from its "dry" counterpart in that the sample is completely submerged in deionized water during compression. Because the stress-strain plots are similar to those presented in the previous section, and all trends, calculations, etc. apply to both conditions, all such plots are presented in the appendices. Table 5.2 displays the results of all compression tests conducted under the "wet" condition. It should be noted that the sodium hydrogel is not included. The sodium hydrogel samples fractured before multiple compression tests could be conducted while the sample is entirely submerged in water, rendering a significant measurement of the compression modulus impossible.

Table 5.2: Compression test results; "wet" condition

Sample	Compression Modulus (E)	95% Confidence Interval	Compressive Strength ($\sigma_{10\%}$)
HD Scaffold	49.7 kPa	± 2.9 kPa	2.5 kPa
LD Scaffold	27.5 kPa	± 3.4 kPa	1.7 kPa
HD-2-Na^{+}	138 kPa	± 4.0 kPa	10.6 kPa
HD-2-Fe^{2+}	278 kPa	± 4.0 kPa	16.4 kPa
HD-2-Fe^{3+}	26.3 MPa	± 1.1 kPa	0.82 MPa

5.1.3 Single Sample Transition Results

HD-2-Fe^{2+} and HD-2-Fe^{3+} samples correspond to the "soft" and "hard" states of electroplastic elastomers respectively. Reported compression modulus data have resulted from testing independently prepared samples produced directly by the materials synthesis process. However, in order to establish a basic proof of concept, it is paramount that an increase in stiffness be observed in the same sample, beginning in the lower oxidation state (HD-2-Fe^{2+}) and transitioned to a higher oxidation state (HD-2-Fe^{3+}). To demonstrate this, iron (II) ions are chemically oxidized by the Meyer group by placing the sample an acidic bath of $S_2O_8^{2-}$ after a baseline compression modulus is determined. For a single HD-2-Fe^{2+} sample, a compression modulus of 155 ± 5.1 kPa is measured using the procedure as previously detailed. Following oxidation of the iron (II) metal cations to iron (III), the same sample yields a compression modulus of 1.33 ± 0.2 MPa, demonstrating an order of magnitude increase within the same sample. Figure 5.4 offers a direct comparison of the resulting stress-strain curves for each state of the material.

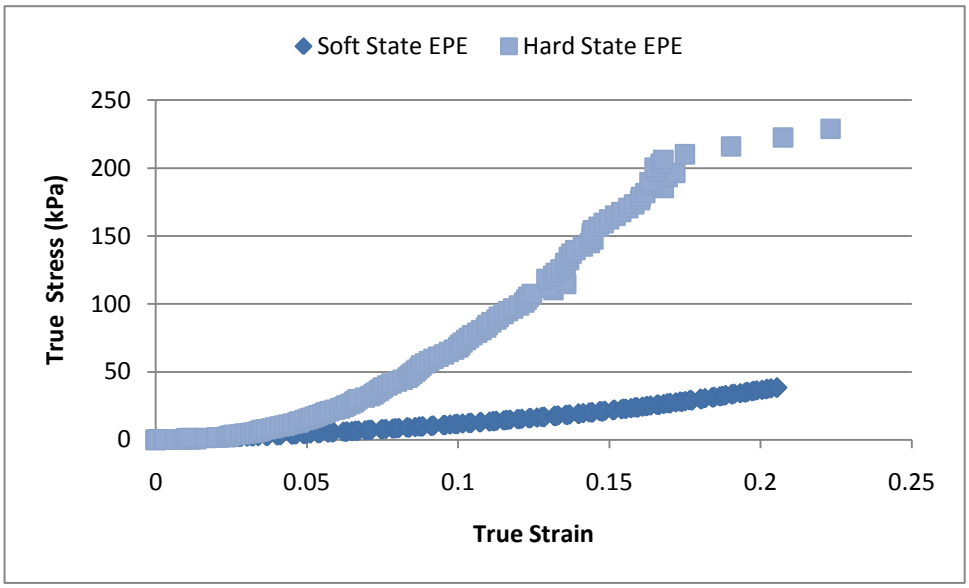

Figure 5.4: Stress-strain curves for single sample compression tests

5.2 COMPRESSION TEST DISCUSSION

This section presents discussion of the experimental results of load frame compression testing including experimental interpretations, challenges, and limitations. Testing includes "wet' and "dry" as well as "soft" and "hard" cases. For reference, Tables 5.1 and 5.2 contain summaries of all the results to be discussed in this section. As summarized in these tables, compression tests are performed on six samples for the "dry" case: low and high density polyurethane foam, hydrogel prepared with sodium counter ions, and hydrogel-scaffold composite samples prepared with sodium, iron (II) and iron (III) counter ions. The sodium hydrogel sample is not included under the "wet" testing conditions.

5.2.1 Foams

As expected, the compression modulus of the high density polyurethane foam exceeds that of the low density foam. The goals of foam testing are to (1) aid in the selection of a desirable scaffold (i.e. eliminate candidates that display ratcheting, residual stress remaining after loading) and (2) establish baseline properties of the selected scaffold. Table 5.1 shows that the high density polyurethane scaffold has the most desirable mechanical properties and thus, is selected for use as an electroplastic elastomer scaffold.

5.2.2 Scaffold Composites

Introduction of the hydrogel to the high density foam (scaffold) results in a stronger composite material. This fact is demonstrated as the compression modulus of the scaffold-sodium hydrogel composite is greater than both of its high density foam and sodium hydrogel components. Such a result is in itself interesting as traditional composites theories suggest that the hydrogel composite stiffness should be bounded by the stiffness of its constituents.

It has been established that increasing cross link density of polymeric materials tends to increase mechanical properties. The underlying hypothesis of this investigation involves the relationship between counter ion valency and cross link density. It is believed that higher counter ion oxidation states should enhance cross linking through the increased bridging of ionic functional groups. Because of the relationship between cross link density and the mechanical properties of polymeric materials, larger compression moduli measurements corresponding to composite samples prepared with higher valency counter ions will indicate that cross link density is indeed being controlled in such a manner. Evidence to support this conjecture is found within

the comparison of the three composite materials. The modest, near two-fold increase in compression modulus for the divalent HD-2-Fe^{2+} sample relative to the monovalent HD-2-Na^{+} sample (182 kPa versus 287 kPa) does support the hypothesis that cross link density has been increased with the monovalent to divalent counter ion exchange. However, more pertinent is the near 100-fold increase in observed compression modulus from composite samples prepared with iron (II) cations and iron (III) cations. The significantly higher modulus observed in the composite prepared with iron (III) lends further validity to the suggestion that cross link density is being controlled during material synthesis.

5.2.3 Hydration

All compression tests are performed under both “wet” and “dry” conditions. It is observed that when a sample is under compression in the dry condition, water is squeezed out of the hydrated composite. The inclusion of the wet condition, in which a sample is completely submerged during compression, seeks to determine if the measured mechanical properties of a material are affected by the loss of water during compression. Consistent across four of the five samples is the trend that wet compression modulus measurements are only slightly smaller than their dry counterparts. This result would indicate that the removal of small amounts of water during dry compression conditions is inconsequential with regard to mechanical testing. Such a result would be expected under most conditions.

However, an interesting observation is noted regarding the HD-2-Fe^{3+} sample. The compression modulus measured under the wet conditions is notably larger than that measured without exogenous water (22.4 MPa versus 26.3 MPa). An examination of the generated stress-strain curves does not reveal any significant variations in curve shape. However, such an increase

is not likely attributable to simple experimental error. Although this phenomenon only occurs in one of five tested samples, the roughly 17% increase in stiffness is significant enough to explore in future experimental works.

5.2.4 In-Sample Transition

For the purposes of establishing a proof of concept, it is imperative that a quantifiable increase in mechanical properties be observed within a single sample, transitioned from the soft to hard state via oxidation of iron metal counter ions. This idea encompasses the second phase of the experimental characterization process presented here and the subsequent investigation yields the key preliminary result. Upon chemically oxidizing the iron (II) counter ions in an HD-2-Fe^{2+} composite to iron (III) in an acidic bath of $S_2O_8^{-2}$, an order of magnitude increase in compression modulus is observed (155 kPa to 1.33 MPa) within the sample. Although the latter of these measurements is less than that observed in the independently prepared samples, the order of magnitude increase is significant enough to establish a basic proof of concept. An obvious observation is the difference in compression modulus between the independently prepared composite and the oxidized composite. This may be attributable to the amount of iron (II) in the sample that has been successfully oxidized. At the current time, the amount of iron (II) sites remaining after chemical oxidation is not known. In the event that considerably more iron (III) sites exist within the independently prepared composite than the oxidized sample, the subsequent loss of cross link density would explain the discrepancy in measured compression modulus. In addition, all prepared samples are soaked in a solution corresponding to the desired counter ion. Due to the nature of this process, the amount of iron initially in each sample is unknown and

such differences in the amount of iron present from sample to sample may also account for such a discrepancy.

5.3 INDENTATION TEST RESULTS

Indentation tests conducted using the multi sample indenter (MSI) may be categorized into two separate phases. The first phase is geared towards the developmental effort of the MSI. These initial tests are designed to ensure that the MSI is operating in a desirable manner by measuring the correct relative stiffness values of different materials. The second phase of indentation tests is more in tune with the scope of the project, as thin film samples produced by the Meyer group with different cross linking times are tested. The results of each phase will be presented in two separate sections.

5.3.1 MSI Development Test Results

Initially, indentation tests are performed on materials of known relative stiffness. Due to the fact that the MSI is a new untested apparatus, it is necessary to confirm that the measurements it yields are reasonable. To this end, four film samples listed in order of increasing modulus as confirmed by compression tests on cubic samples (hydrogel, hydrogel + scaffold, hydrogel + iron (III), and hydrogel + iron (III) + scaffold) are subject to indentation tests. Table 5.3 summarizes the results of the MSI tests as compared to load frame results (benchmark). It should be noted that no modulus is measured for the hydrogel film sample. This is due to the lack of mechanical integrity of the gel. Unable to support the weight of the probe, the sample

was completely punctured before the indentation test could be administered, rendering an experimental measurement impossible. It is valid to state however, that the hydrogel film would have the lowest compression modulus of the four samples due to the fact that it was the only film unable to support the probe.

Table 5.3: Preliminary indentation test results versus compression test results

Sample	Indentation Modulus (Thin Film Sample)	Compression Modulus (One Inch Cube Sample)
Hydrogel	-	0.01 MPa
Hydrogel + Scaffold	0.06 MPa	0.05 MPa
Hydrogel + Iron (III)	1.2 MPa	0.13 MPa
Hydrogel + Iron (III) + Scaffold	1.9 MPa	0.48 MPa

As Table 5.3 indicates, the moduli measured by the MSI do coincide with expected trends. This fact demonstrates that the MSI is capable of correctly distinguishing between samples of differing mechanical properties. Upon this determination, the MSI is then able to be utilized in the manner best suiting the current research.

Next, indentation tests are performed on three different foam samples including vinyl, silicon, and buna-N-foam. Such tests enable introduction of control samples in that they are homogeneous from a mechanical standpoint and maintain a known, constant sample thickness. In practice, these foam samples of known stiffness are placed among any batch of samples currently undergoing testing to periodically confirm that the MSI has retained appropriate calibration. The results of these foam tests, as well as an explanation of conclusions drawn, are presented in the appendices.

5.3.2 Device Implementation Results

Indentation tests are performed on iron (II) and iron (III) thin film samples corresponding to the soft and hard states of electroplastic elastomers and produced by the Meyer group. The variable of interest to this point is the time allowed for cross linking during the material synthesis process, which is varied between two and 10 hours. All results are tabulated in Table 5.4.

Table 5.4: Indentation test results

Sample	Cross Linking Time	Indentation Modulus	95% Confidence Interval
Iron (II)	2 Hr	95 kPa	± 27 kPa
Iron (II)	4 Hr	160 kPa	± 110 kPa
Iron (II)	5 Hr	220 kPa	± 44 kPa
Iron (II)	8 Hr	330 kPa	± 130 kPa
Iron (II)	10 Hr	240 kPa	± 100 kPa
Iron (III)	2 Hr	280 kPa	± 36 kPa
Iron (III)	5 Hr	280 kPa	± 25 kPa
Iron (III)	8 Hr	240 kPa	± 33 kPa

5.4 INDENTATION TEST DISCUSSION

5.4.1 MSI Development Discussion

Initial indentation tests performed on samples of known relative stiffness are conducted with the primary purpose of ensuring that the measurements produced are reasonable and constructive. The results, as tabulated in the previous section, are evidence that the MSI is capable of reasonably detecting relative differences amongst materials from a mechanical

properties standpoint. This conclusion is reached by observing that for significantly different sample stiffness cases, the indentation modulus trends produced by the MSI display the same ranking of increasing stiffness as measured by compression testing. For cases with similar properties, the more time and resource intensive compression tests will be required. However, the design purpose of expedited assessment of relative stiffness is satisfied by the MSI.

It should be noted that the measurements produced by the MSI are not necessarily accurate from a nominal standpoint. Examination of Table 5.3 reveals that the MSI tends to over-predict material stiffness. The primary source of error is thought to be the rudimentary procedure (peak force measurement) employed to extract modulus measurements. Using a single stress point to calculate the modulus of a material is the equivalent of calculating the slope of a line passing through the origin and the point (σ_{peak}, ε). An examination of stress-strain curves in section 5.1.1 shows that for electroplastic elastomers, the slope of the curve increases with subsequent increases in strain. Indentation tests achieve strain values of ~80% - 100%, which are significantly larger than the 8% - 10% ranges utilized for compression tests. If the stress-strain curves illustrated in section 5.1.1 were to be extrapolated to such high strain values, corresponding modulus measurements would be more likely to agree with those generated via indentation tests. This result is acceptable due to the fact that the purpose of the MSI is to quickly obtain relative modulus measurements. The motivation includes (1) a dramatically reduced time required to characterize mechanical properties and thus, expedite the synthesis feedback and (2) reduce synthesis material demands through the creation of smaller samples.

Another observation worth mentioning is the issue of pre-test deformation. The MSI operates in such a manner that a small force (the weight of the indenter probe) is applied to the the sample as initial contact is made. During the first phase of testing, this resulted in significant

pre-test deformation in softer samples such as the hydrogel and hydrogel + scaffold thin films. As Table 5.3 shows, no measurement is given for the hydrogel film as it is not mechanically strong enough to support the weight of the rod. Similarly, significant deformation is observed for the hydrogel + scaffold film. In order to minimize this effect, the original stainless steel rod is replaced with a wood rod as the probe. Following the substitution of the wooden probe, the measurement ability of the MSI is not otherwise affected and the amount of pre-test deformation is noticeably reduced in softer samples. All indentation tests results reported, aside from the initial four tests from the design phase, make use of the wooden probe as opposed to the stainless steel probe. Another design modification is that the wooden probe has a rounded tip in contrast to the flat tip of the steel probe. The intent is to minimize stress concentrations associated with discrete edges, as this may also have contributed to the hydrogel sample damage.

5.4.2 MSI Implementation Discussion

The second phase of indentation testing investigates the effect of cross linking duration during the synthesis process on the resulting material properties. Hydrogel films prepared with either iron (II) or iron (III) counter ions are produced with varying cross linking times, and indentation tests are conducted. As the results in Table 5.4 indicate for the case of iron (II), generally longer cross linking times coincide with a mechanically stiffer material up to a certain point. In fact, up to eight hours, the trend is approximately linear, after which stiffness appears to degrade with additional time allotted to cross linking. While it is possible that the degradation is within experimental error (i.e. not significant), the iron (III) samples also display degradation for longer cross linking times. Moreover, the iron (II) samples do not otherwise display particular sensitivity to cross linking times considered here.

In addition, it is pertinent to note that the discrepancy in mechanical properties between iron (II) and iron (III) samples is quite small compared to that observed in compression testing of cubic samples. This is because the sample preparation methods in the current study do not overtly seek to optimize stiffness, rather the intent is to assess the effects of more subtle variations in synthesis strategies.

6.0 MULTI-SCALE MODELING

This chapter describes the motivation and development of a multi-scale computational model for material stiffness predictions. Specifically, the model presented applies rotational isomeric state (RIS) theory in combination with a Monte Carlo methodology to ultimately predict material stiffness. This strategy has previously been employed to successfully predict local stiffness of the ionomer Nafion® as pertaining to the net backbone contribution, [26, 29, 30] where the stiffness contributions of semicrystalline regions and the hydrophilic clusters are not taken into account. However, it can be shown that reasonable values are achieved by applying a rule of mixtures scheme as described by Gao and Weiland [26].

The current model is based on the parameters associated with fully hydrated, sodium-exchanged Nafion® and is adapted to simulate the increased cross link density as is relevant to this thesis. An overview of the methodology is presented followed by an analysis of the modeling and computational development. The results are then offered followed by a discussion and interpretation.

6.1 OVERVIEW

As advances in modern computing have led to increases in computing power, multi-scale modeling has become more prevalent as a research tool. More specifically, predictions obtained

via modeling methods may serve to explain or confirm experimental results, motivate further studies, or save time and resources consumed by experimentation. In the context of this thesis, the development of a multi-scale model aims to provide additional insight into the relationship between increased cross linking and bulk material stiffness in polymeric materials; more specifically, ionomers.

Many multi-scale modeling efforts with regard to ionic polymers seek to discover information regarding the mechanisms responsible for their transduction properties. A majority of these models are based on the idealized cluster morphology proposed by Hsu and Gierke [25] which is detailed in Section 2.2.2. Because ionomer stiffness has been shown to both directly and indirectly affect transducer response [28, 49], modeling methods for the prediction of ionomer stiffness as a function of composition (ionomer and counter ion type as well as solvation type and level) have become increasingly desirable [26].

The current modeling effort utilizes rotational isomeric state (RIS) theory which, as described by Flory [19], has been employed to build atomic scale models of polymer chain conformations for the purposes of predicting mechanical response trends and material properties of polymeric materials. Fundamentally, RIS theory states that any given bond within a polymer chain is restricted to a discrete number of possible rotational bond angles corresponding to low energy states and dictated largely by the interaction with the nearest-neighbor bond. Based on a non-Gaussian theory of rubberlike elasticity proposed by Curro and Mark [50], RIS theory is applied in conjunction with a Monte Carlo methodology to computationally generate polymer chain conformations and thus, compute a large number of end-to-end distances between cross link junctions (*r*-values). These *r*-values may then be used to estimate a probability density

function (PDF) for cluster interaction distance. Using this PDF, various statistical methods may be utilized to predict material response.

Like previous ionomer modeling efforts by Weiland et al., the current modeling effort applies RIS theory in a similar manner to recent polymer composite particle inclusion works also utilizing the Mark-Curro approach [51, 52]. In this case, the inclusion volumes are taken to be hydrophilic clusters which act as backbone cross linking junctions under certain conditions [30]. In order to ensure stable stiffness predictions, the current model applies the same methodology previously proposed for the generation of backbone chain lengths of sufficient length [26].

The mechanical response of fully hydrated 1200 equivalent weight (EW) Nafion® containing Na^+ is considered where ion exchange is assumed complete. Like the aforementioned particle inclusion investigations, the backbone polymer chain conformation is excluded from occupying any volume allocated to a hydrophilic cluster. For the current case, such inclusions are distributed as proposed by the Hsu and Gierke model of ionomer morphology [25]. Pendant chains communicate with these hydrophilic clusters via attachment points which are assumed to approximate cross linking junctions as illustrated in Figure 6.1a. These attachment points coincide with an end point for the end-to-end distance between cross linking junctions (*r*-values). Previous modeling efforts propose the distance between a pendant chain and the closest hydrophilic cluster must be no more than the length of the pendant chain for a successful communication point. The current model utilizes this assumption as a baseline as Figure 6.1b illustrates. A 100% communication rate is then implemented, corresponding to an increased cross linking state within the polymer.

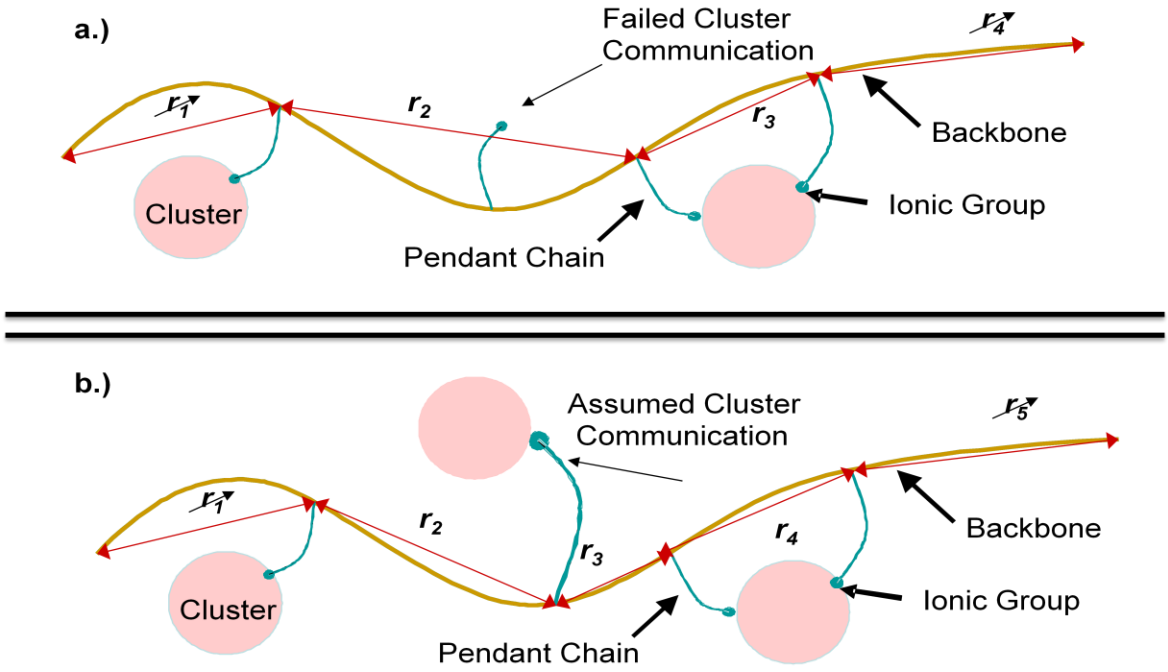

Figure 6.1: End-to-end length *r* distances; (a) baseline and (b) assuming 100% communication

6.2 MODELING AND COMPUTATION DETAILS

Simulation of a polymer backbone chain requires information on numerous parameters such as chemical structure, bond lengths, counter ion type, as well as statistical weight matrices which yield information regarding rotational angles between bonds. Population of these parameters may be non-trivial. Meanwhile, electroplastic elastomers continue to evolve via consideration of a broad range of options. Thus, this chapter demonstrates the generalized phenomenon of increased cross linking in an ionic polymer for a well defined case. As electroplastic elastomers approach a narrow set of material design chemical components, the approach may be adapted to specific experimental cases.

6.2.1 Simulation of polymer chain conformation

Figure 6.1 depicts the repeating monomer unit of Nafion where $(CF_2CF)(CF_2CF_2)_n$ constitutes the polymer backbone chain, and SO^{-3} represents the hydrophilic pendant chain ionic group, capable of interacting with hydrophilic clusters.

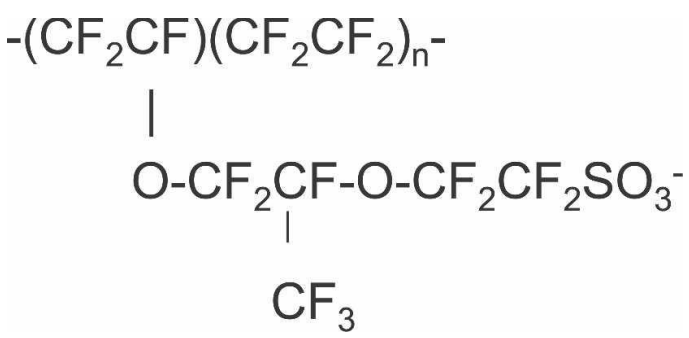

Figure 6.2: Chemical structure of a single Nafion monomer [26]

The current modeling effort considers the 87/13 composition of Nafion® in which there are approximately 13 (CF_2CF) groups for every 87 (CF_2CF_2) groups comprising the total length of the polymer backbone chain. Thus the value of *n* is approximately 7, illustrating that the bulk of the polymer backbone consists of (CF_2CF_2) or polytetrafluoroethylene; more commonly known as PTFE or Teflon. This assumption allows for the incorporation of statistical weight matrices corresponding to PTFE for prediction of backbone rotational bond angles as dictated by RIS theory. In the current simulation, the monomer displayed in Figure 6.1 is repeated *m* times, with $m = [50, 80]$, as determined for stable stiffness predictions by Gao and Weiland in terms of appropriate chain length [26]. The actual values of *n* are determined using a discrete probability distribution in the range $n = [5, 11]$ with a mean of approximately 7 to account for physically realistic variability as displayed in Table 6.0.

Table 6.1: Discrete probability distribution of *n* values

N	Probability
5	0.1
6	0.2
7	0.3
8	0.2
9	0.1
10	0.05
11	0.05

The current simulation places polymer chains on a three dimensional cubic grid measuring $(5000\ \text{Å})^3$. Firstly, the spherical, hydrophilic clusters described by Hsu and Gierke [25] are evenly distributed upon the grid, analogous to a cubic crystalline structure. The size of each cluster is determined by the cluster volume fraction which is directly related to the counter ion type (different counter ion types will result in different cluster sizes). Using the volume fraction for sodium counter ions, reported by Bar-Cohen [8] to be 30%, the cluster radius (21Å), and the size of the grid, the center-to-center cluster separation distances easily follow. These are all the necessary parameters to describe and place the distribution of spherical clusters.

Upon assignment of the cluster distribution, the generation of a polymer chain begins by randomly placing a PTFE bond on the grid. If the bond location coincides with a volume occupied by a cluster, new coordinates are generated and the bond is placed again. For PTFE, the carbon-carbon bond length and in-plane bond angle are fixed at $l_{C\text{-}C} = 1.53$ Å and $\theta = 116°$ respectively as seen in Figure 6.2 where φ_j is the out-of-plane rotational bond angle.

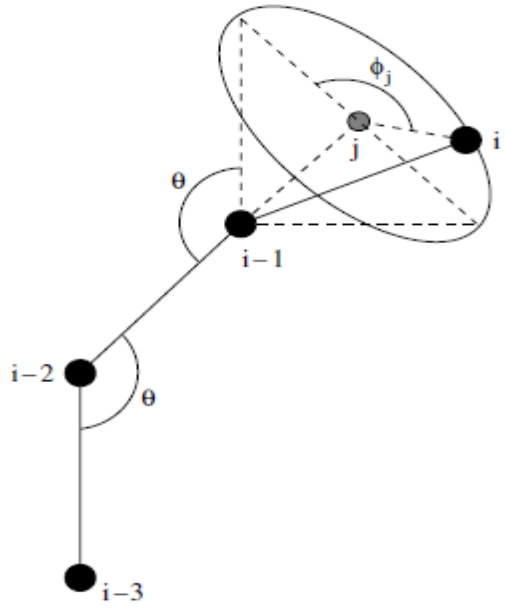

Figure 6.3: Spatial Geometry of Nafion chain [29]

Placement of all backbone chain bonds beyond the initial two is accomplished by a series of translations and rotations to a local coordinate system as described by Matthews el al [29]. Once the bond is properly placed, the inverses of these rotations and translations are applied in order to return the newly placed bond to the global coordinate system.

Since the simulation is performed within a three dimensional space, two angles are required of the placement of all bonds. Unlike the in-plane bond angle which is held constant throughout the simulation, the second, out-of-plane, rotational angle is determined by statistical weight matrices which yield probabilities of various low energy angular conformations based on previous bond angles as dictated by RIS theory. These matrices are utilized for all bond placements with the exception of the initial bond and those corresponding to pendant chains. For PTFE, three- and four-state statistical weight matrices have been studied. Due to ability of the four-state model to describe the helical chain coiling behavior in both PTFE and Nafion, it is ultimately preferred to the three-state model. In this case, the four possible out-of-plane bond

angles are +15°, +120°, -120°, and -15° corresponding to the trans+, gauche+, gauche- and trans- conformations respectively. The four-state statistical weight matrices applied are as follows;

$$U_2 = \begin{vmatrix} 1 & 0 & 0 & 0 \\ 0 & \sigma' & 0 & 0 \\ 0 & 0 & \sigma' & 0 \\ 0 & 0 & 0 & 1 \end{vmatrix} \qquad U_3 = \begin{vmatrix} 1 & \sigma & 0 & \omega \\ 1 & \sigma & \sigma\beta & 1 \\ 1 & \sigma\beta & \sigma & 1 \\ \omega & 0 & \sigma & 1 \end{vmatrix}$$

$$U_k = \begin{vmatrix} 1 & \sigma & 0 & \omega \\ 1 & \sigma & 0 & 0 \\ 0 & 0 & \sigma & 1 \\ \omega & 0 & \sigma & 1 \end{vmatrix} \qquad U_N = \begin{vmatrix} 1 & \sigma' & \sigma' & \omega \\ 1 & \sigma' & \sigma'\beta & 0 \\ 0 & \sigma'\beta & \sigma & 1 \\ \omega & \sigma & \sigma' & 1 \end{vmatrix}$$

(6.1)

The rows and columns of each matrix are indexed in the order of out-of-plane rotational angles listed above. After the first bond is placed using the constant in-plane bond angle 116°, the orientation of the second bond is specified by U_2, the third bond by U_3, and the last bond by U_N. Placement of all other bonds is dictated by the matrix U_k. However, there exist two conditions in which the matrices are overridden which will be detailed shortly.

The above matrices are not directly utilized in bond angle prediction; they must be normalized first. In order to employ these matrices in the determination of out-of-plane bond angles corresponding to low energy states, a similarity transformation

$$Q_j = \varepsilon_{j,1}^{-1} D_{j,1}^{-1} U_j D_{j,1} \tag{6.2}$$

where $\varepsilon_{j,1}$ is the largest eigenvalue of U_j and $D_{j,1}$ is the diagonal matrix of the elements of the eigenvector associated with $\varepsilon_{j,1}$, must be performed on each statistical weight matrix U_j. The resulting conditional probability matrices are then directly implemented into the model.

$$Q_2 = \begin{vmatrix} 1 & 0 & 0 & 0 \\ 0 & 1 & 0 & 0 \\ 0 & 0 & 1 & 0 \\ 0 & 0 & 0 & 1 \end{vmatrix} \qquad Q_3 = \begin{vmatrix} 0.6552 & 0.2137 & 0 & 0.1310 \\ 0.4017 & 0.1310 & 0.0655 & 0.4017 \\ 0.4017 & 0.0655 & 0.1310 & 0.4017 \\ 0.1310 & 0 & 0.2137 & 0.6522 \end{vmatrix}$$

$$Q_k = \begin{vmatrix} 0.7295 & 0.1246 & 0 & 0.1459 \\ 0.8541 & 0.1459 & 0 & 0 \\ 0 & 0 & 0.14589 & 0.8541 \\ 0.1459 & 0 & 0.1246 & 0.7295 \end{vmatrix} \qquad Q_N = \begin{vmatrix} 0.2781 & 0.4829 & 0.2144 & 0.0245 \\ 0.3203 & 0.5562 & 0.1235 & 0 \\ 0 & 0.6263 & 0.0556 & 0.3181 \\ 0.1261 & 0.1095 & 0.4863 & 0.2781 \end{vmatrix}$$

(6.3)

Again, the rows and columns of each matrix are indexed in the order +15°, +120°, -120°, and -15°. These conditional probability matrices are used in the simulation to choose out-of-plane rotational bond angles based on the rotational state of the previous bond. They are utilized in the following manner: Assume that the last bond of a backbone chain is being placed where the previous bond angle is +15°, corresponding to the trans+ state. The simulation will go to the first row of the conditional probability matrix Q_N and a random number is generated between 0 and 1. If the previous bond angle was +120º, the simulation would select the second row of the matrix and so on. Assume a value of 0.45 is selected. Since (0.45 > 0.2781), the +15º angle will not be selected. At this point, the subsequent number 0.4829 is added to 0.2781 to give 0.761. Since (0.761 > 0.45), the angle corresponding to the second column, +120º, is selected.

As previously stated, there are two conditions in which the above matrices are overridden while placing a bond. The first exception occurs when placement of a bond coincides with a hydrophilic cluster. In such a scenario, another random number is generated and applied to determine an alternative low energy bond angle. If all possible out-of-plane bond angles result in cluster coincidence, the previous bond is replaced with another low energy conformation per the method of Gao and Weiland [26]. This allows for the generation of longer backbone chain

lengths by avoiding pre-mature chain termination while generating a more realistic distribution of *r*-values. Physically, these measures are consistent with the reality that a hydrophobic backbone chain will reconfigure itself upon solvation to an alternative low energy state in order to avoid a hydrophilic region [30]. A second case in which the statistical weight matrices are overridden occurs during placement of a bond corresponding with a pendant chain connection point. The selected angle, in this case, minimizes the distance to the nearest cluster which is physically representative of the terminal ionic group tending to a hydrophilic region (i.e. the nearest cluster). Selection of the bond angle in this manner also describes the effect that the hydrophilic clusters have on polymer chain conformation. Because the angle corresponding to a minimum cluster distance is always chosen, it follows that in the presence of clusters, the polymer chain is going to tend in their direction.

It is assumed that a pendant chain ionic group successfully communicates with a cluster if it is placed within 8 Å, the estimated length of the extended pendant chain, of the nearest cluster. Figures 6.1 and 6.4 illustrate multiple *r*-values occurring within a single backbone polymer chain. Due to the fact that the first and last *r*-value for each chain, known as free ends, do not contribute to bulk stiffness, they are discarded. A large number of *r*-values, on the order of 10,000, are generated in order to ensure statistical validity. From these values, a probability density function (PDF) may be estimated using various statistical methods.

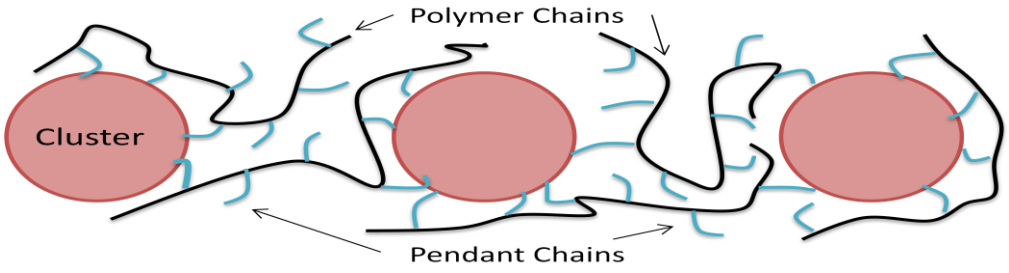

Figure 6.4: Visual approximation of model output

Of central importance to this thesis is the relationship between cross link density and material stiffness. In order to capture this, the current model is adapted in the following manner: baseline stiffness is calculated by generating *r*-values via the method described above. In this case, not all cross links successfully communicate with clusters, corresponding to a state of lower cross link density. To simulate a scenario in which cross link density has been increased within the polymer, all pendant chains are assumed to communicate with the nearest cluster, resulting in 100% communication rate and a general decrease in the average calculated *r*-value. The rationale for this scenario begins with the recognition that state change (in this thesis, from counter ion valency change) will correspond with minor morphological shifts including cluster size. It is then postulated that this facilitation of chain mobility will enable previously free pendant chains to communicate with (respond to ionic attraction of) the increased valency counter ion. It is further assumed in this illustration case that stiffness variation due to the morphological shift will be small compared to that of the increased cross link density.

6.2.2 Statistical analysis

In order to estimate a PDF, *P(r),* from a distribution of computationally generated r-values based on a polymer chain conformation, a variety of statistical techniques may be employed. In previous studies, a traditional cubic spline approach has been implemented as well as the Johnson family of distributions [26, 29, 30]. The Johnson family has been shown to yield stable predictions and in addition, is well defined. Thus, it is the preferred method for estimating *P(r).* Furthermore, an advantageous feature of the Johnson family of distributions is that the four parameters all have specific statistical meaning and estimation of these four parameters allows for easy application of *P(r).* There exist four Johnson family distributions including unbounded,

bounded, lognormal, and normal. Previous efforts utilize only the unbounded and bounded families as they are both sufficiently flexible for the generated data [26].

In general, the PDF *P(r)* based on the Johnson family of distributions has the following form

$$P(r) = \frac{\delta}{\lambda\sqrt{2\pi}} f'\left(\frac{r-\xi}{\lambda}\right) exp\left\{-\frac{1}{2}\left[\gamma + \delta * f\left(\frac{r-\xi}{\lambda}\right)\right]\right\} \tag{6.4}$$

where δ and γ are shape parameters, λ is a scale parameter, and ξ is a location parameter. The function *f* is defined according to the applied distribution family for all r ∈ H with *f'* being the first derivative of *f* with respect to r.

$$f(y) = \begin{cases} \ln\left(y + \sqrt{y^2 + 1}\right), & \text{for the Su (unbounded) family} \\ \ln\dfrac{y}{1-y}, & \text{for the SB (bounded) family} \end{cases}$$

$$H = \begin{cases} (-\infty, +\infty), & \text{for the Su (unbounded) family} \\ [\xi, \xi + \lambda], & \text{for the SB (bounded) family} \end{cases}$$

6.2.3 Model for estimation of material stiffness

Utilizing Boltzman's approach to statistical thermodynamics, the estimated probability density function *P(r)* for the simulated distribution of end-to-end chain lengths, or *r*-values, may be used to compute Young's modulus. The entropy of the chain is related to *P(r)* by the expression

$$S(r) = c + k \ln P(r) \tag{6.5}$$

where *k* is Boltzmann's constant and *c* is a constant of integration which drops out when the difference in entropy for the unperturbed configuration is taken with respect to the distorted

configuration. Utilizing the "three chain" model under the assumptions of rubberlike elasticity described by Treloar [53], the change in entropy upon distortion is given by

$$\Delta S = \frac{\nu}{3}\left[S(r_0\alpha) + 2S\left(r_0\alpha^{-1/2}\right) - 3S(r_0)\right] \tag{6.6}$$

where ν is the number density of network chains, r_0 is the root mean square of the generated *r*-values, and $\alpha = L/L_i$ is the relative length of the sample. Assuming that under load, the rotation about the individual bonds is unrestricted, it can also be assumed that Helmholtz free energy is strictly a function of entropy, which allows the nominal stress to be calculated using the expression

$$f^* = -T\left(\frac{\partial \Delta S}{\partial \alpha}\right)_T = -\frac{\nu kTr_0}{3}\left[G'(r_0\alpha) - \alpha^{-3/2}G'\left(r_0\alpha^{-1/2}\right)\right] \tag{6.7}$$

where

$$G(r) = \ln P(r)$$
$$G'(r) = \frac{dG(r)}{dr}.$$

The corresponding modulus $[f^*]$ is then given as

$$[f^*] = \frac{f^*}{\alpha - \alpha^{-2}} \tag{6.8}$$

and approaches Young's modulus for small strains ($\alpha \rightarrow 1$). Substituting equation (6.7) into equation (6.8) and applying L'Hôpital's rule yields the following expression for material stiffness

$$E = -\frac{\nu kTr_0}{6}\left\{\frac{r_0P(r_0)P''(r_0) - r_0\left[P'(r_0)\right]^2 + P(r_0)P'(r_0)}{[P(r_0)]^2}\right\}. \tag{6.9}$$

The number density of network chains, ν, is estimated per the methods of Weiland et al.

6.3 RESULTS

The current RIS-MC simulation generates backbone chains between 50 and 80 repeating units *m*. It has been proposed that physically realistic chain lengths consist of between 135 and 225 repeat units [29]. However, more recent models have shown that between 50 and 80 units are sufficient to obtain repeatable, stable predictions [26]. Between 9950 and 10,000 *r*-values are generated per simulation as previous studies have also concluded that this is a sufficient number to achieve repeatable results as well as to ensure statistical validity. Ten simulations are run for both the baseline and increased cross linking cases, producing ten material stiffness predictions for each.

Estimates of a probability density function *P(r)* are generated using the Johnson family of distributions. More specifically, the bounded family of distributions, as shown in Figure 6.4, is used as they have been found to provide the most stable, reliable predictions [30].

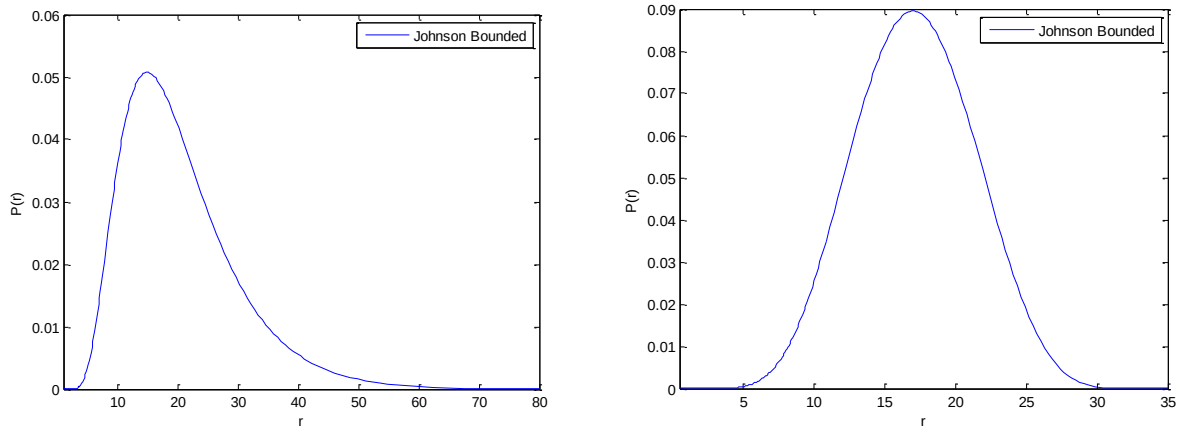

Figure 6.5: Typical Johnson bounded estimated PDFs [baseline (left) and increased cross linking cases (right).]

The software package FITTR1 allows each of the four Johnson families to be fitted using a variety of methods including moment and percentile matching, ordinary least squares, diagonally

weighted least squares, L_1-norm and L_∞-norm. General descriptive statistics such as mean, standard deviation, and range as well as goodness-of-fit information and the Kolmogorov-Smirnov (K-S) statistic are also produced for sets of data. Based on the results of previous studies as well as the low K-S statistic produced in this study, the diagonally weighted least squares method is chosen as the fitting method best suited for the current modeling effort.

For the baseline cross linking case of the sodium exchanged ionomer Nafion, approximately 73% of pendant chains are predicted to successfully communicate with a hydrophilic cluster; this corresponds to a predicted mean stiffness of 4.14 MPa with a standard deviation of 0.1 MPa. An increase in cross link density is simulated by allowing a 100% communication rate between the hydrophilic clusters and the ionic pendant chains of the polymer backbone chain. The mean stiffness of the increased cross linking case is calculated to be 15.9 MPa with a standard deviation of 1.3 MPa. This corresponds to an approximate 4-fold increase in bulk stiffness. Tables 6.2 and 6.3 provide the full details of all simulations for each case.

Table 6.2: Stiffness predictions; sodium exchanged Nafion 1200 EW (baseline)

Simulation	Com. %	Mean r value (Å)	S.D	γ	δ	λ	ξ	K-S	r_o (Å)	Stiffness (MPa)
1	72.89	20.86	11.64	4.334	1.885	194.2	0.745	0.065	22.39	4.178
2	72.45	21.00	11.94	4.070	1.826	181.3	0.918	0.066	22.60	4.020
3	72.88	21.05	11.69	5.769	2.014	344.2	-0.004	0.066	22.79	4.107
4	73.20	21.03	11.51	6.793	2.012	533.8	0.916	0.065	22.82	4.275
5	72.92	20.85	11.54	5.793	2.050	329.6	-0.001	0.068	22.45	4.125
6	72.76	21.19	11.69	3.928	1.847	170.1	0.609	0.070	22.69	4.275
7	73.47	20.80	11.57	3.909	1.862	162.5	0.692	0.071	22.21	4.271
8	72.59	21.20	11.81	3.759	1.807	161.9	0.719	0.072	22.73	4.028
9	72.70	20.79	11.61	4.389	1.871	201	0.812	0.065	22.39	4.093
10	72.42	21.10	11.73	6.427	1.997	462.6	0.797	0.064	22.89	4.095

Table 6.3: Stiffness predictions; sodium exchanged Nafion 1200 EW (increased cross linking)

Simulation	Com. %	Mean r value (Å)	S.D	γ	δ	λ	ξ	K-S	r_o (Å)	Stiffness (MPa)
1	100	17.01	4.663	0.155	1.987	35.49	0.047	0.038	17.65	15.42
2	100	16.99	4.735	-0.103	1.816	33.27	0.031	0.038	17.63	14.62
3	100	17.00	4.703	-0.042	1.869	33.78	0.051	0.038	17.64	15.17
4	100	17.06	4.687	0.071	1.917	34.67	0.144	0.037	18.28	17.09
5	100	17.00	4.691	-6.447	7.890	163.8	-96.45	0.024	17.62	18.28
6	100	17.02	4.700	0.353	2.107	37.57	-0.114	0.040	17.69	16.44
7	100	17.03	4.692	0.042	1.912	34.35	0.158	0.038	17.67	15.53
8	100	17.03	4.675	0.221	2.066	36.40	-0.108	0.042	17.67	16.59
9	100	16.97	4.709	0.046	1.937	34.84	-0.137	0.038	17.99	16.08
10	100	16.86	4.711	-0.358	1.672	31.15	-0.190	0.031	17.45	13.36

6.4 MODELING DISCUSSION AND SUMMARY

The current modeling effort generalizes the phenomenon of increased pendant chain communication with hydrophilic clusters in ionomeric materials and the subsequent relationship to mechanical properties by studying the well defined case of Nafion. One of the goals of this effort is to establish the foundations of a multi-scale modeling method for stiffness prediction that is able to account for increases in cross link density akin to that expected in electroplastic elastomers. One of the first observations is the seemingly large distribution range of stiffness predictions for the increased cross linking case (standard deviation of 1.3 MPa) compared to the baseline case (0.1 MPa). This result is intriguing in that the respective standard deviations for the calculation of r_o are roughly the same (.225 Å versus .235 Å) and the distributions of *r*-values for the increased cross linking case consistently display much lower standard deviations as shown in Tables 6.2 and 6.3. When viewed through the lens of percent accuracy, while the disparity remains, it does decrease; the standard deviation of the baseline case remains at 2% of the median while the standard deviation of the increased cross linking case is 8% of the median

value. Consider that upon careful inspection of Equation 6.6, it is noted that predicted stiffness is a function of the probability of a chain having length r_o as well as the slope and variation in slope at that point. Subsequent inspection of Figure 6.4 draws attention to the fact that in the baseline case, this point occurs on a well behaved region of the PDF while for the increased cross linking case, it occurs near the peak. In previous Nafion studies, the bounded family was selected precisely because this point tended to align with a well behaved portion of the PDF. Thus, one possible conclusion is that the Johnson Bounded approach may need reconsideration in the case of electroplastic elastomers.

Table 6.4: Stiffness prediction results

Modeling Conditions	Mean Calculated Stiffness	Standard Deviation
Current Baseline Case	4.1 MPa	0.1 MPa
Current Increase X-Link Case	15.9 MPa	1.3 MPa

Overall, simulations project an approximate 4-fold increase in stiffness as cross link density is increased. Although the model is not specific to electroplastic elastomers at this time, this prediction trend is consistent with the material development hypothesis. In addition, this prediction displays a trend similar to the observed order of magnitude increase in stiffness when a single sample is chemically transitioned from the iron (II) to iron (III) counter ion considered in the previous chapter.

Sources of error contributing to the variation between this prediction (4-fold increase with increased valency) as compared to the experimental case (10-fold increase) include: (1) most significantly that Nafion is a fundamentally different ionomer case, and (2) even for the Nafion case, the baseline prediction is low compared to previous studies (~4 MPa as compared to ~10 MPa predicted previously). However, these sources of error do not diminish the significance

of the projected increase nor the potential for developing this modeling approach in optimization of electroplastic elastomers.

Consider for instance, the issue of formulation optimization. If provided reasonable estimates for cross link length and bond angles for alternate formulations (for instance, from the software package HyperChem), this modeling tool may be employed to expedite selection of formulation targets (as compared to purely experimental timelines). Similarly, consider that the demonstration case assumes a pendant chain placement at approximately every eighth interval. This rate of incidence has not been optimized for electroplastic elastomers (and further, may have contributed to the prediction of the ~4-fold increase as opposed to the experimentally measured ~10-fold increase for counter ion valency change). Thus, the approach could be employed to explore the trade-offs associated with varying this interval.

In summary, this chapter illustrates a modeling methodology that (1) even in rudimentary form is able to predict significant stiffness variation in the presence of increased communication of ionomeric pendant chains with adjacent clusters, and (2) has the potential to expedite formulation development.

APPENDIX A

COMPRESSION TESTING

The following appendix provides additional detail with regards to compression tests performed. Further results and details of compression tests conducted with the inclusion of electric current are provided, followed by individual stress-strain plots from each compression test reported in Section 5.1 of this thesis.

A.1 ELECTRIC CURRENT TESTS

Due to the fact that oxidation and reduction of counter ions, responsible for altering mechanical properties of electroplastic elastomers, is initiated by an electrochemical process, it is necessary to investigate any potential superfluous effects of electric current inclusion. To this end, compression tests are performed in which a current is run through the sample and compared with a baseline result. The testing procedure is as follows;

1. Establish a baseline modulus
2. Apply ~1mA for five minutes, conduct three compression tests with current still running
3. Switch off current and wait five minutes before performing three compression tests

4. Repeat step 2
5. Switch off current and wait ten minutes before performing three compression test
6. Apply ~1mA for ten minutes, conduct three compression tests with current still running

The above procedure is performed on a scaffold – iron (III) based hydrogel composite. Figure A.1 contains the subsequent results.

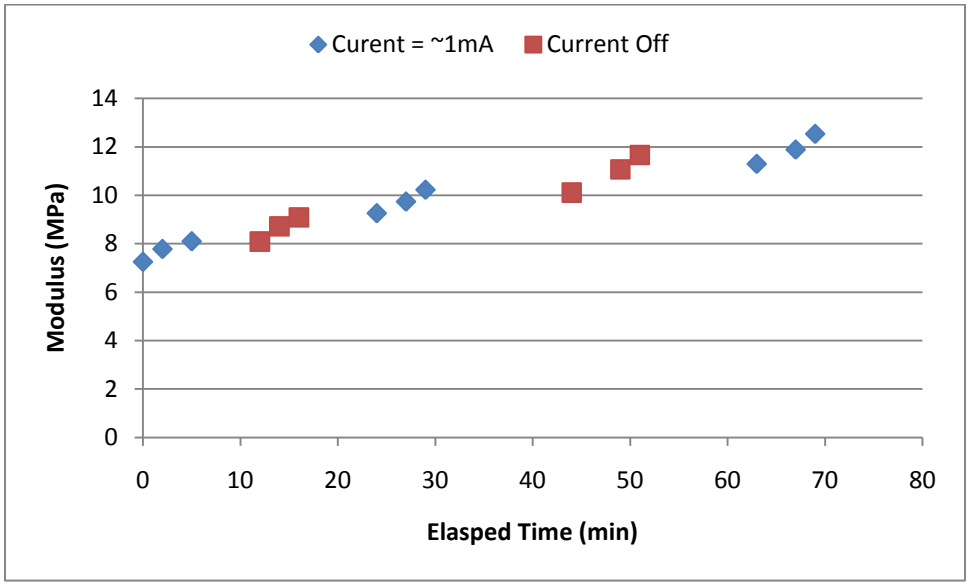

Figure A.1: Effects of electric current on compression modulus measurements of HD-2-Fe^{3+} (Baseline stiffness is 6.9 MPa)

Aside from the upward trending of modulus measurements, there are no visually discernable effects or irregularities resulting from running a current through the sample. This null result is encouraging as is suggests that no electrical coupling effects are displayed.

Initially, all compression tests include the application of a preload so as to ensure good contact between the compression piston and the sample. However, the crosshead is zeroed after the preload is applied, thus the preloading effect is amplified with each subsequent test, falsely indicating continual increases in stiffness. It is determined that such increases in compression

modulus between measurements are attributed to this error. Once the error is accounted for, this effect disappears from all subsequent tests.

Table A.1: Tabulated compression test results (HD-2-Fe^{3+}) with electric current. Shaded rows correspond to applied current of ~1mA and un-shaded rows correspond to no current applied.

Test	Compression Modulus	Time of Test
Baseline Test	6.9 MPa	10:07
1	7.3 MPa	10:27
2	7.8 MPa	10:29
3	8.1 MPa	10:33
1	8.1 MPa	10:40
2	8.7 MPa	10:42
3	9.1 MPa	10:44
1	9.3 MPa	10:52
2	9.7 MPa	10:55
3	10.2 MPa	10:57
1	10.1 MPa	11:11
2	11.1 MPa	11:17
3	11.7 MPa	11:19
1	11.3 MPa	11:31
2	11.9 MPa	11:34
3	12.5 MPa	11:36

A.2 DRY COMPRESSION TEST RESULTS

A.2.1 High Density Polyurethane Foam

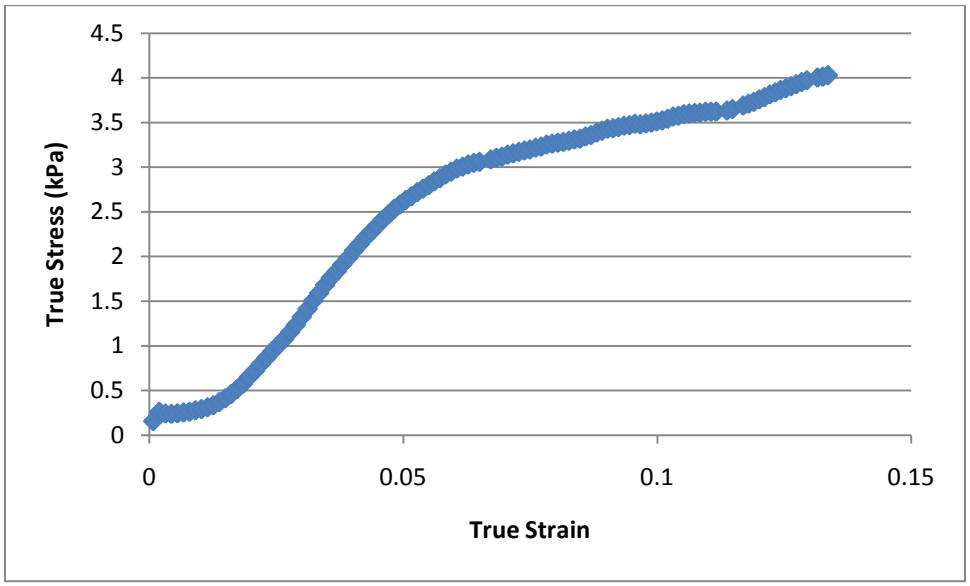

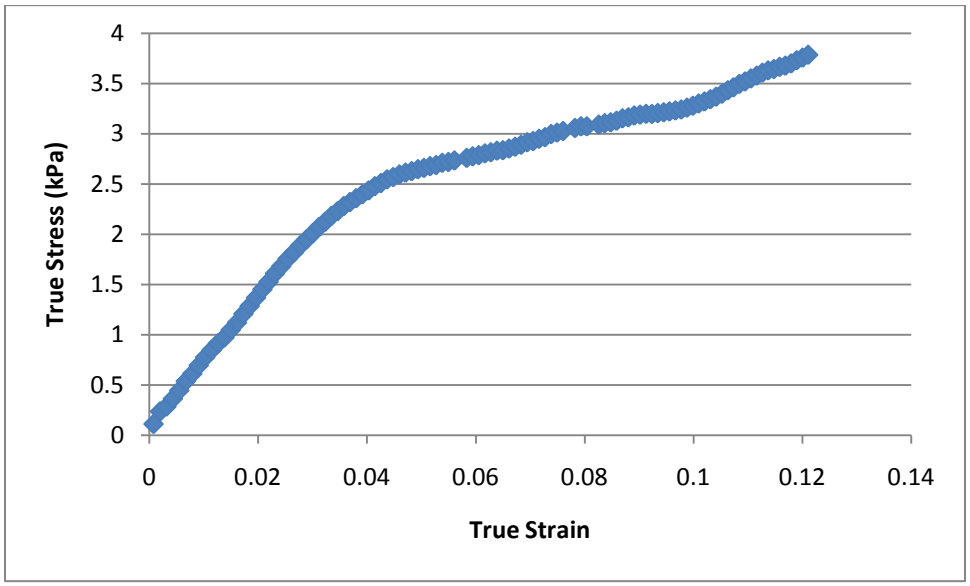

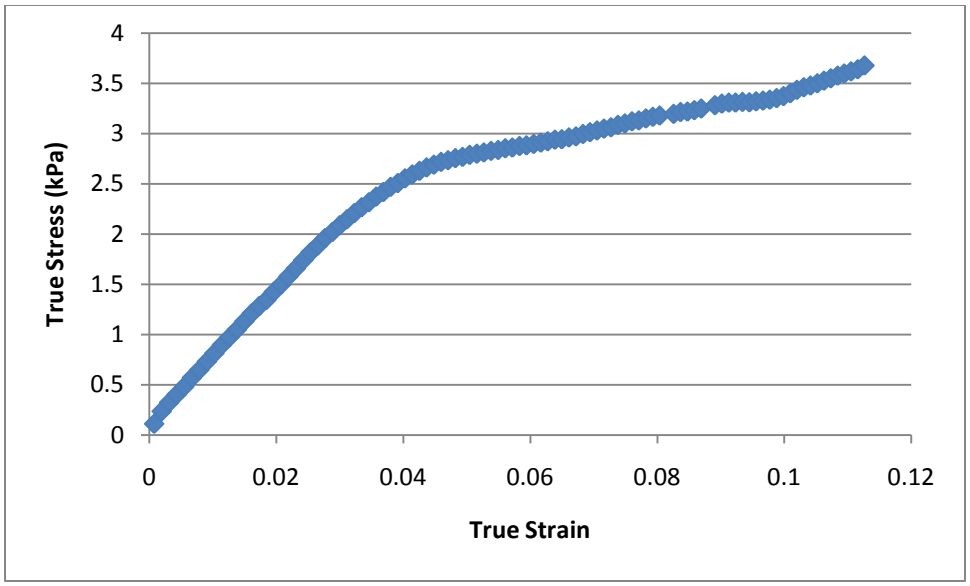
True Stress (kPa)
4
3.5
3
2.5
2
1.5
1
0.5
0
0
0.02
0.04
0.06
0.08
0.1
0.12
True Strain

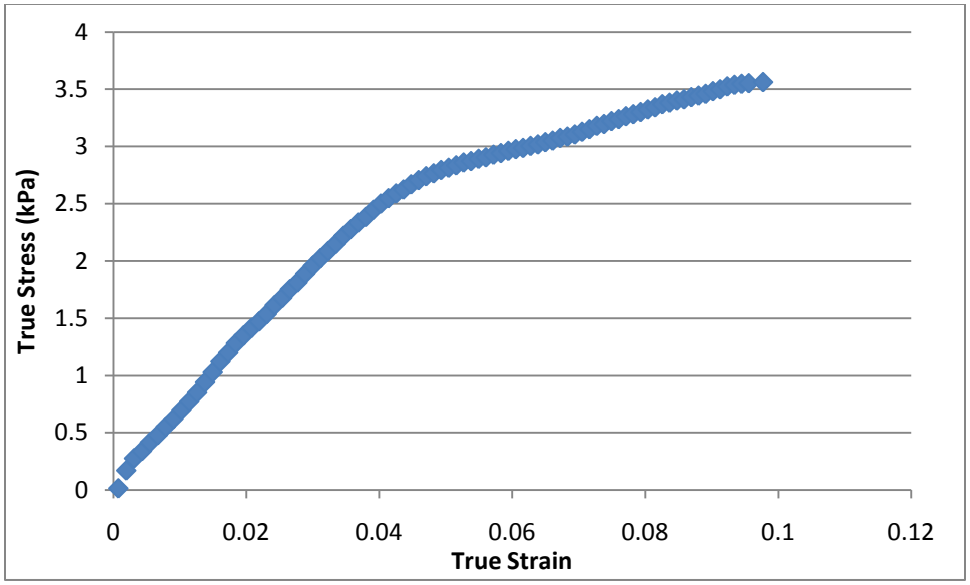
True Stress (kPa)
4
3.5
3
2.5
2
1.5
1
0.5
0
0
0.02
0.04
0.06
0.08
0.1
0.12
True Strain

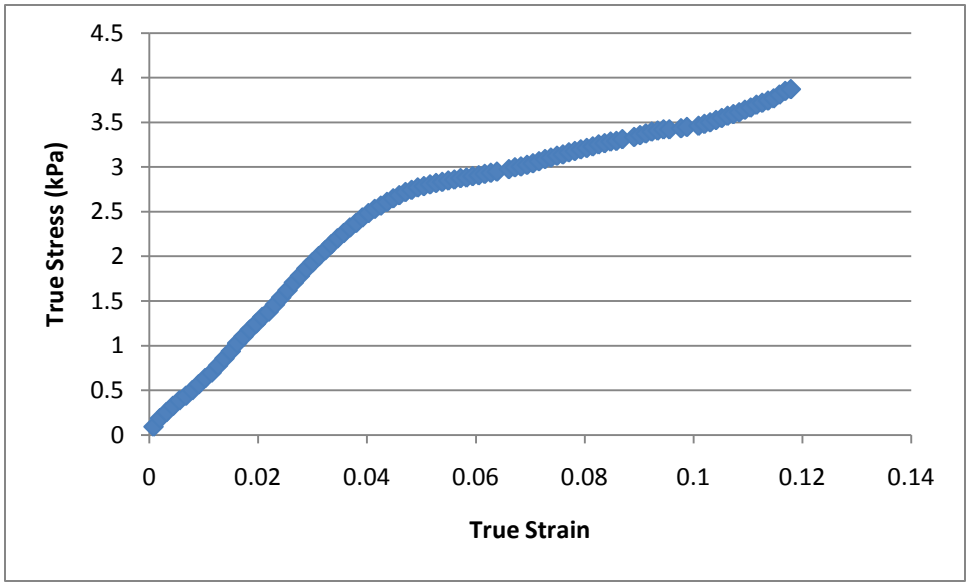

A.2.2 Low Density Polyurethane Foam

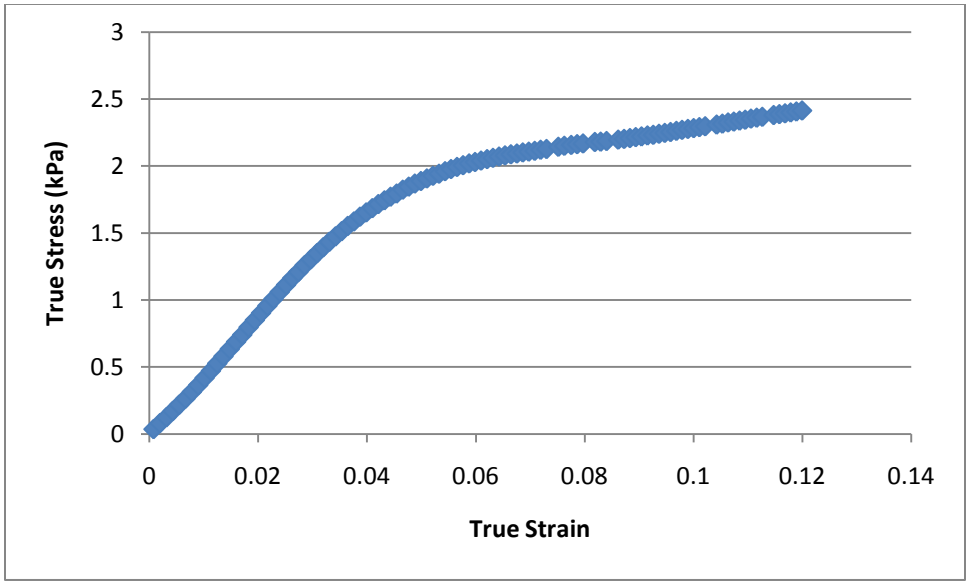

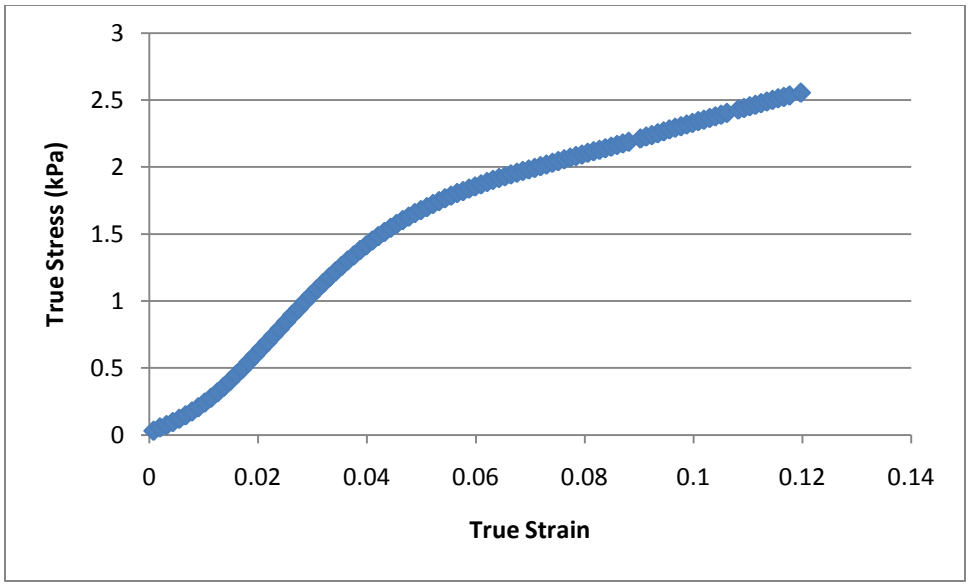
True Stress (kPa)
3
2.5
2
1.5
1
0.5
0
0
0.02
0.04
0.06
0.08
0.1
0.12
0.14
True Strain

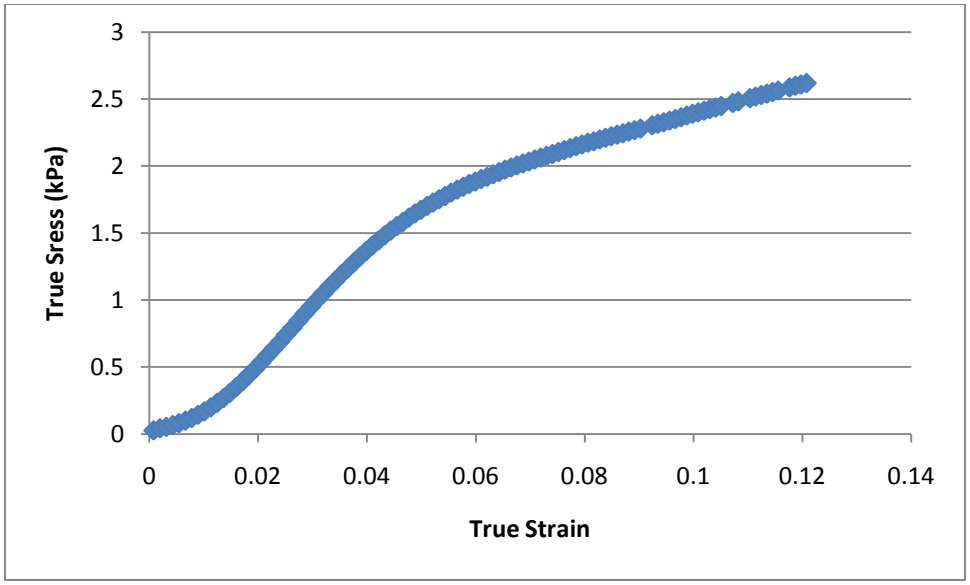
True Sress (kPa)
3
2.5
2
1.5
1
0.5
0
0
0.02
0.04
0.06
0.08
0.1
0.12
0.14
True Strain

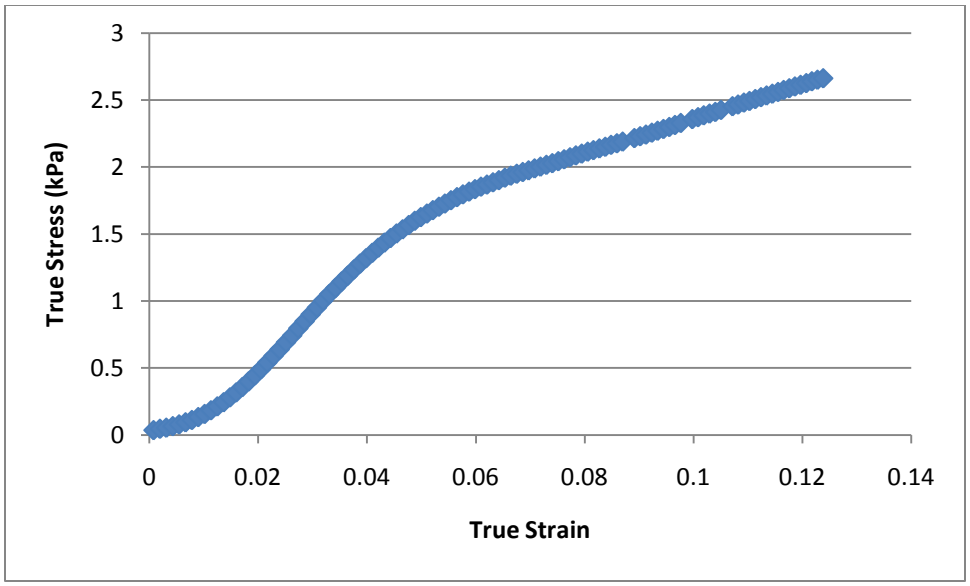
True Stress (kPa)
3
2.5
2
1.5
1
0.5
0
0
0.02
0.04
0.06
0.08
0.1
0.12
0.14
True Strain

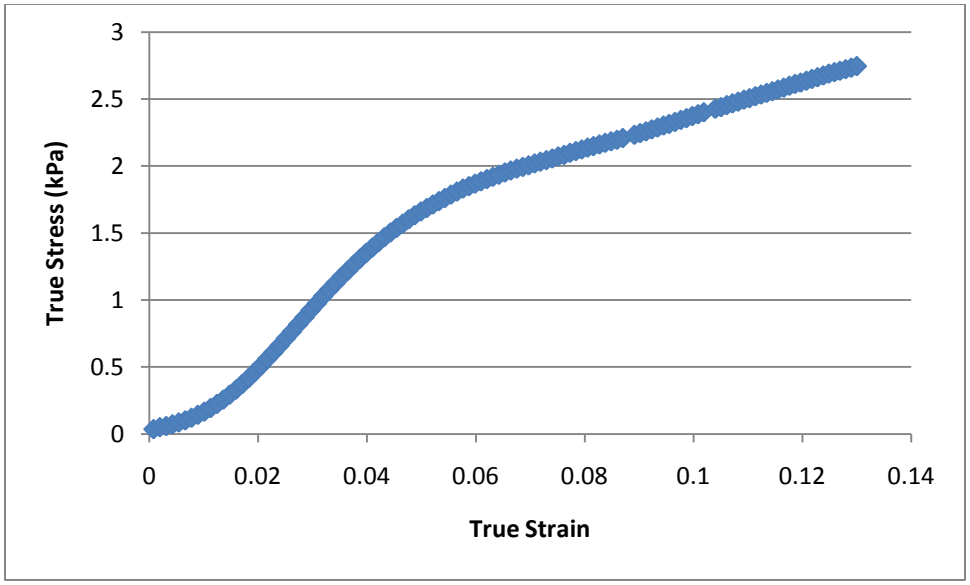
True Stress (kPa)
3
2.5
2
1.5
1
0.5
0
0
0.02
0.04
0.06
0.08
0.1
0.12
0.14
True Strain

A.2.3 Sodium Hydrogel

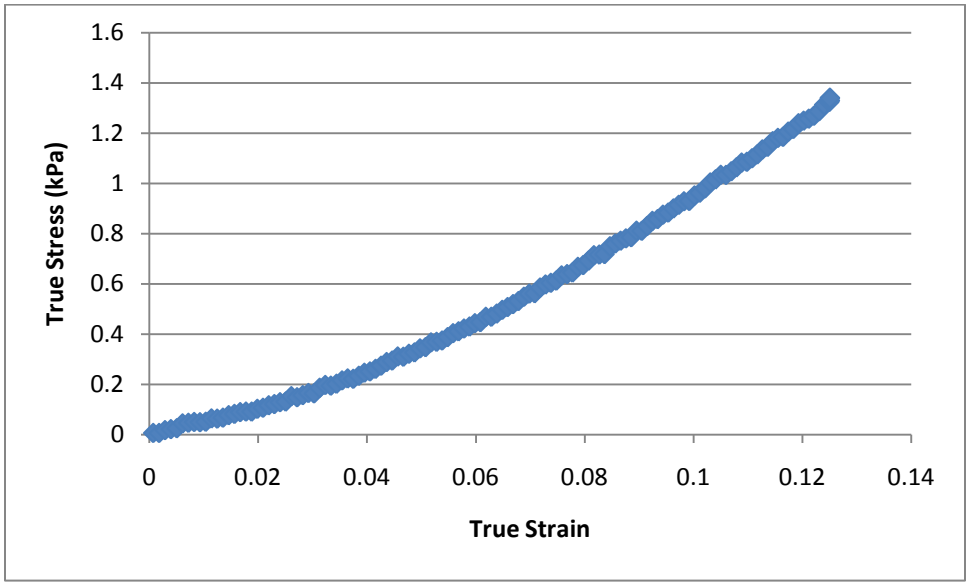

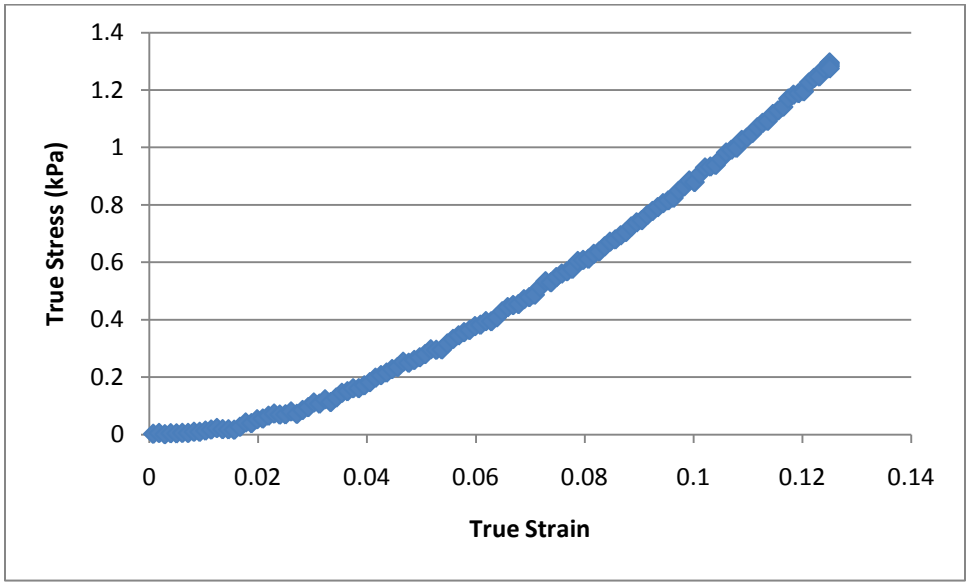

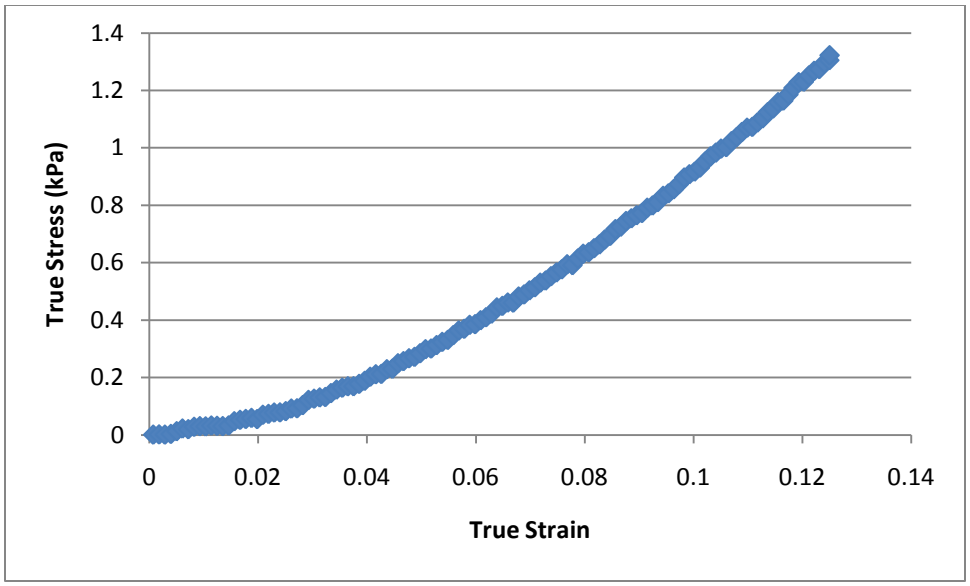
True Stress (kPa)
1.4
1.2
1
0.8
0.6
0.4
0.2
0
0
0.02
0.04
0.06
0.08
0.1
0.12
0.14
True Strain

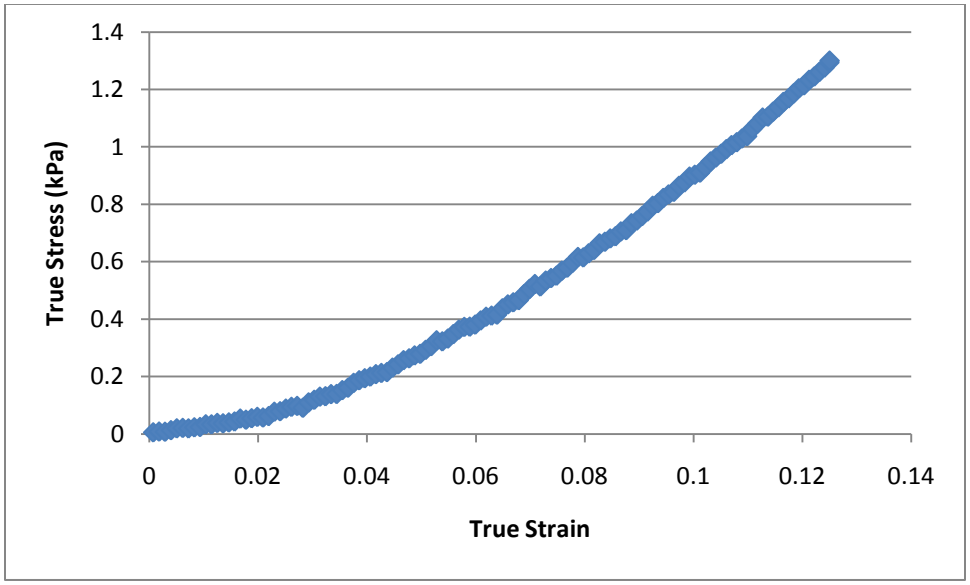
True Stress (kPa)
1.4
1.2
1
0.8
0.6
0.4
0.2
0
0
0.02
0.04
0.06
0.08
0.1
0.12
0.14
True Strain

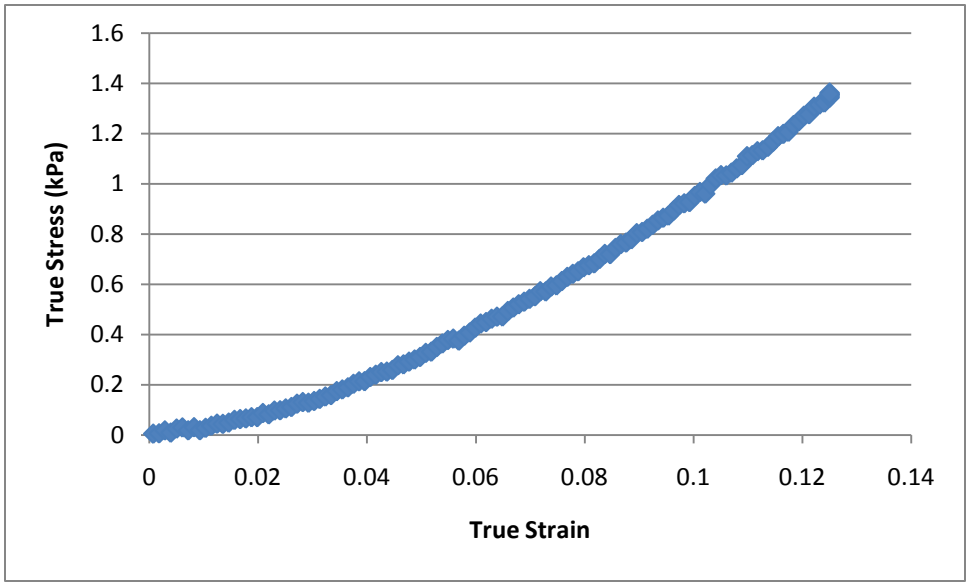
1.6
1.4
1.2
1
0.8
0.6
0.4
0.2
0
True Stress (kPa)
0
0.02
0.04
0.06
0.08
0.1
0.12
0.14
True Strain

A.2.4 HD-2-Na^+

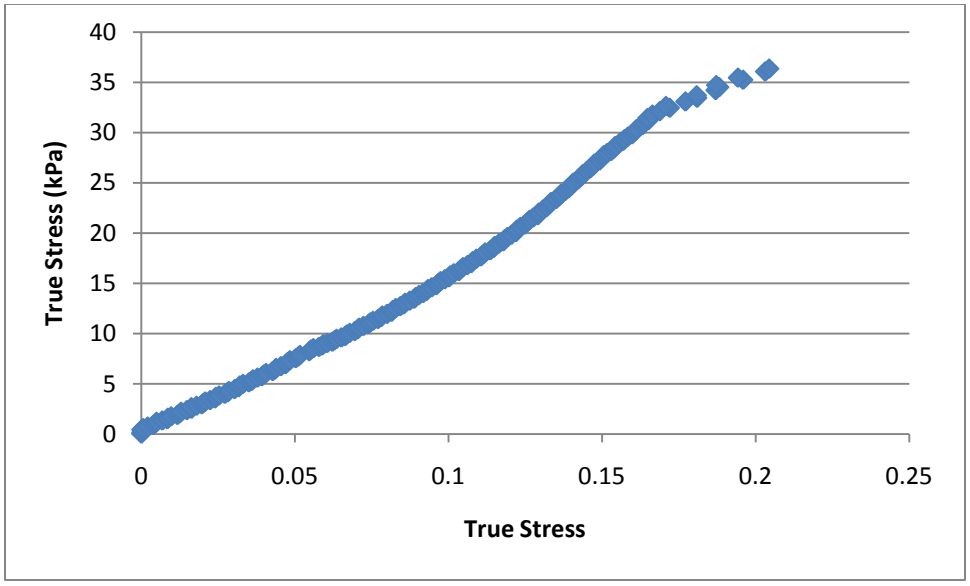
40
35
30
25
20
15
10
5
0
True Stress (kPa)
0
0.05
0.1
0.15
0.2
0.25
True Stress

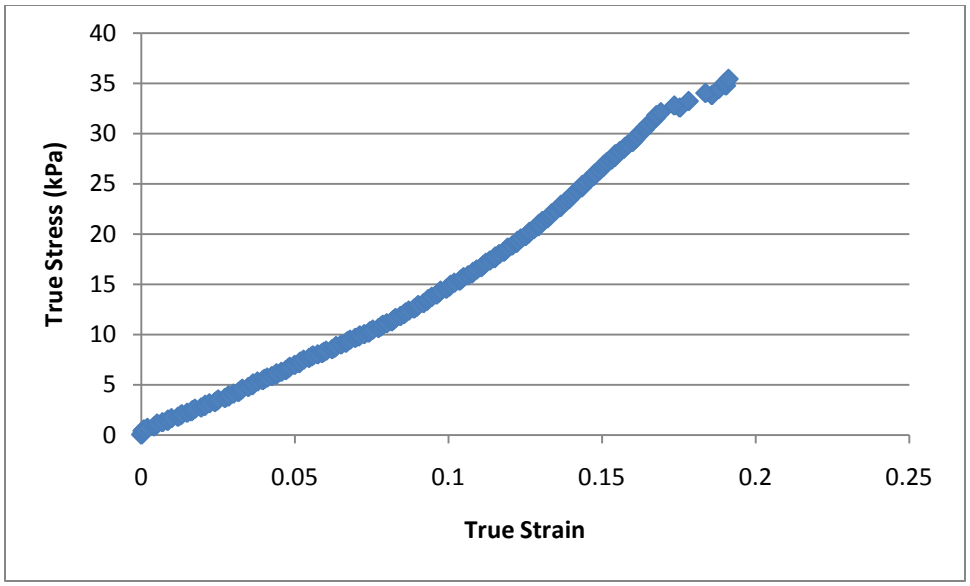
True Stress (kPa)
40
35
30
25
20
15
10
5
0
0
0.05
0.1
0.15
0.2
0.25
True Strain

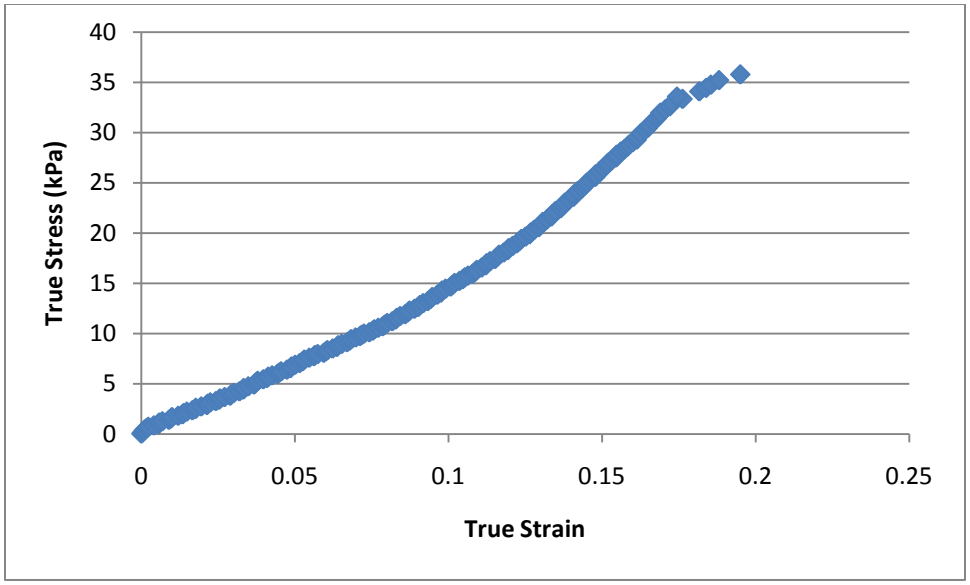
True Stress (kPa)
40
35
30
25
20
15
10
5
0
0
0.05
0.1
0.15
0.2
0.25
True Strain

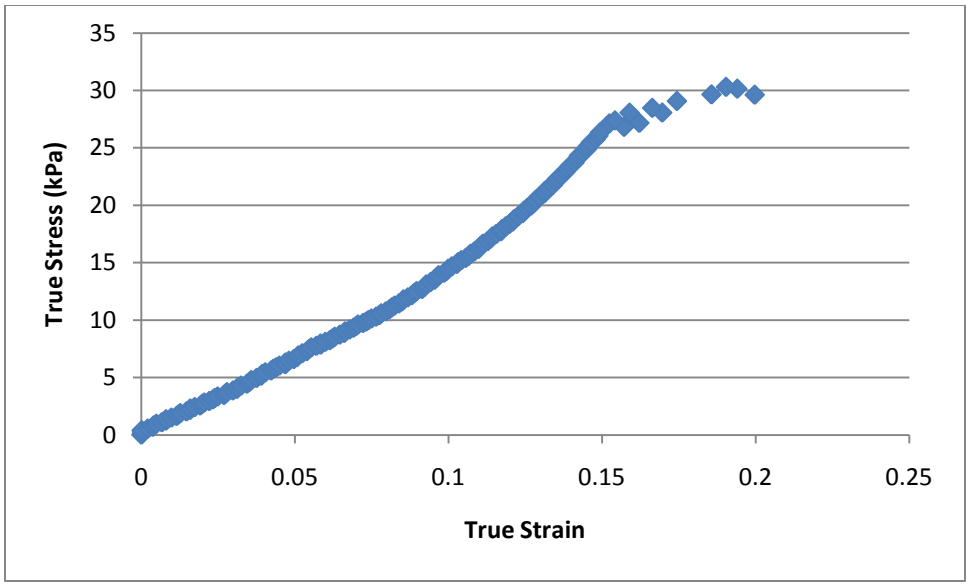
True Stress (kPa)
35
30
25
20
15
10
5
0
0
0.05
0.1
0.15
0.2
0.25
True Strain

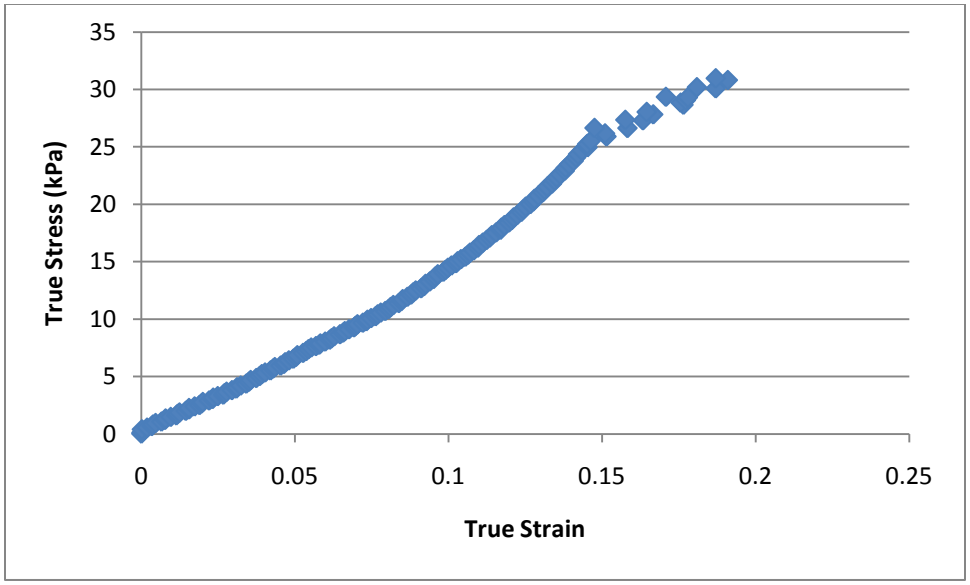
True Stress (kPa)
35
30
25
20
15
10
5
0
0
0.05
0.1
0.15
0.2
0.25
True Strain

A.2.5 HD-2-Fe^{2+}

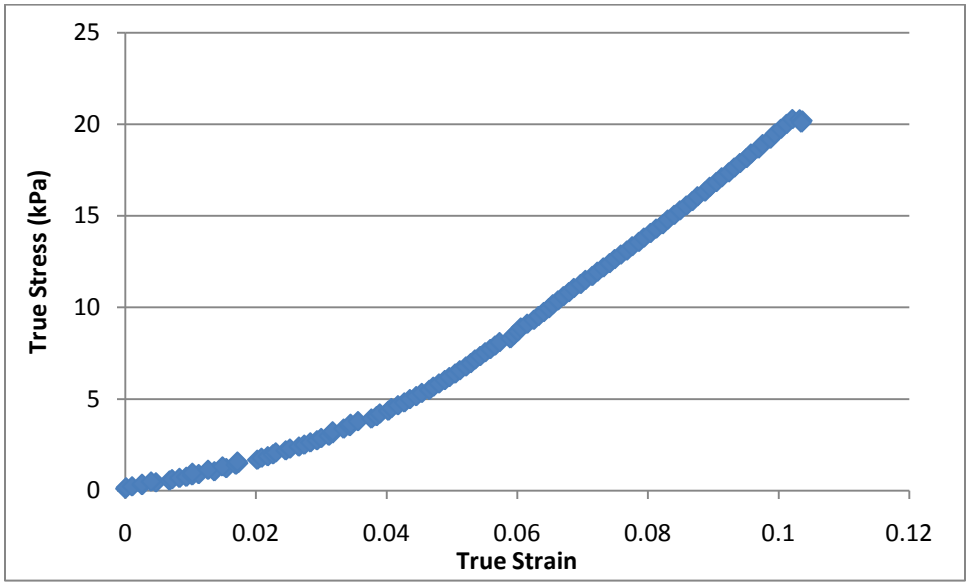
25
20
15
10
5
0
True Stress (kPa)
0
0.02
0.04
0.06
0.08
0.1
0.12
True Strain

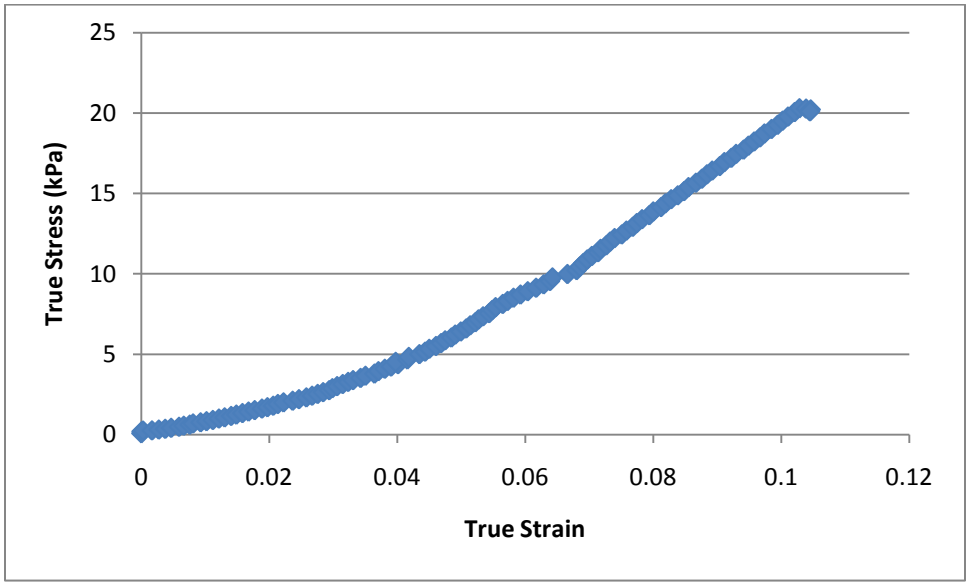
25
20
15
10
5
0
True Stress (kPa)
0
0.02
0.04
0.06
0.08
0.1
0.12
True Strain

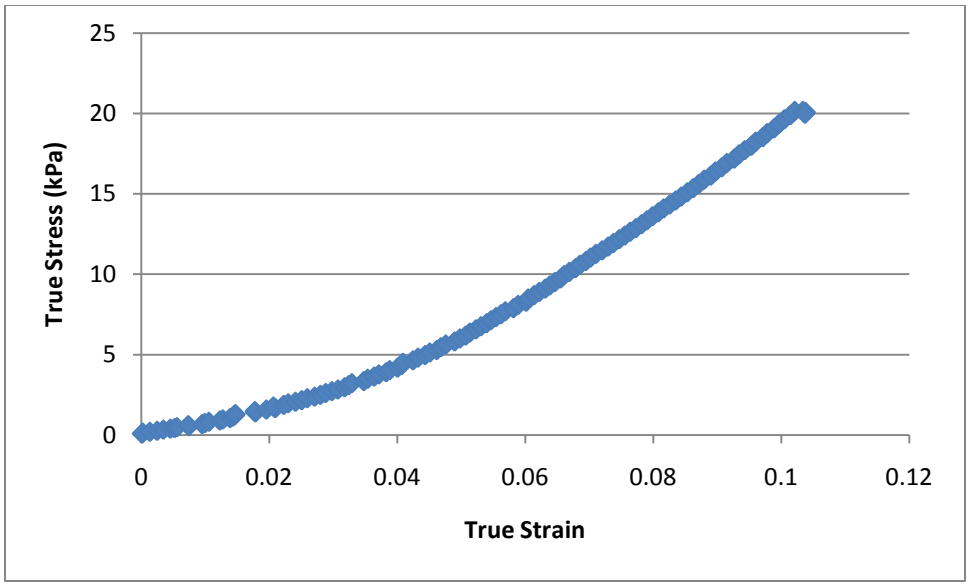
25
20
15
10
5
0
True Stress (kPa)
0
0.02
0.04
0.06
0.08
0.1
0.12
True Strain

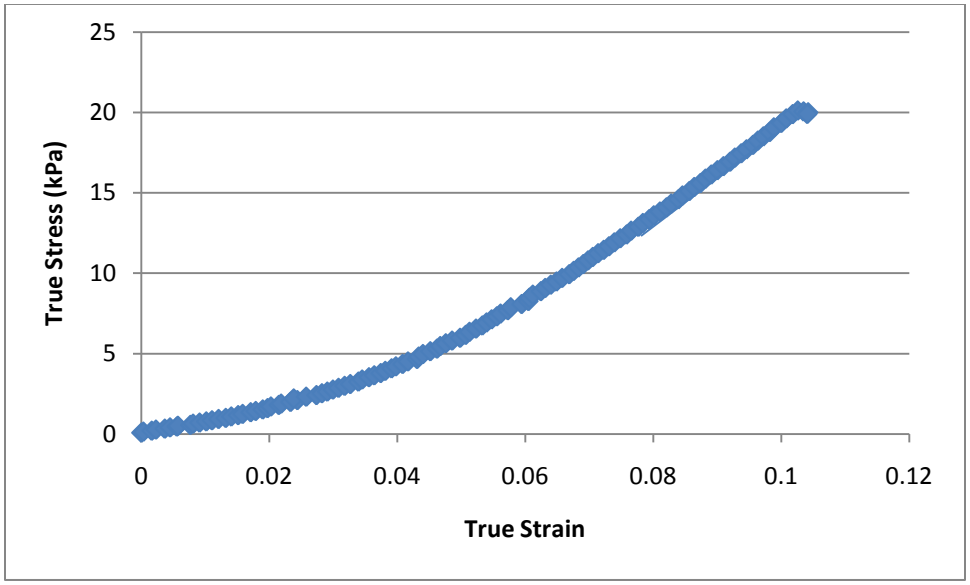
25
20
15
10
5
0
True Stress (kPa)
0
0.02
0.04
0.06
0.08
0.1
0.12
True Strain

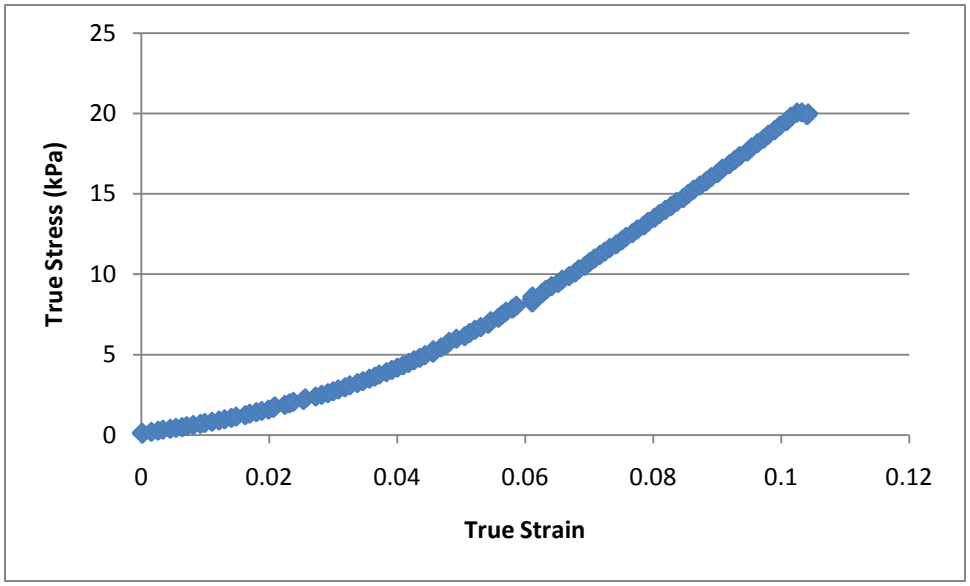
25
20
15
10
5
0
True Stress (kPa)
0
0.02
0.04
0.06
0.08
0.1
0.12
True Strain

A.2.6 HD-2-Fe^{3+}

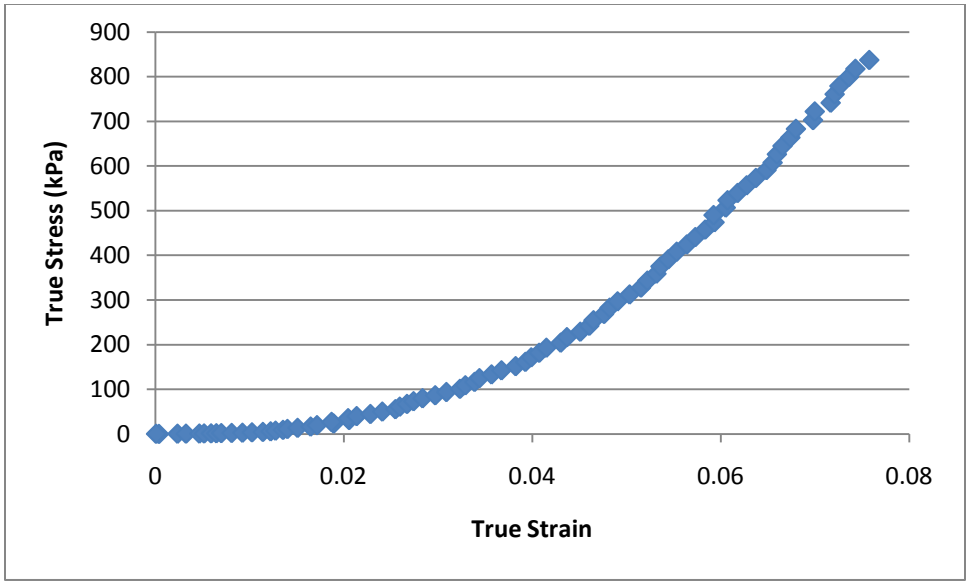
900
800
700
600
500
400
300
200
100
0
True Stress (kPa)
0
0.02
0.04
0.06
0.08
True Strain

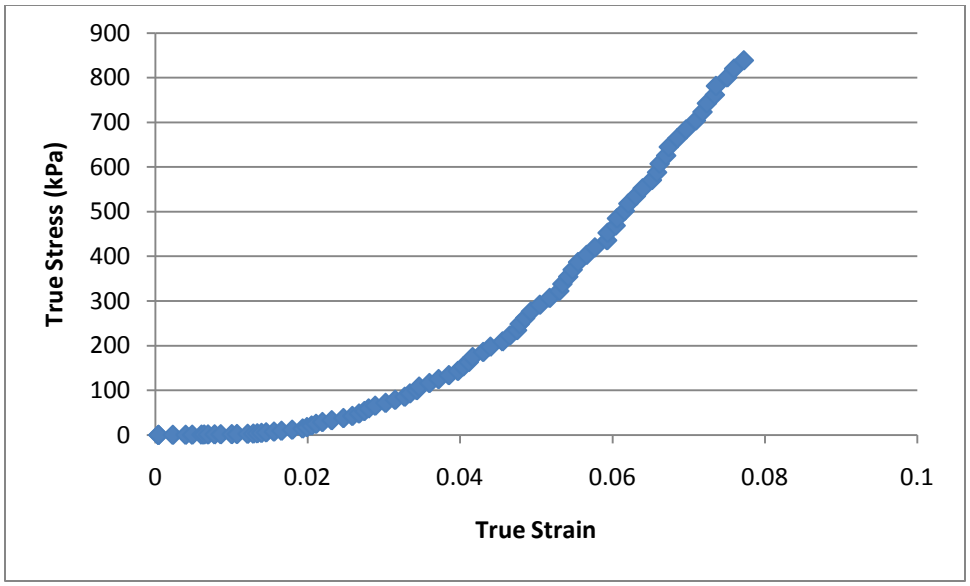
900
800
700
600
500
400
300
200
100
0
True Stress (kPa)
0
0.02
0.04
0.06
0.08
0.1
True Strain

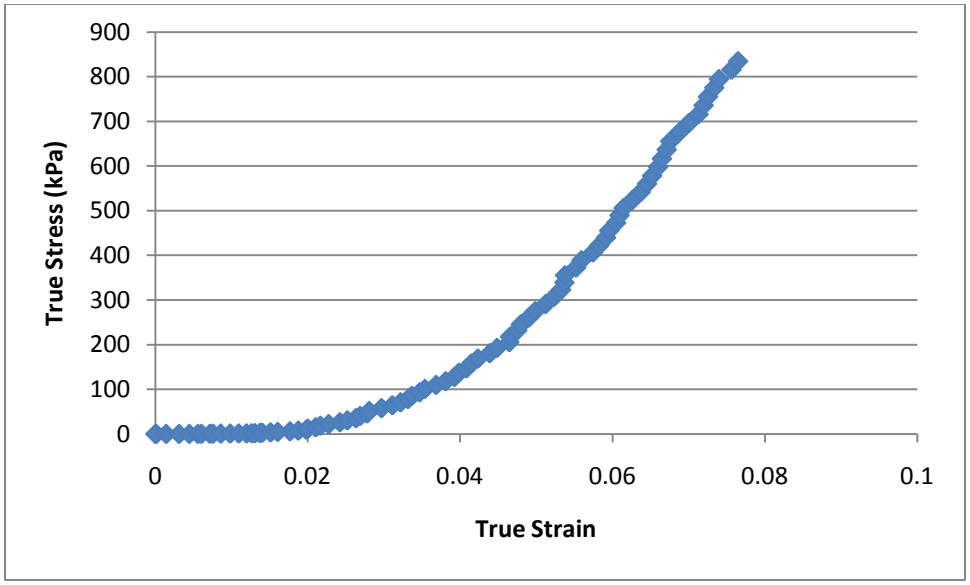
900
800
700
600
500
400
300
200
100
0
True Stress (kPa)
0
0.02
0.04
0.06
0.08
0.1
True Strain

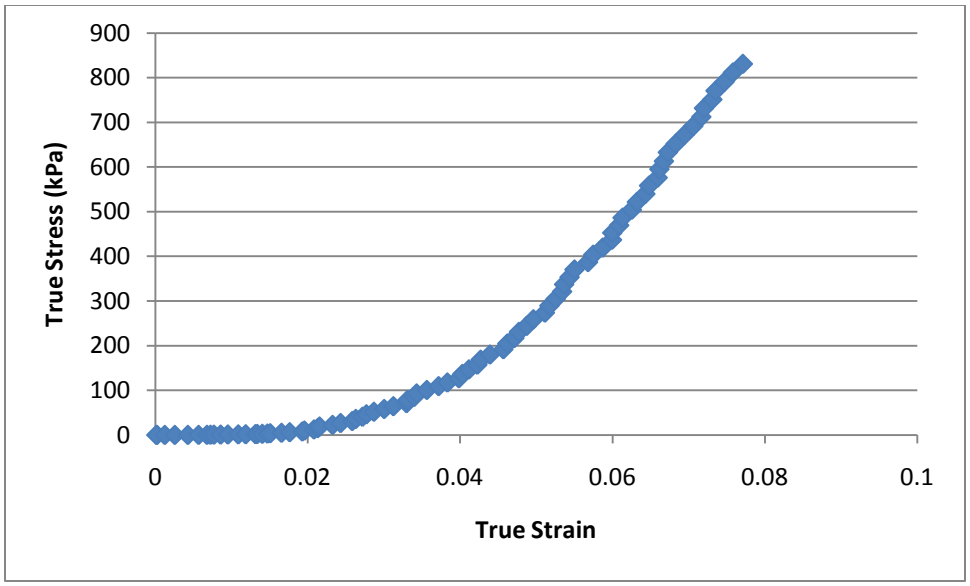
900
800
700
600
500
400
300
200
100
0
True Stress (kPa)
0
0.02
0.04
0.06
0.08
0.1
True Strain

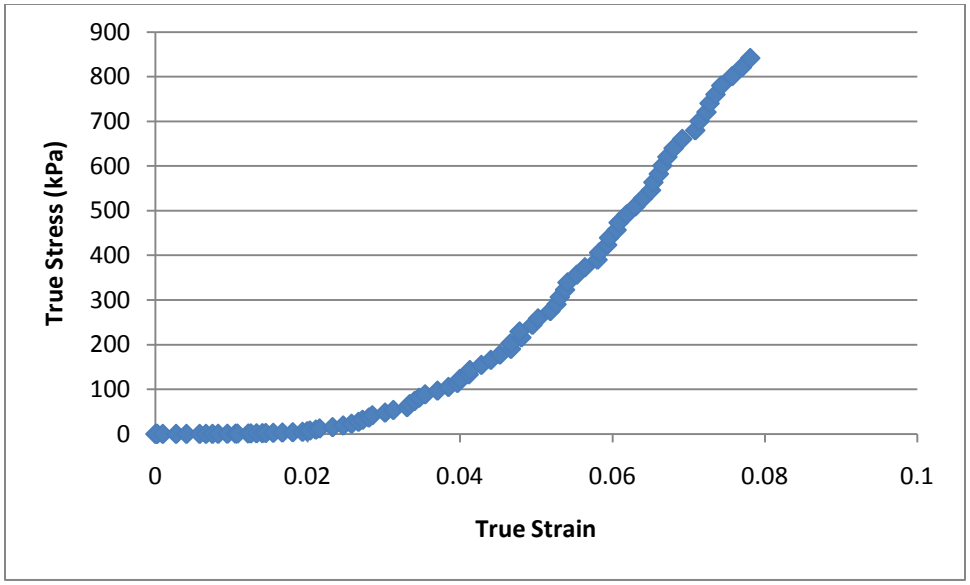
900
800
700
600
500
400
300
200
100
0
True Stress (kPa)
0
0.02
0.04
0.06
0.08
0.1
True Strain

A.3 WET COMPRESSION TEST RESULTS

A.3.1 High Density Polyurethane Foam

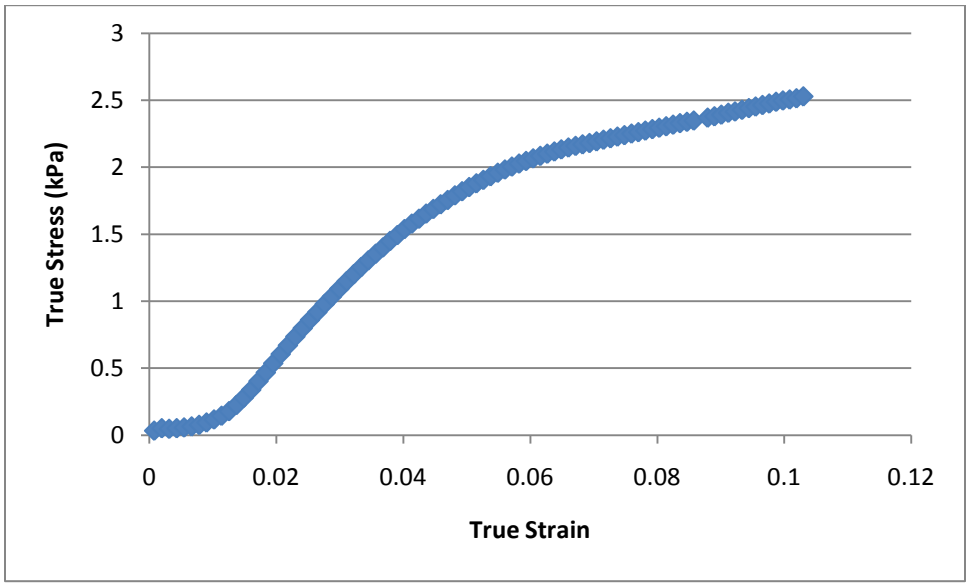

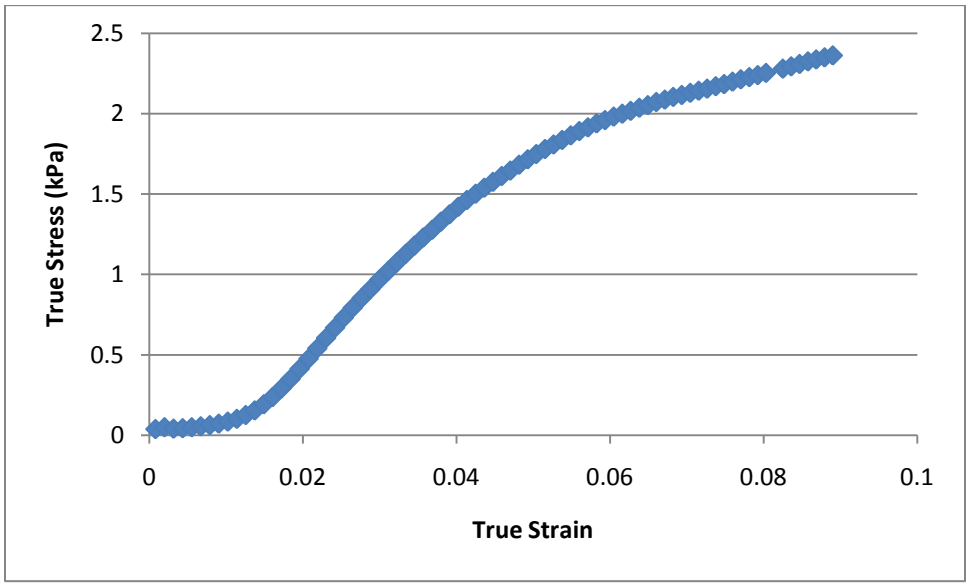

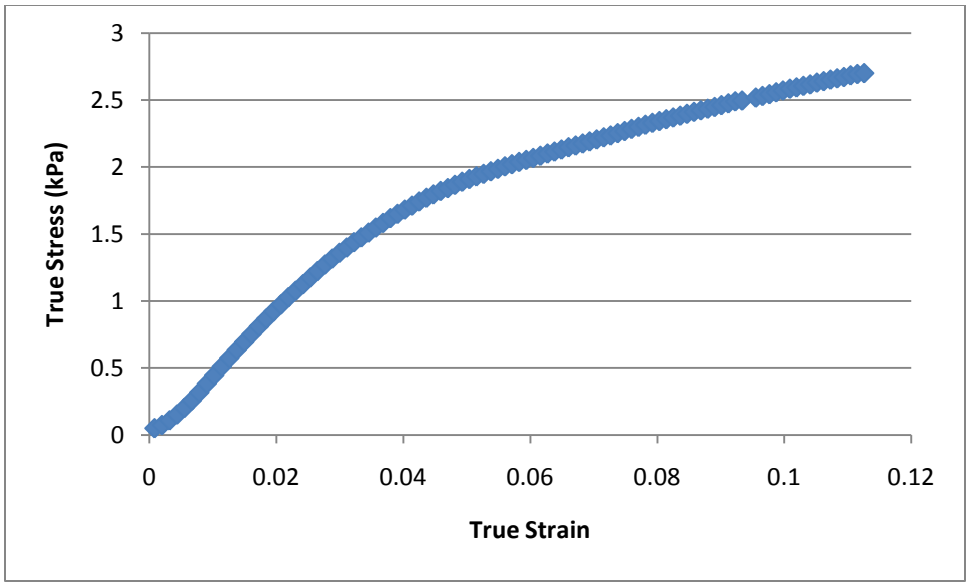
True Stress (kPa)
3
2.5
2
1.5
1
0.5
0
0
0.02
0.04
0.06
0.08
0.1
0.12
True Strain

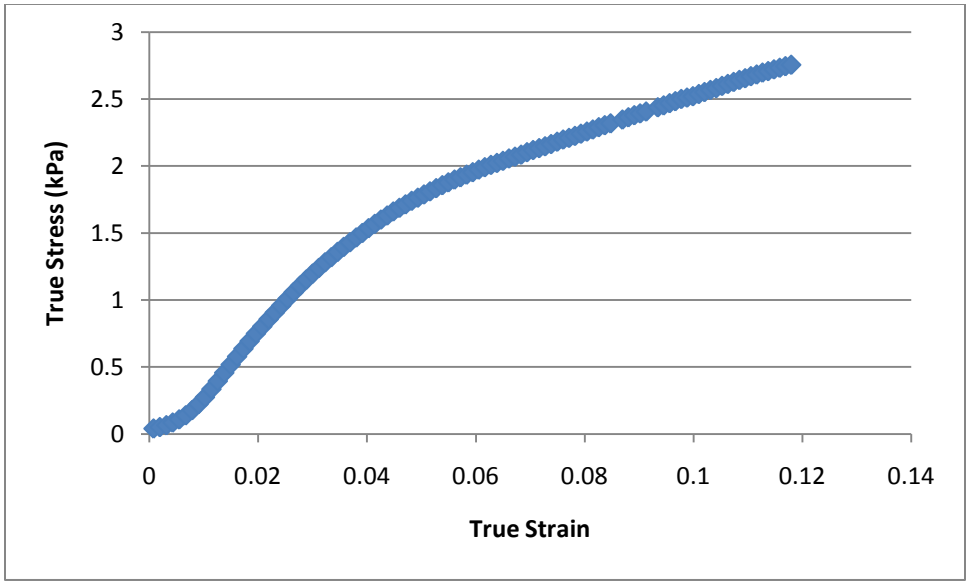
True Stress (kPa)
3
2.5
2
1.5
1
0.5
0
0
0.02
0.04
0.06
0.08
0.1
0.12
0.14
True Strain

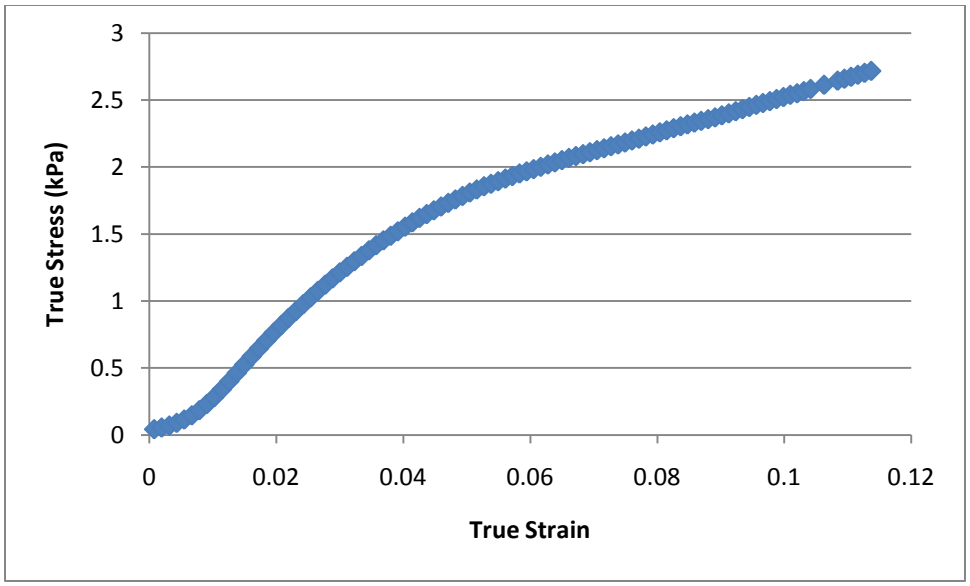

A.3.2 Low Density Polyurethane Foam

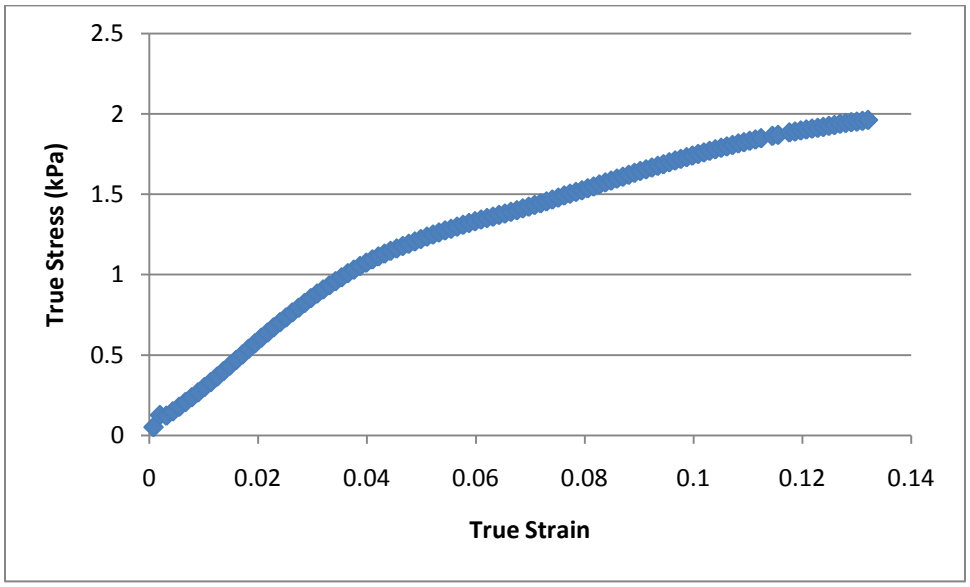

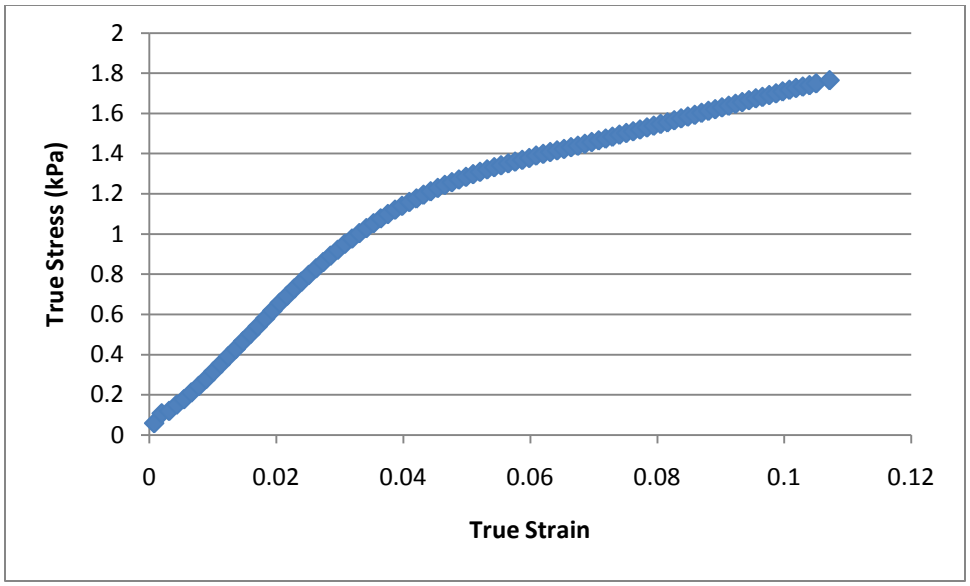
True Stress (kPa)
2
1.8
1.6
1.4
1.2
1
0.8
0.6
0.4
0.2
0
0
0.02
0.04
0.06
0.08
0.1
0.12
True Strain

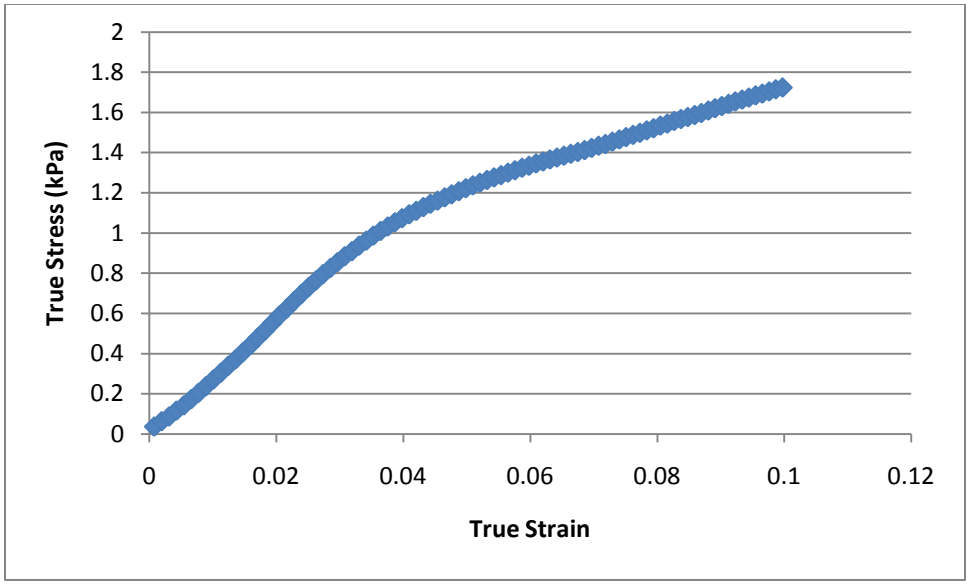
True Stress (kPa)
2
1.8
1.6
1.4
1.2
1
0.8
0.6
0.4
0.2
0
0
0.02
0.04
0.06
0.08
0.1
0.12
True Strain

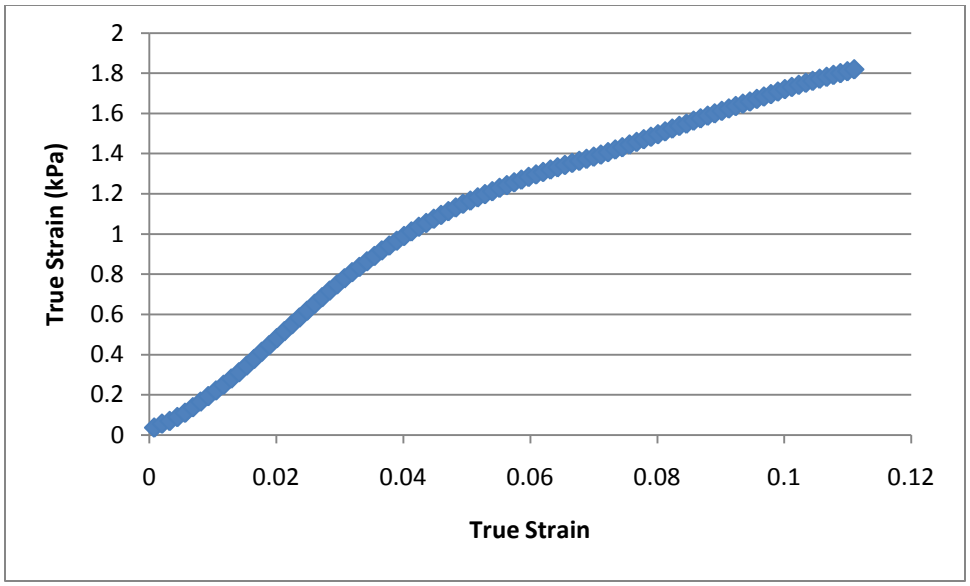
True Strain (kPa)
2
1.8
1.6
1.4
1.2
1
0.8
0.6
0.4
0.2
0
0
0.02
0.04
0.06
0.08
0.1
0.12
True Strain

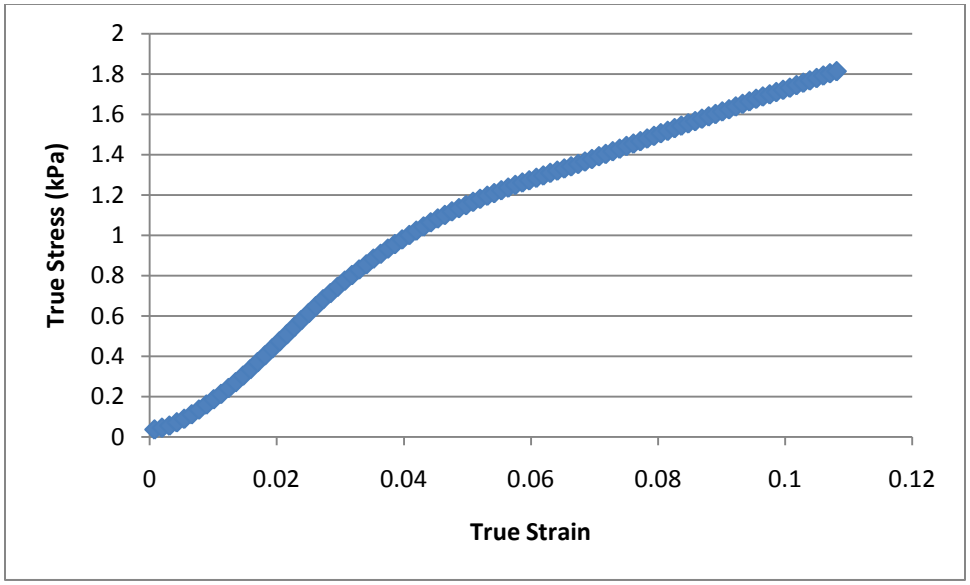
True Stress (kPa)
2
1.8
1.6
1.4
1.2
1
0.8
0.6
0.4
0.2
0
0
0.02
0.04
0.06
0.08
0.1
0.12
True Strain

A.3.3 HD-2-Na^+

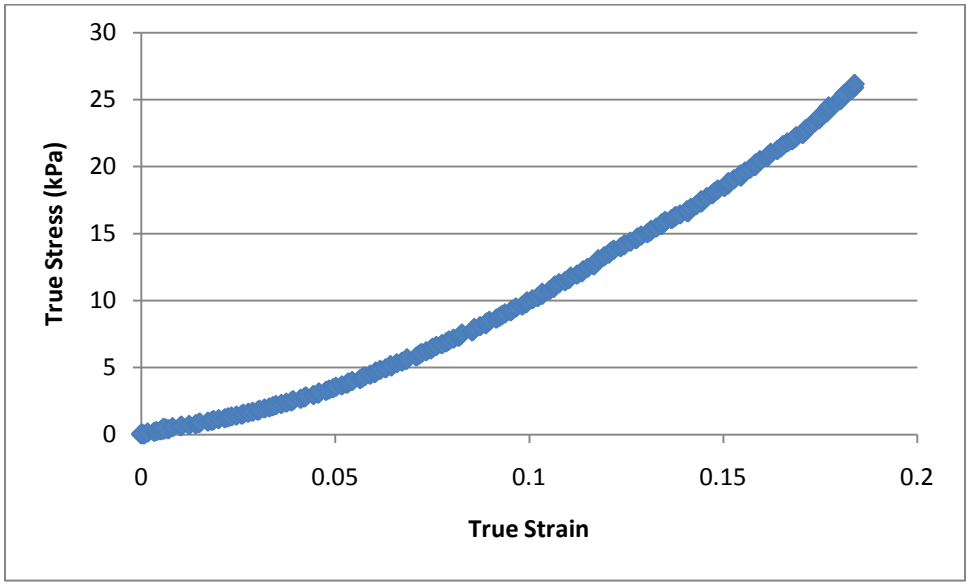
30
25
20
15
10
5
0
True Stress (kPa)
0
0.05
0.1
0.15
0.2
True Strain

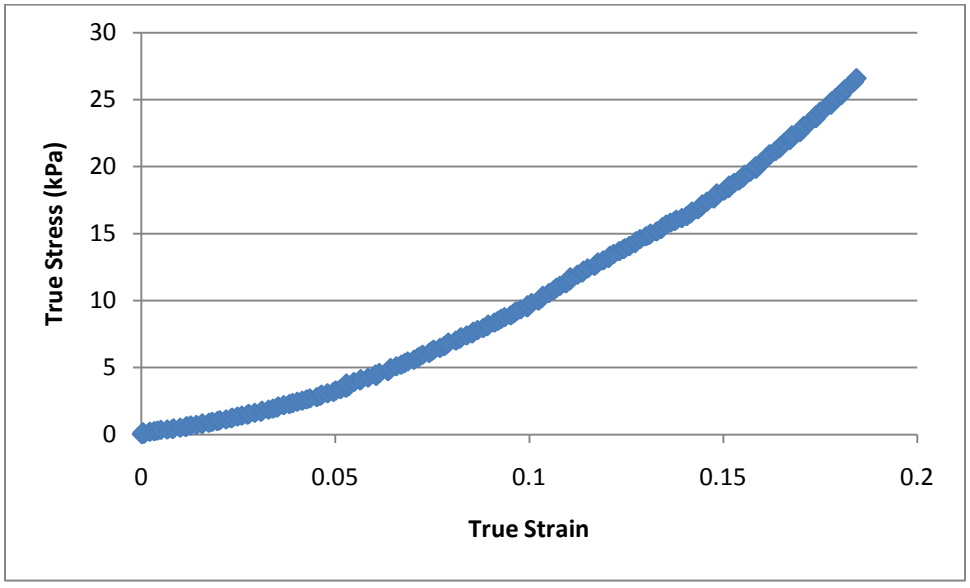
30
25
20
15
10
5
0
True Stress (kPa)
0
0.05
0.1
0.15
0.2
True Strain

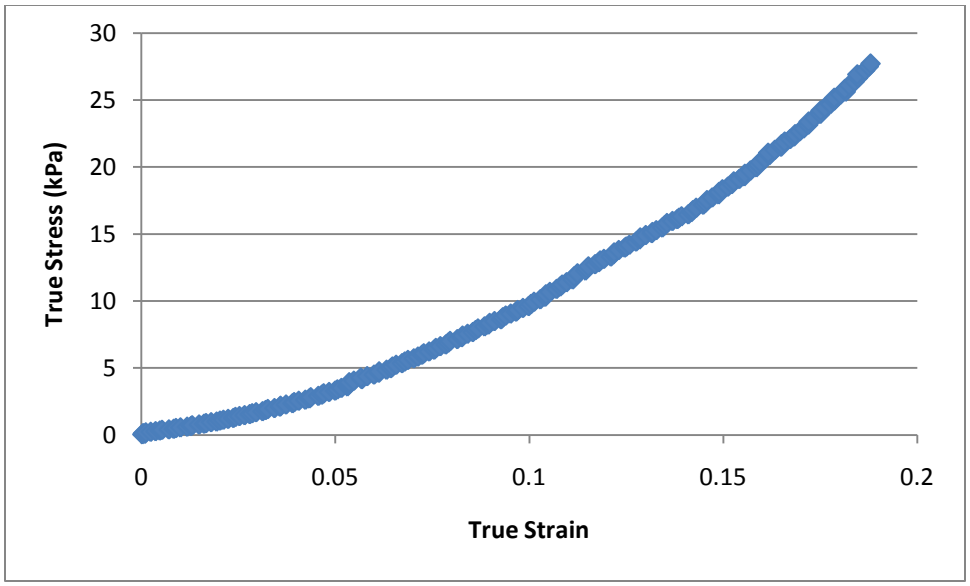
True Stress (kPa)
30
25
20
15
10
5
0
0
0.05
0.1
0.15
0.2
True Strain

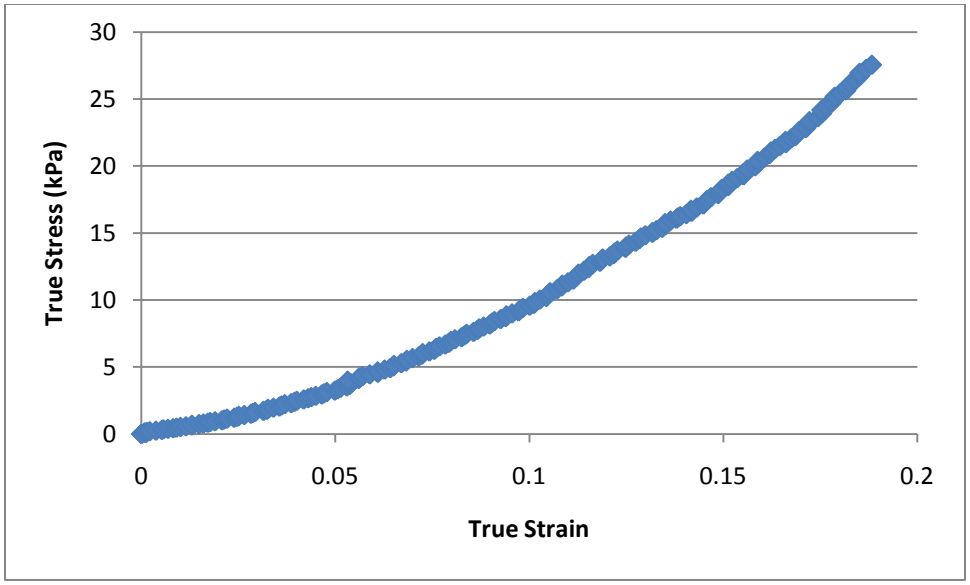
True Stress (kPa)
30
25
20
15
10
5
0
0
0.05
0.1
0.15
0.2
True Strain

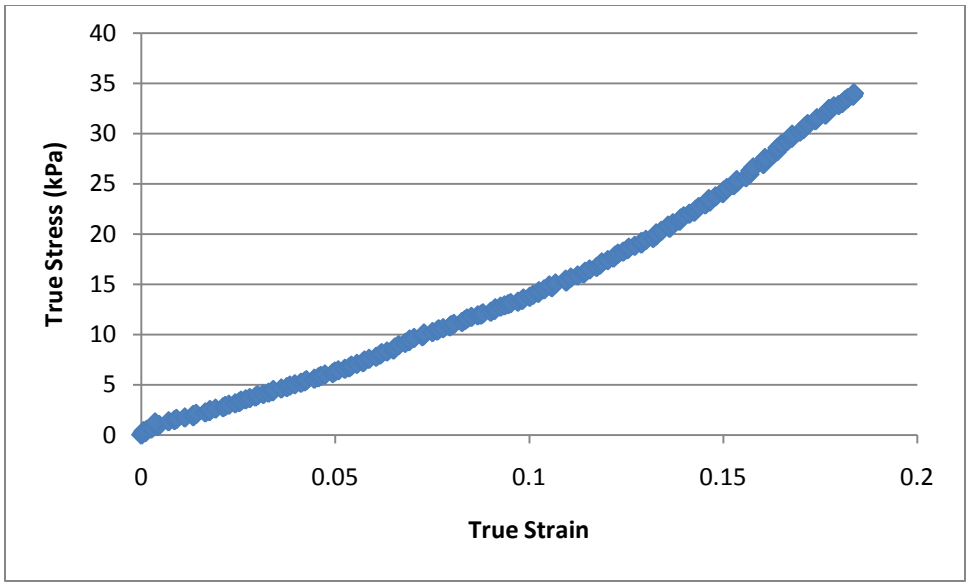
40
35
30
25
20
15
10
5
0
True Stress (kPa)
0
0.05
0.1
0.15
0.2
True Strain

A.3.4 HD-2-Fe^{2+}

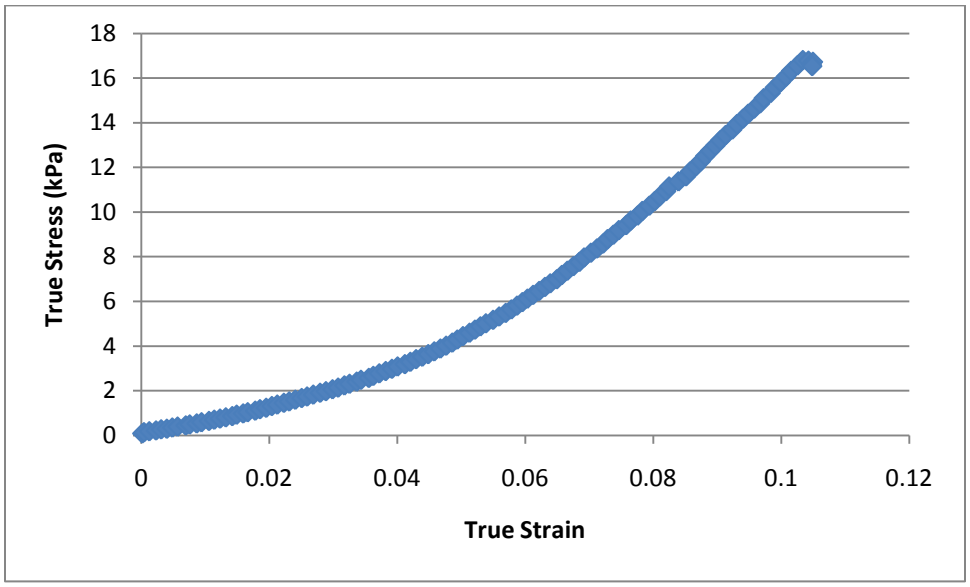
18
16
14
12
10
8
6
4
2
0
True Stress (kPa)
0
0.02
0.04
0.06
0.08
0.1
0.12
True Strain

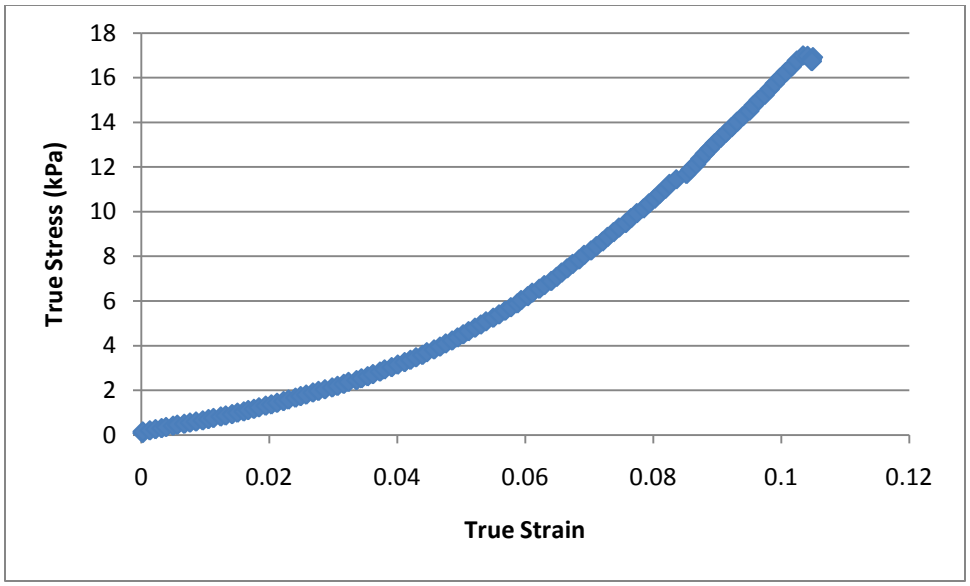
True Stress (kPa)
18
16
14
12
10
8
6
4
2
0
0
0.02
0.04
0.06
0.08
0.1
0.12
True Strain

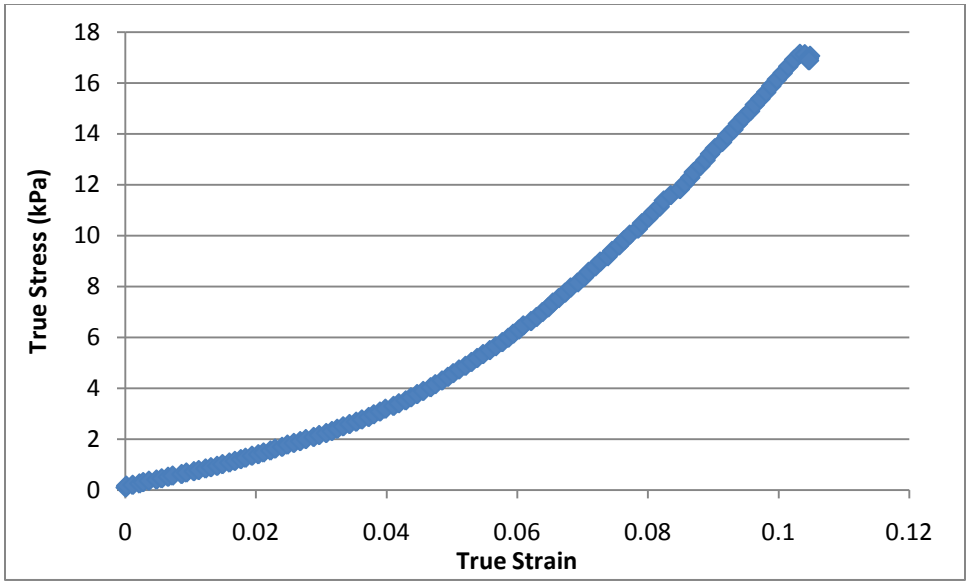
True Stress (kPa)
18
16
14
12
10
8
6
4
2
0
0
0.02
0.04
0.06
0.08
0.1
0.12
True Strain

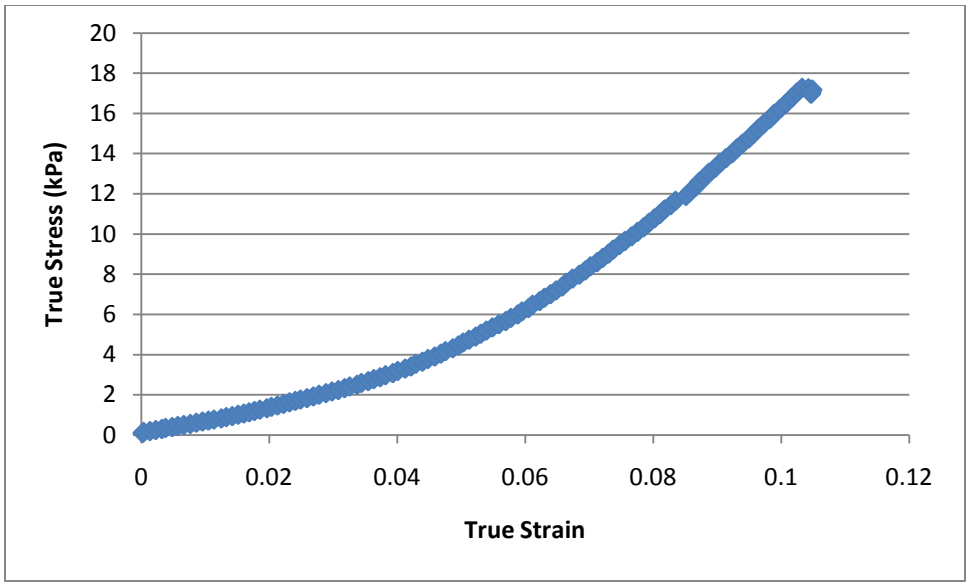
True Stress (kPa)
20
18
16
14
12
10
8
6
4
2
0
0
0.02
0.04
0.06
0.08
0.1
0.12
True Strain

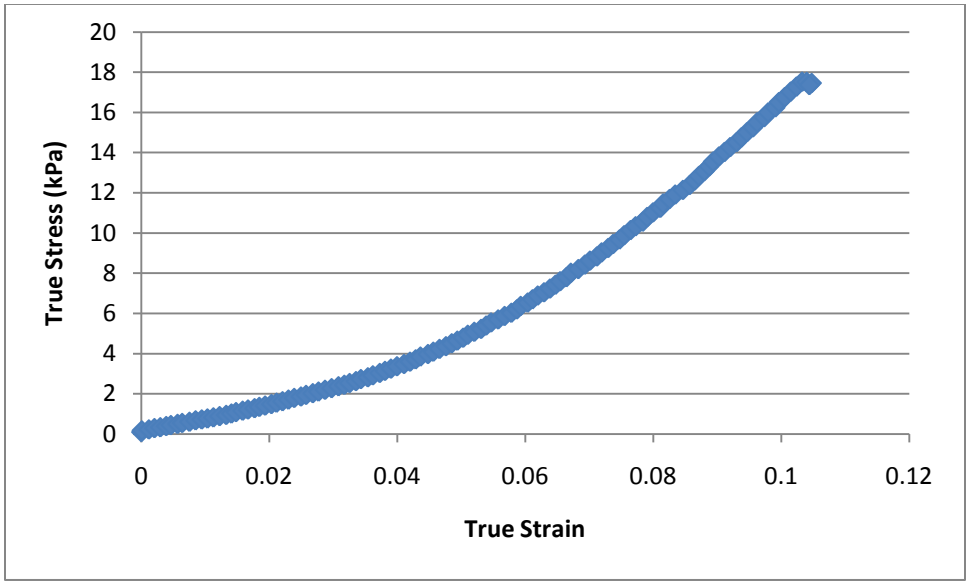
True Stress (kPa)
20
18
16
14
12
10
8
6
4
2
0
0
0.02
0.04
0.06
0.08
0.1
0.12
True Strain

A.3.5 HD-2-Fe^{3+}

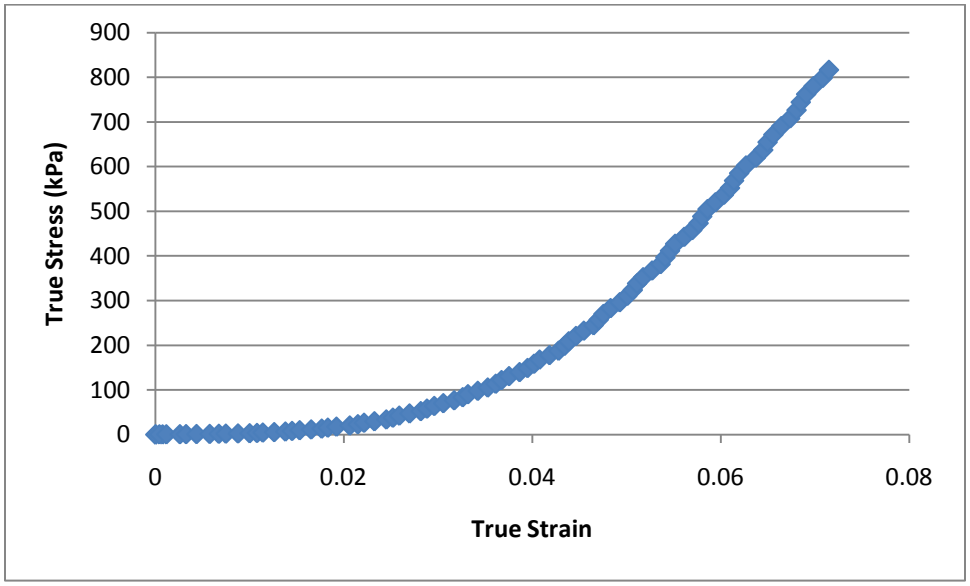
900
800
700
600
500
400
300
200
100
0
True Stress (kPa)
0
0.02
0.04
0.06
0.08
True Strain

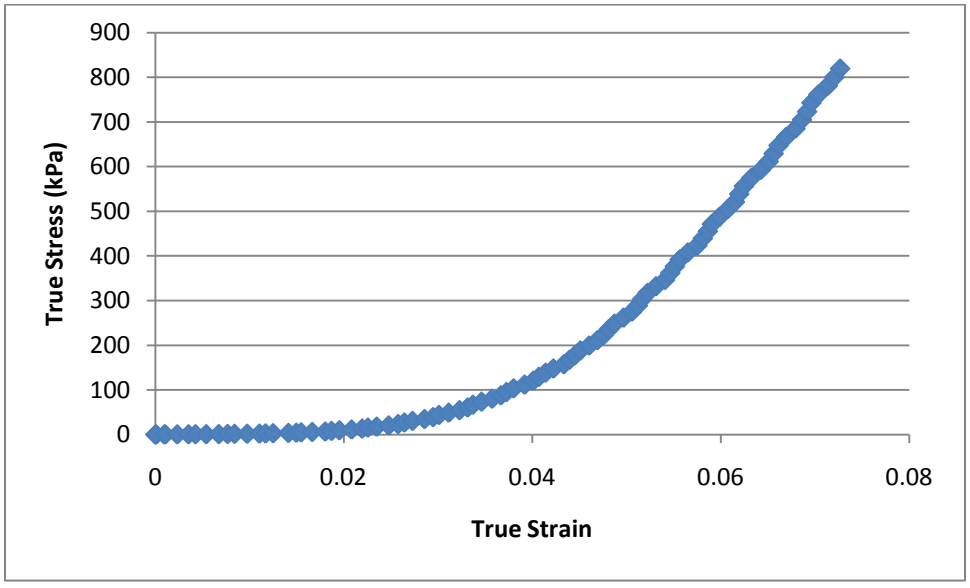
900
800
700
600
500
400
300
200
100
0
True Stress (kPa)
0
0.02
0.04
0.06
0.08
True Strain

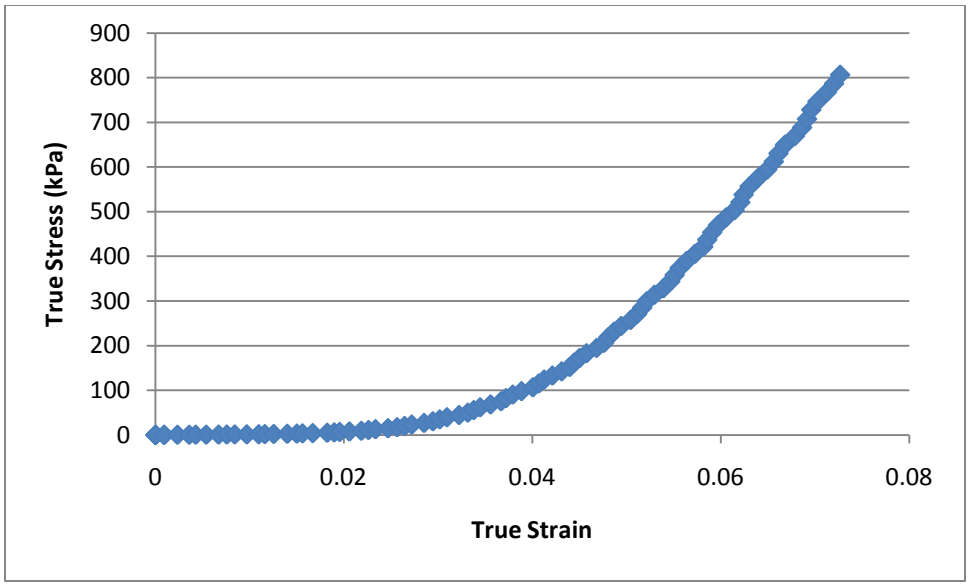
900
800
700
600
500
400
300
200
100
0
True Stress (kPa)
0
0.02
0.04
0.06
0.08
True Strain

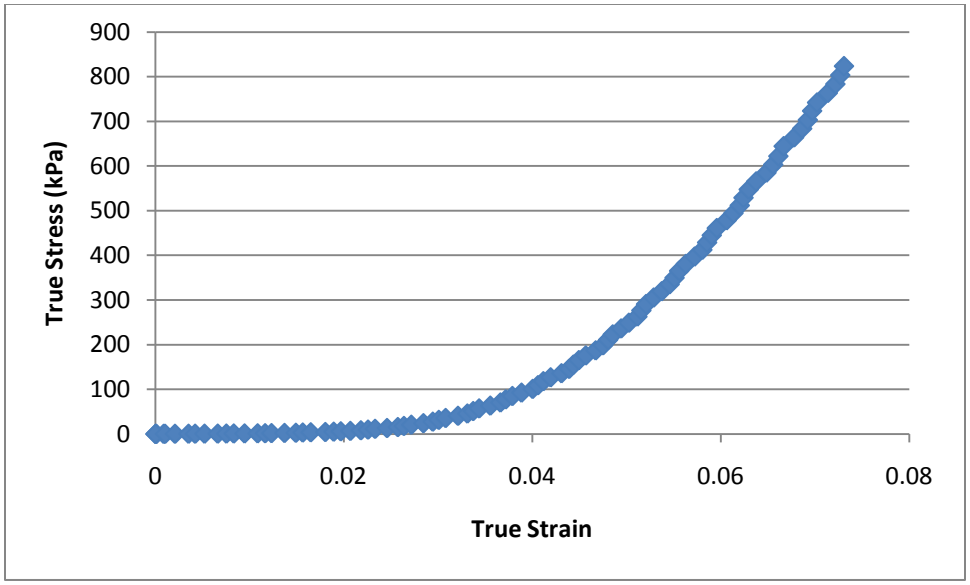
900
800
700
600
500
400
300
200
100
0
True Stress (kPa)
0
0.02
0.04
0.06
0.08
True Strain

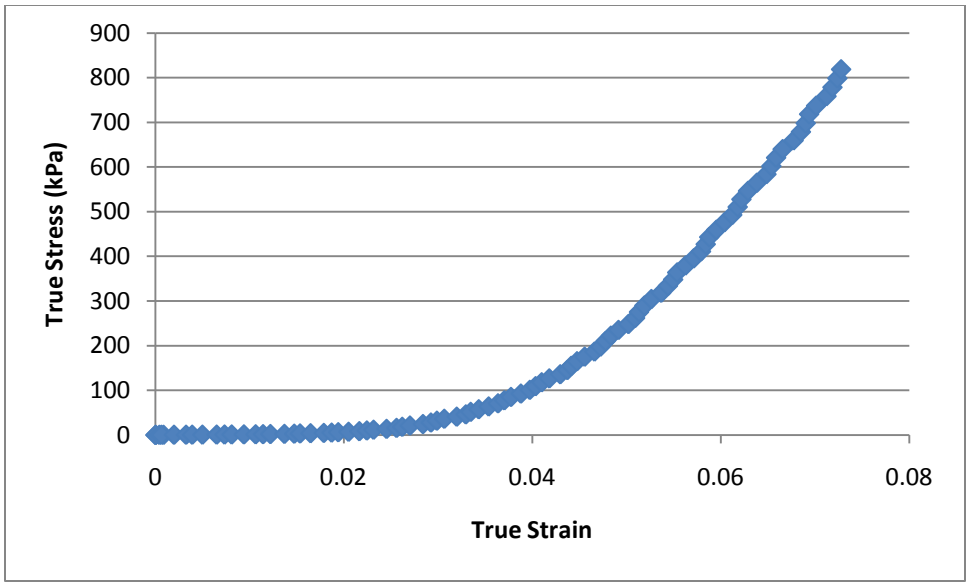

A.4 SINGLE SAMPLE TRANSITION RESULTS

A.4.1 EPE "Soft" State (HD-2-Fe^{2+})

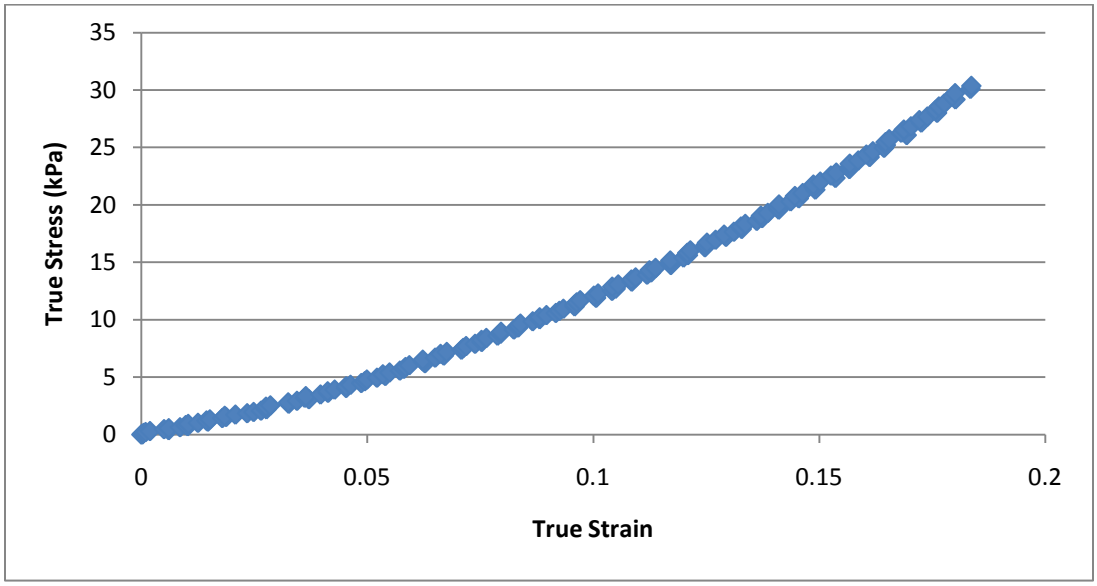

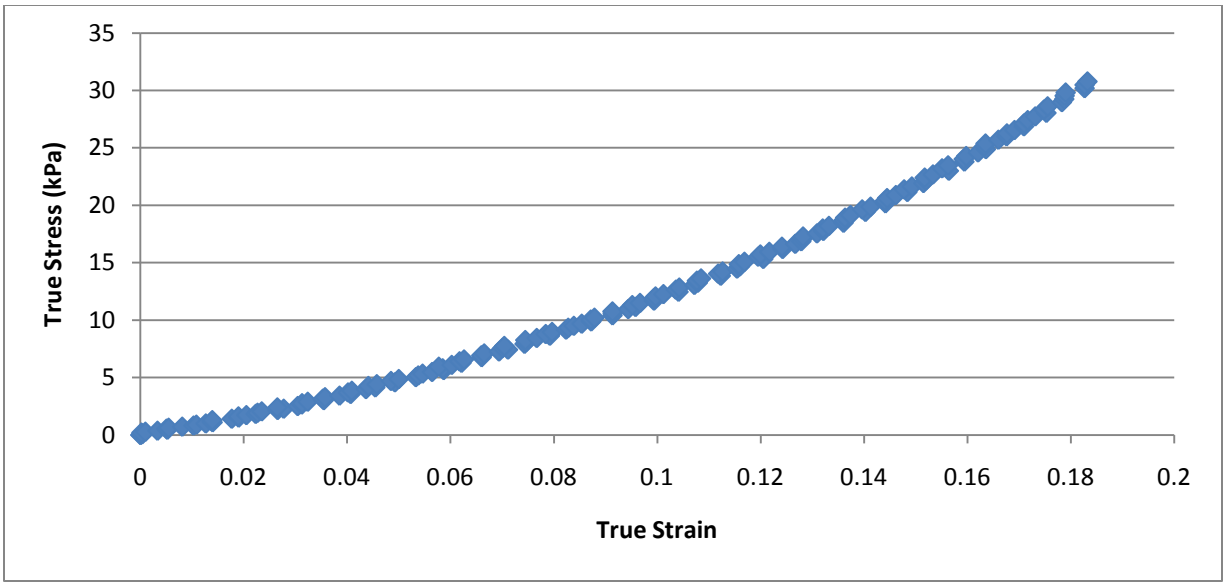
True Stress (kPa)
35
30
25
20
15
10
5
0
0
0.02
0.04
0.06
0.08
0.1
0.12
0.14
0.16
0.18
0.2
True Strain

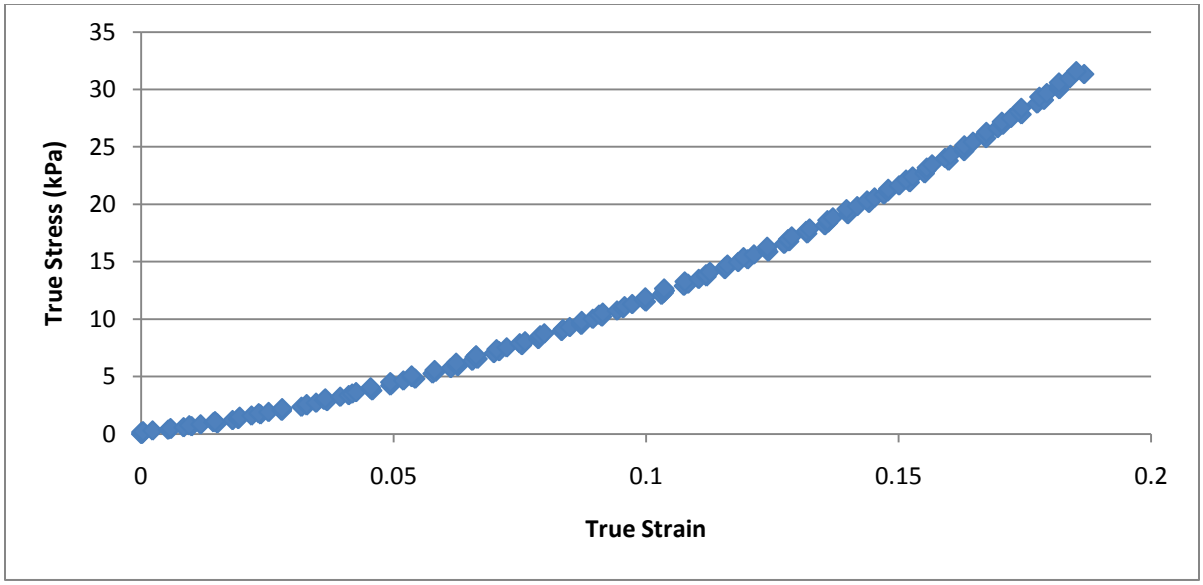
True Stress (kPa)
35
30
25
20
15
10
5
0
0
0.05
0.1
0.15
0.2
True Strain

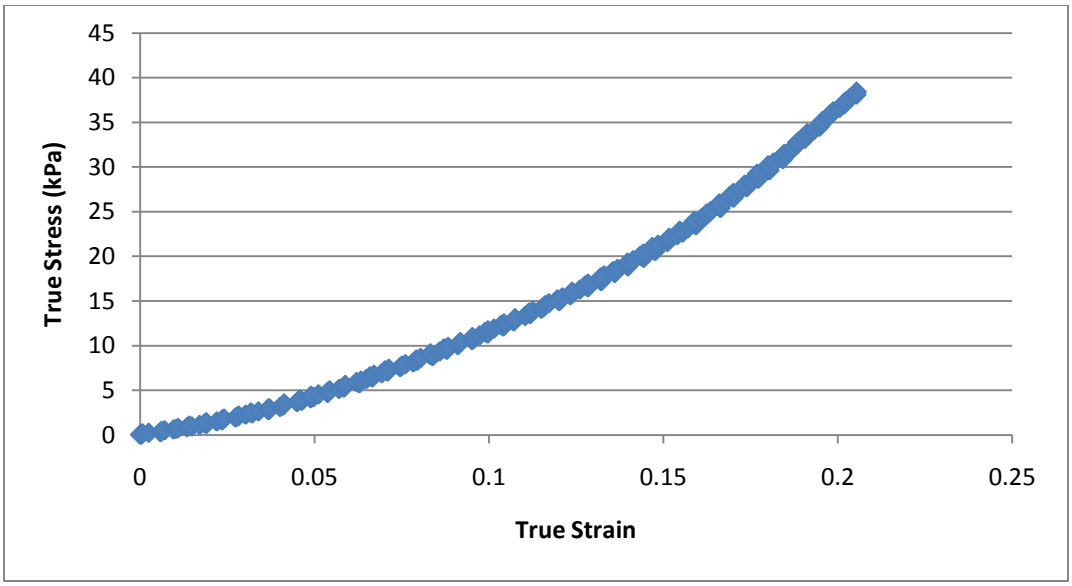
45
40
35
30
25
20
15
10
5
0
True Stress (kPa)
0
0.05
0.1
0.15
0.2
0.25
True Strain

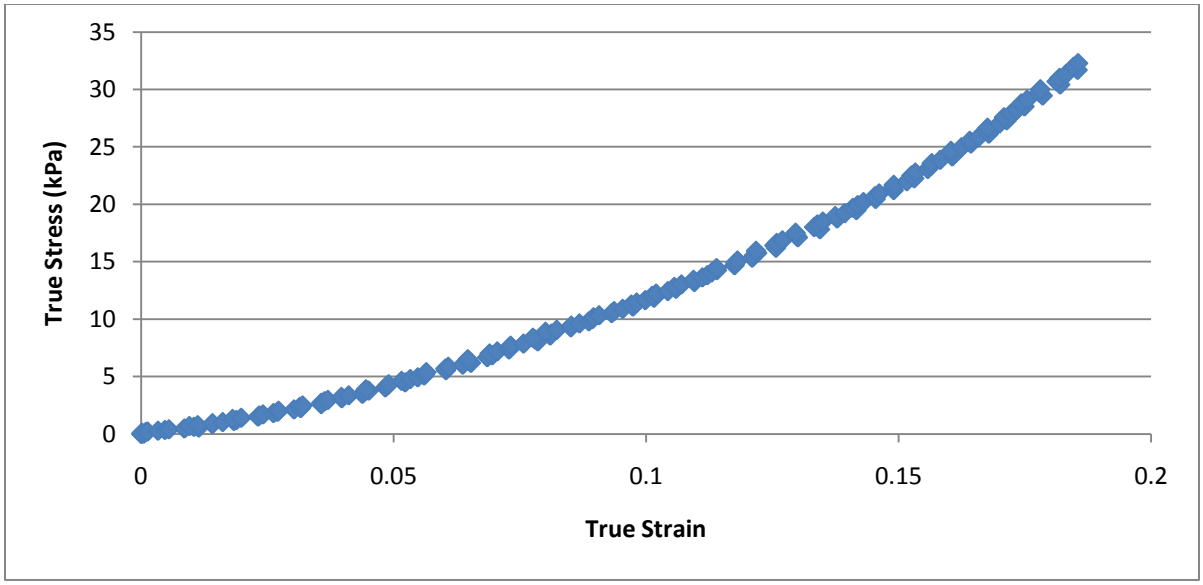
35
30
25
20
15
10
5
0
True Stress (kPa)
0
0.05
0.1
0.15
0.2
True Strain

A.4.2 EPE "Hard" State (HD-2-Fe^{3+})

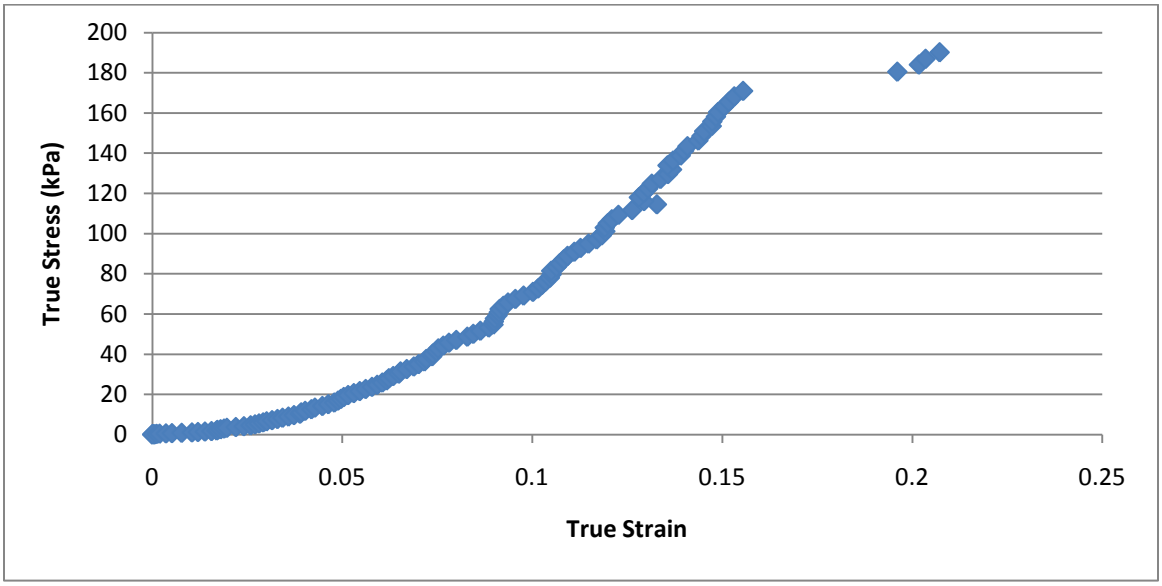

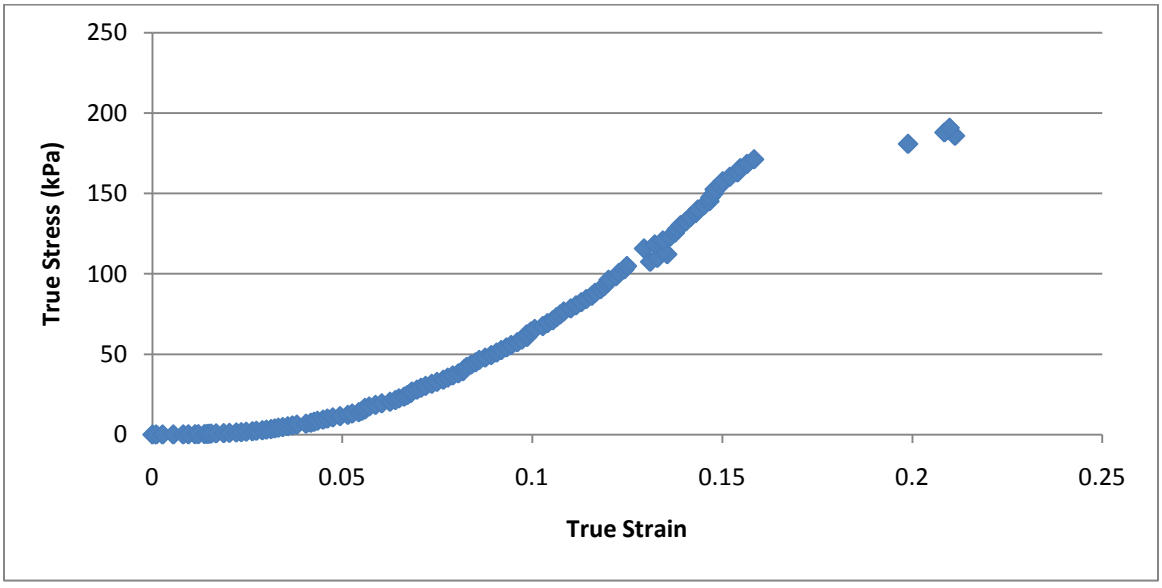

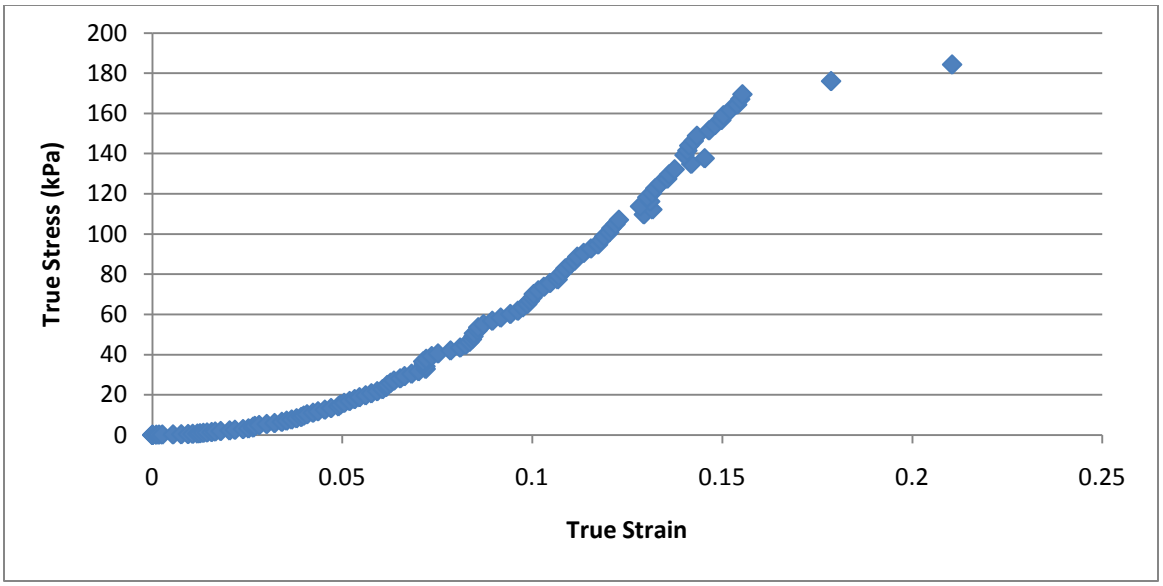
True Stress (kPa)
200
180
160
140
120
100
80
60
40
20
0
0
0.05
0.1
0.15
0.2
0.25
True Strain

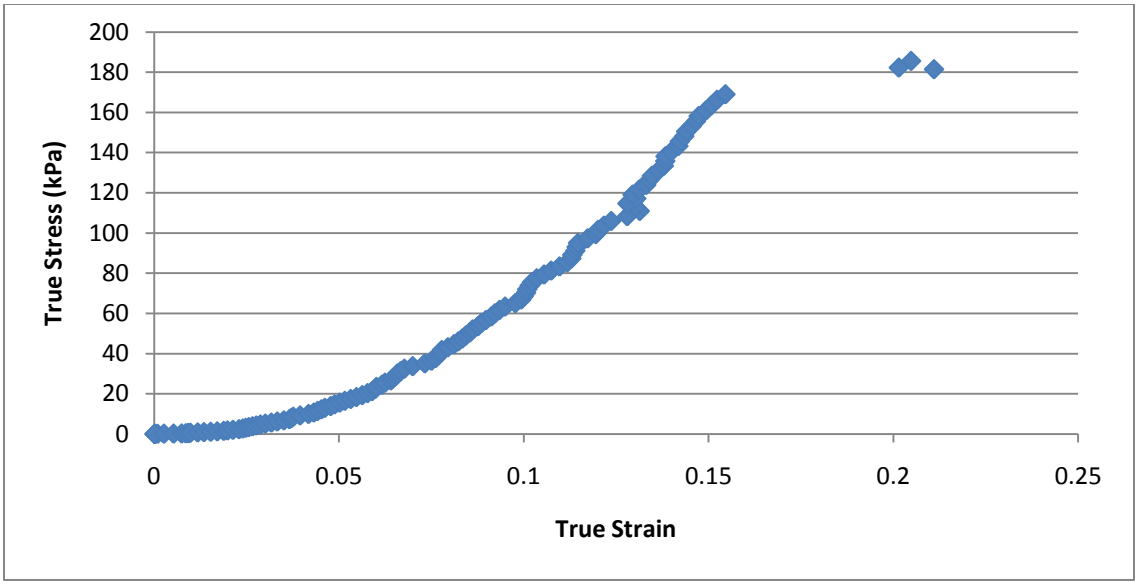
True Stress (kPa)
200
180
160
140
120
100
80
60
40
20
0
0
0.05
0.1
0.15
0.2
0.25
True Strain

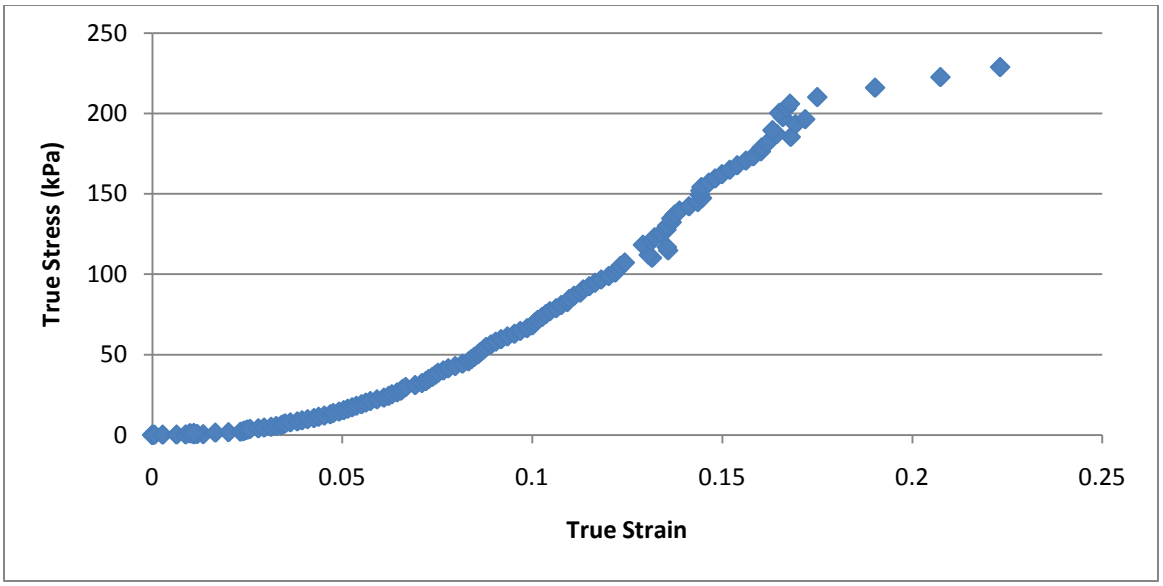

A.5 ELECTRIC CURRENT COMPRESSION TESTS

A.5.1 Current On

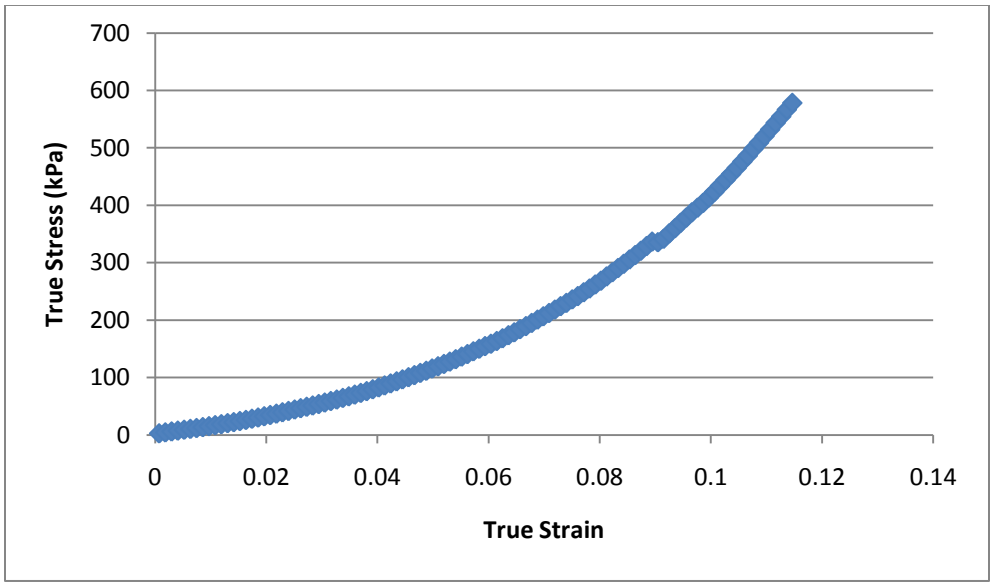

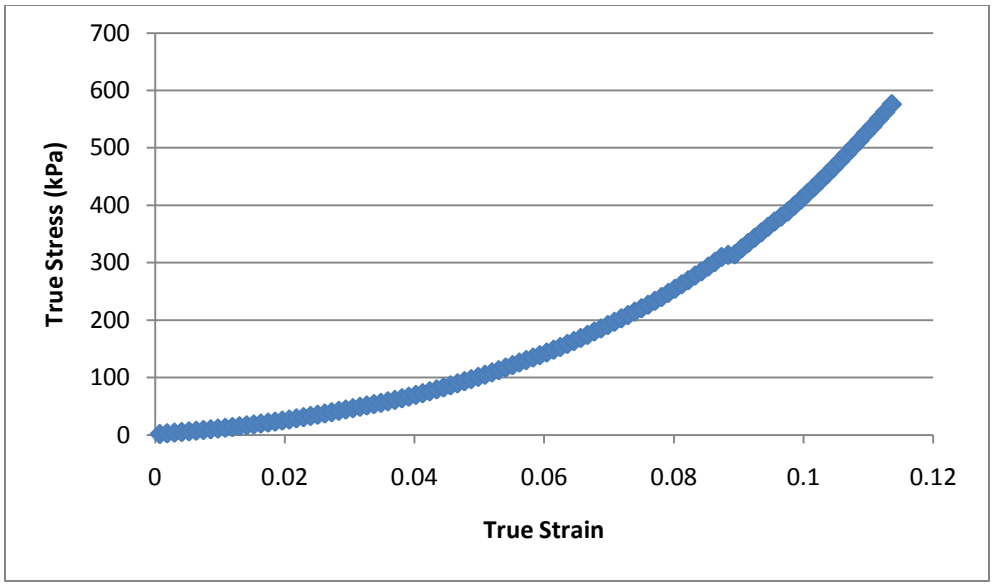
700
600
500
400
300
200
100
0
True Stress (kPa)
0
0.02
0.04
0.06
0.08
0.1
0.12
True Strain

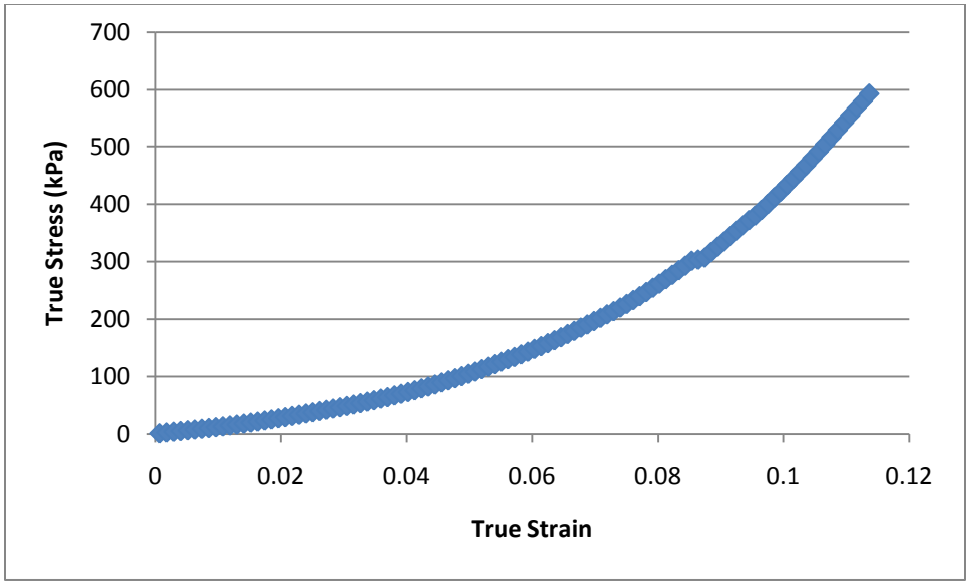
700
600
500
400
300
200
100
0
True Stress (kPa)
0
0.02
0.04
0.06
0.08
0.1
0.12
True Strain

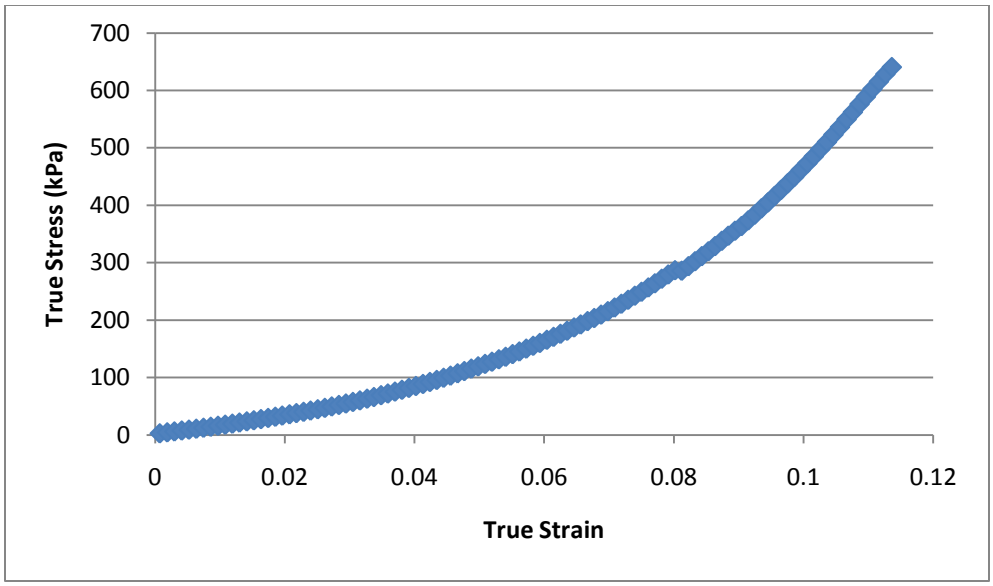
700
600
500
400
300
200
100
0
True Stress (kPa)
0
0.02
0.04
0.06
0.08
0.1
0.12
True Strain

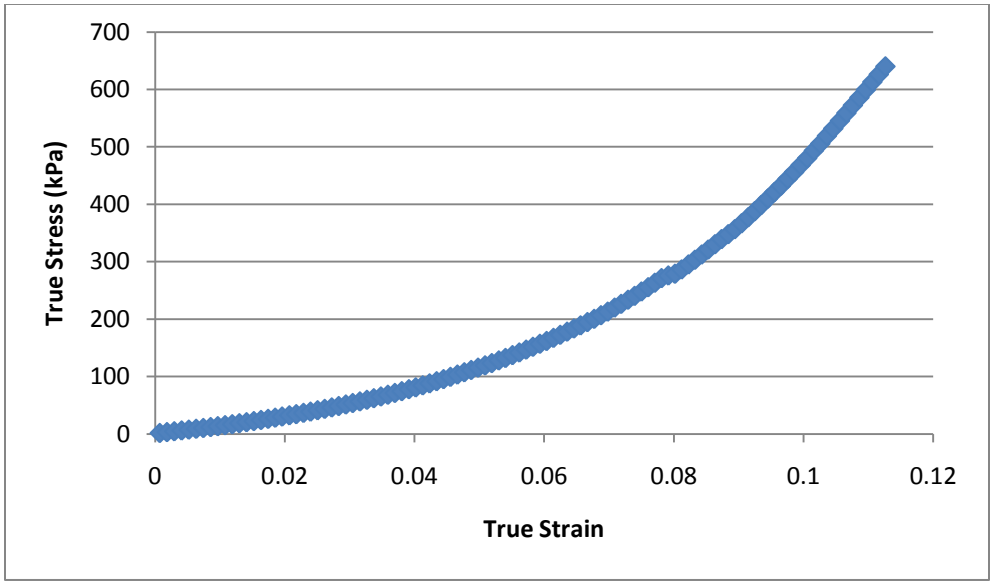
700
600
500
400
300
200
100
0
True Stress (kPa)
0
0.02
0.04
0.06
0.08
0.1
0.12
True Strain

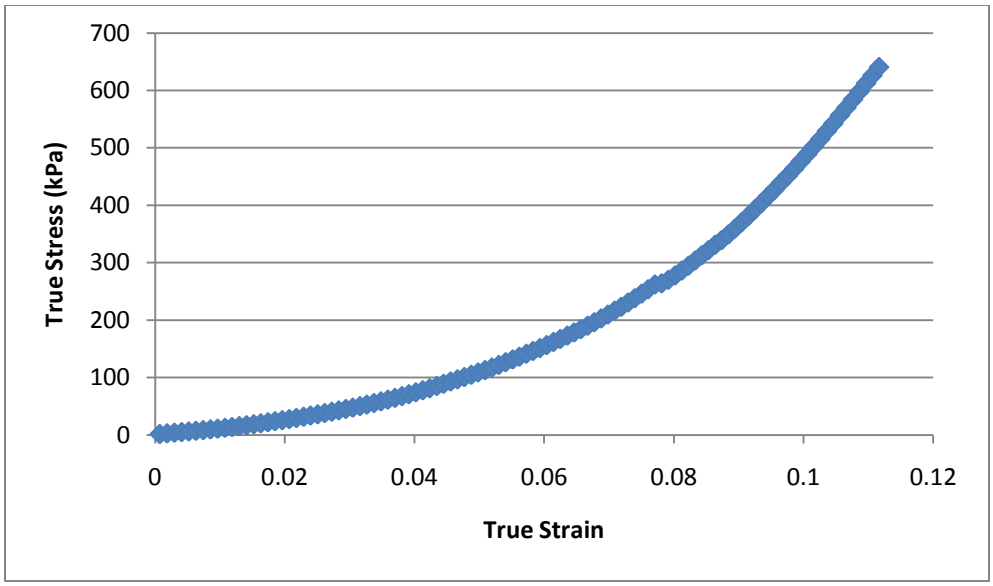
700
600
500
400
300
200
100
0
True Stress (kPa)
0
0.02
0.04
0.06
0.08
0.1
0.12
True Strain

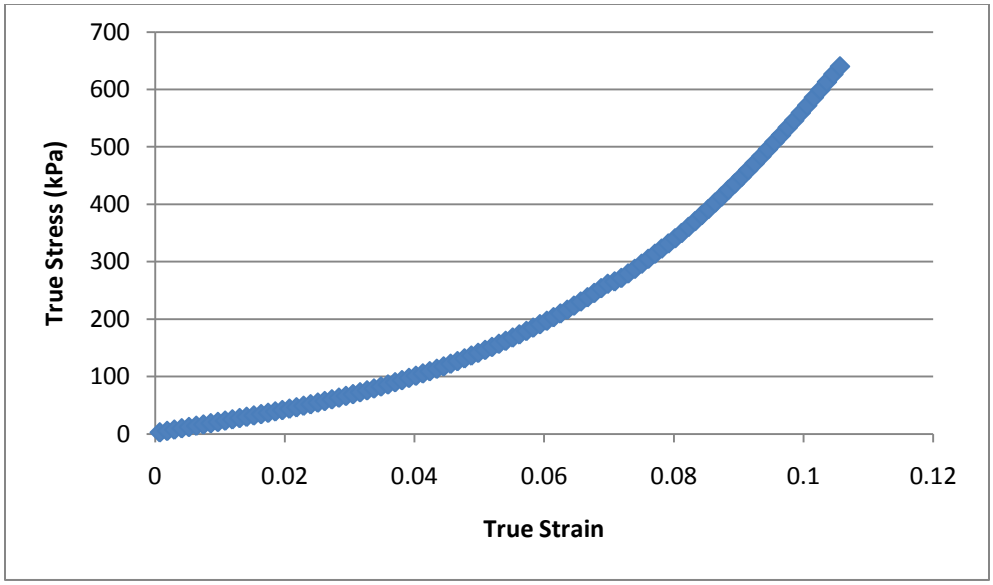
700
600
500
400
300
200
100
0
True Stress (kPa)
0
0.02
0.04
0.06
0.08
0.1
0.12
True Strain

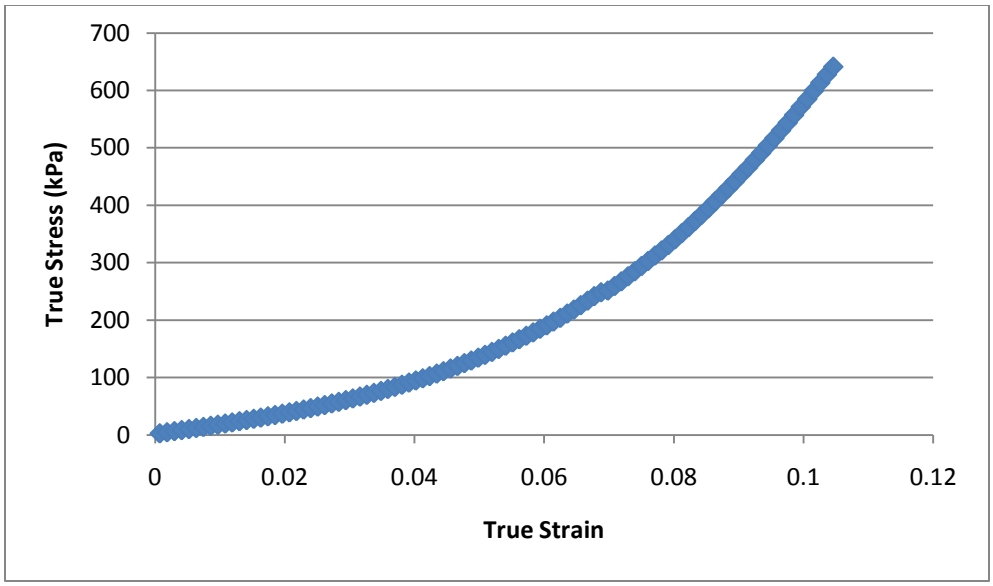
700
600
500
400
300
200
100
0
True Stress (kPa)
0
0.02
0.04
0.06
0.08
0.1
0.12
True Strain

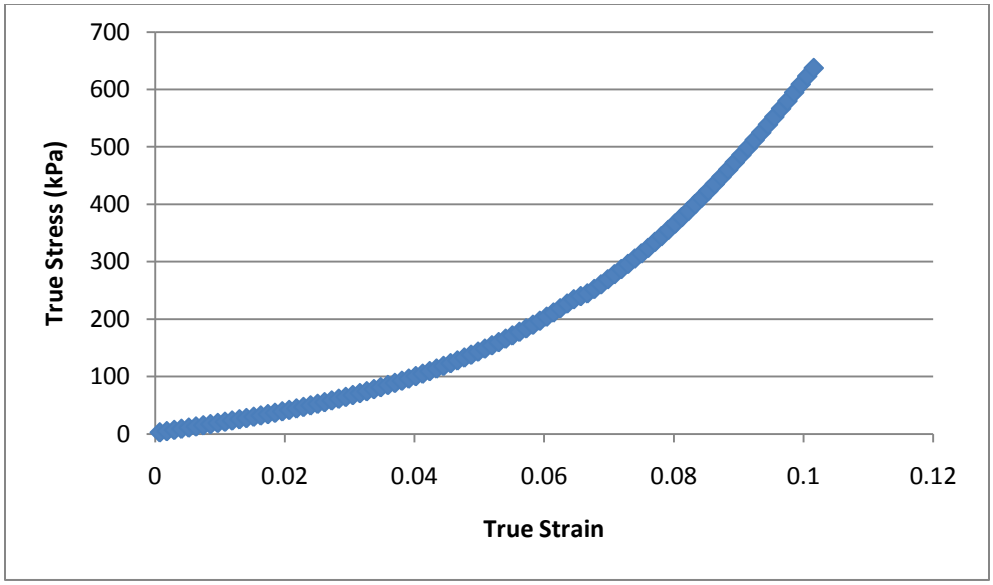
700
600
500
400
300
200
100
0
True Stress (kPa)
0
0.02
0.04
0.06
0.08
0.1
0.12
True Strain

A.5.2 Current Off

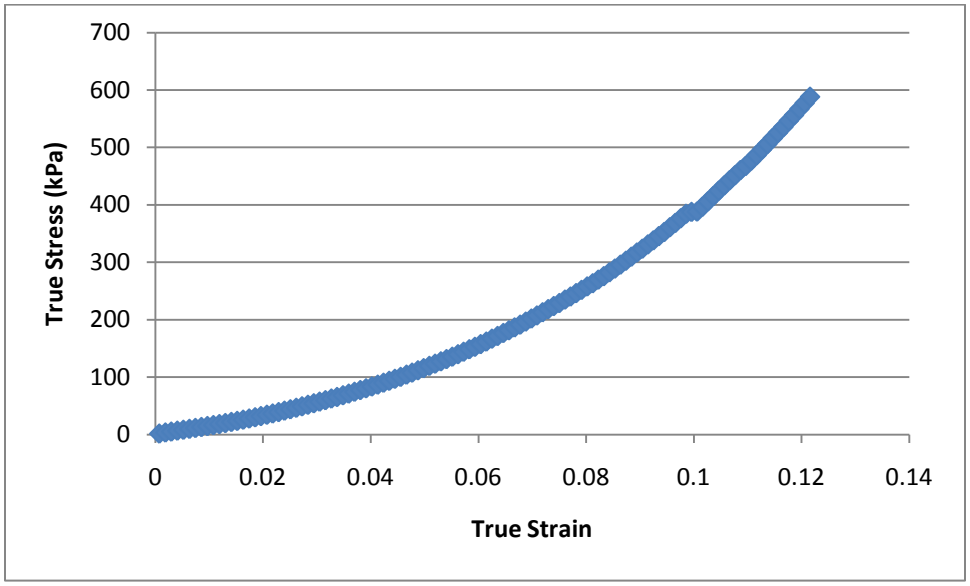

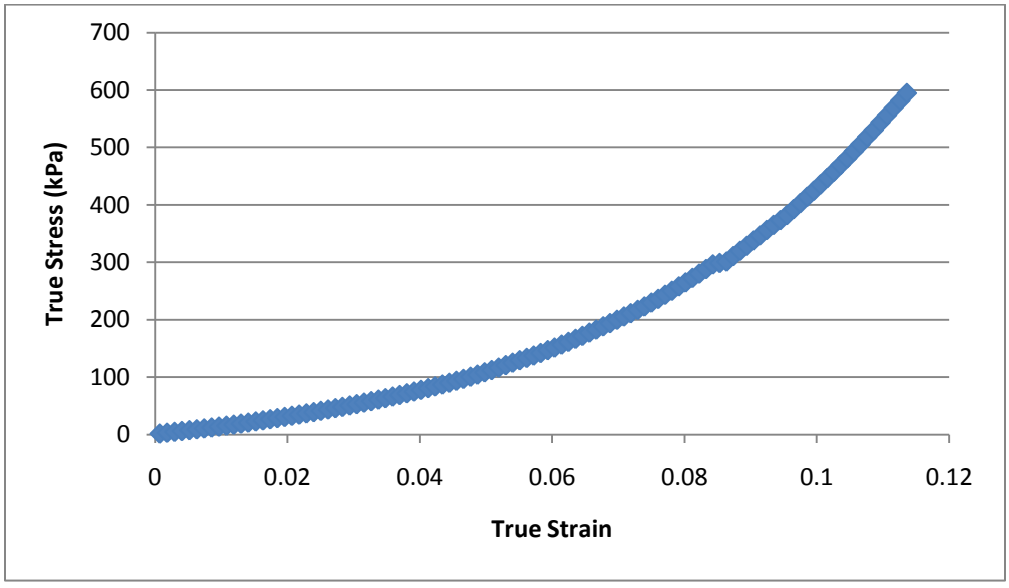

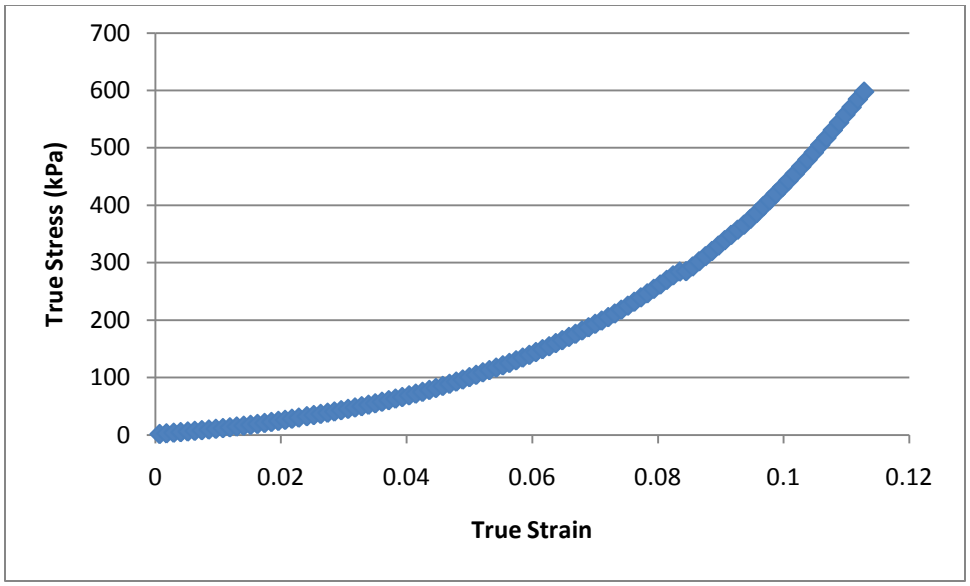
700
600
500
400
300
200
100
0
True Stress (kPa)
0
0.02
0.04
0.06
0.08
0.1
0.12
True Strain

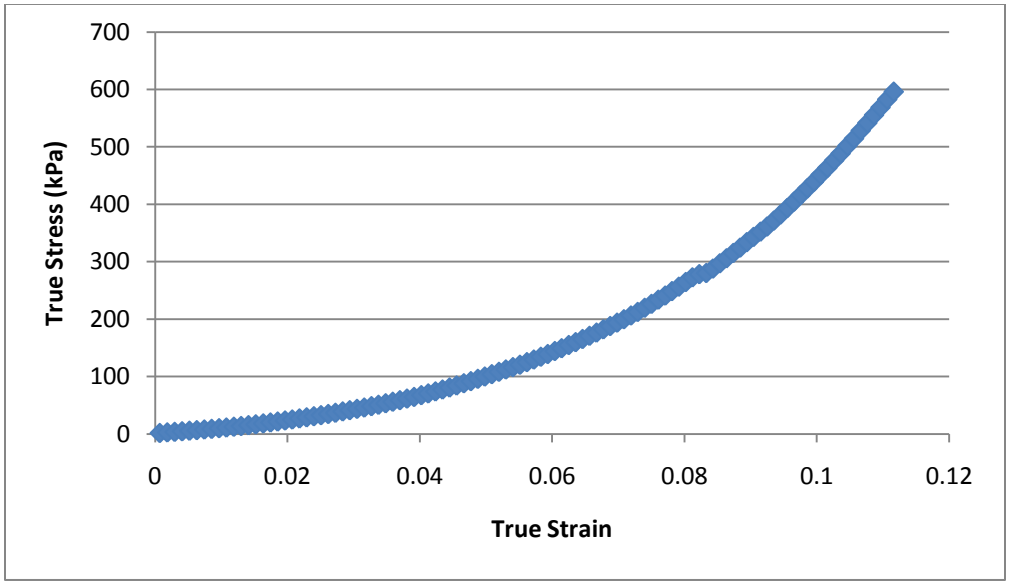
700
600
500
400
300
200
100
0
True Stress (kPa)
0
0.02
0.04
0.06
0.08
0.1
0.12
True Strain

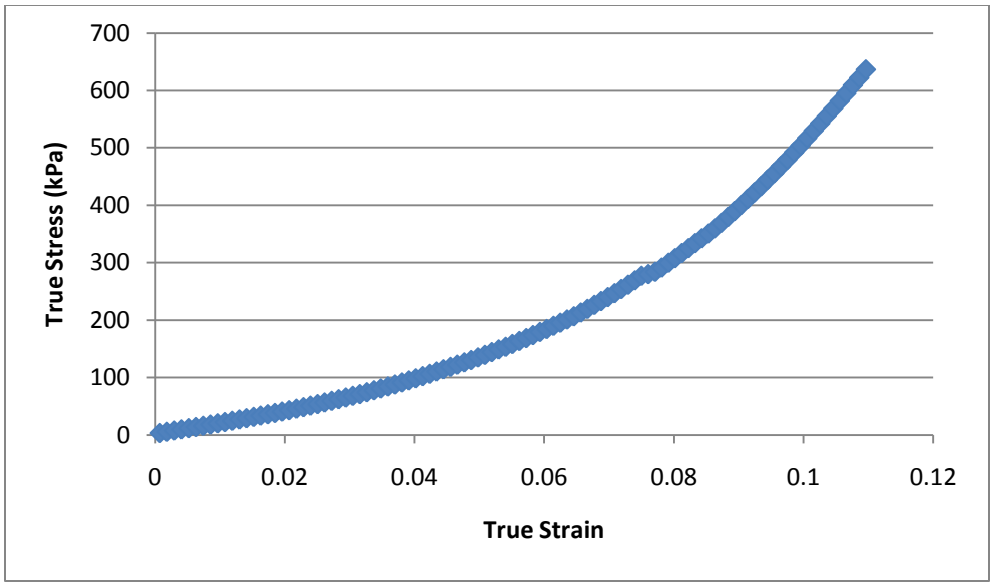
700
600
500
400
300
200
100
0
True Stress (kPa)
0
0.02
0.04
0.06
0.08
0.1
0.12
True Strain

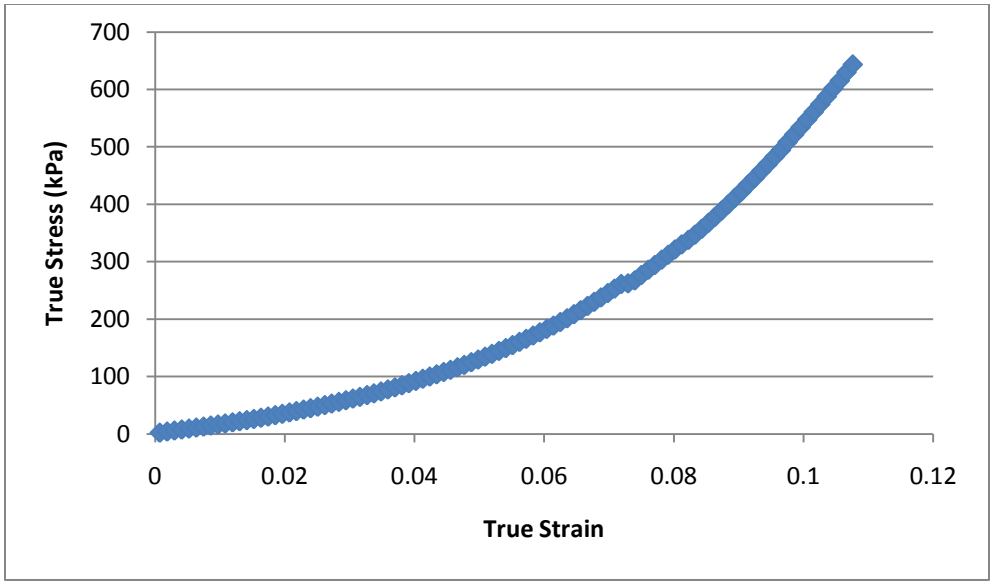
700
600
500
400
300
200
100
0
True Stress (kPa)
0
0.02
0.04
0.06
0.08
0.1
0.12
True Strain

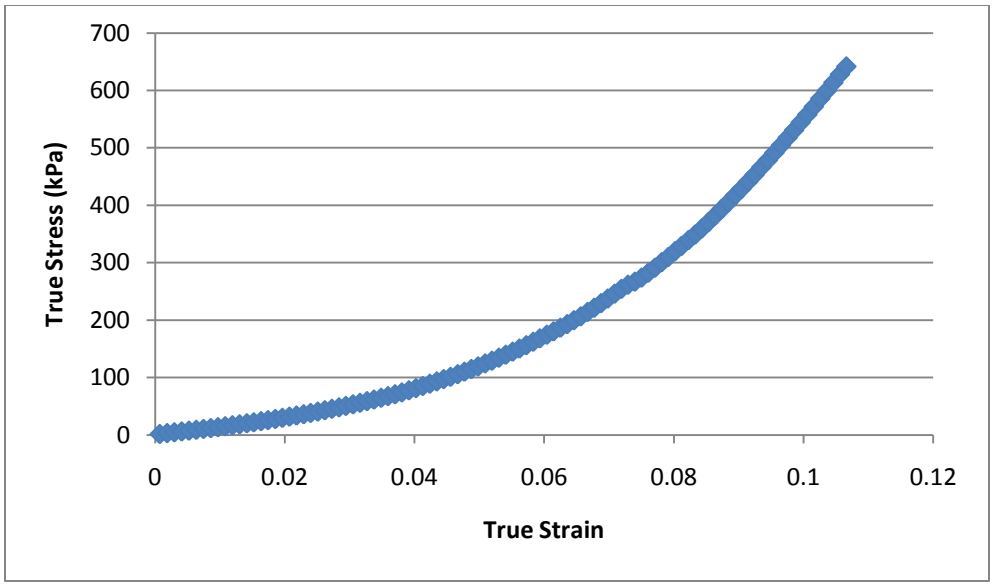
700
600
500
400
300
200
100
0
True Stress (kPa)
0
0.02
0.04
0.06
0.08
0.1
0.12
True Strain

APPENDIX B

INDENTATION TESTING

The following appendix provides additional details regarding the multi sample indenter (MSI) and subsequent indentation testing on control foams. A detailed description of the MSI operating procedure is given followed by results and conclusions drawn from indentation tests on three different types of foam samples.

B.1 MSI SET UP AND TESTING PROCEDURE

Before starting the testing procedure, basic .txt files for each individual sample are created for the purpose of storing force measurements. The Labview based DAQ software needs to be told which file to save the force measurements to prior to each individual indentation test. All samples are then placed on marked grid of the indenter's movable platform. The MSI will begin the testing procedure as soon as the power is switched on. Initially, the testing probe will begin to descend in the negative z direction until making contact with the surface of the sample. At this point, the probe will pause and a red LED will light on the circuit board. This indicates that testing is in progress and at this time, the DAQ program should be initiated. Following this

approximately five second pause, the probe will descend further, causing a specified 3mm indentation into the sample. The forces required to cause this indentation are simultaneously measured by the DAQ software on the screen and a plot of force readings is produced. At this point, the testing probe will retract to its original position, and the platform will move in the x direction, allowing for the next sample to be tested. This process is repeated for the first 4 samples. Upon testing sample four, a yellow LED will light on the circuit board, indicating that the platform will now begin moving in the opposite x direction. At this point, the platform must manually be moved in the y direction to line up the testing probe with the next row of samples. Once testing is complete, all force measurements for each test are available in the text files assigned prior to each test.

B.2 CONTROL FOAM INDENTATION TESTS

Foam samples consisting of vinyl and silicon foams as well as Buna-N-foam, which are homogeneous from a mechanical standpoint, are tested using the MSI. Because the MSI is a custom device, it is important that the long term operational capabilities are determined before full device implementation. In addition, measurements acquired via indentation testing of homogeneous materials will allow insight into typical statistical spreads accompanied with MSI measurements. Table B.1 contains the results of these tests.

Table B.1: Indentation test results (control foams)

# of Tests (N)	Foam Type	Modulus (kPa)	Standard Deviation	95 % Confidence Interaval
N = 6	Buna-N-Foam	151 kPa	27 kPa	123 – 179 kPa
N = 4	Silicon Foam	194 kPa	44 kPa	124 – 264 kPa
N = 7	Vinyl Foam	174 kPa	19 kPa	157 – 191 kPa

Examination of Table B.1 clearly indicates that MSI measurements are accompanied by a rather larger statistical spread, especially when compared to typical spreads produced by compression testing. Sources of error contributing to this significant spread are most likely due to the employed 5lb load cell. The load cell has two main deficiencies; (1) poor resolution, which likely contributes to (2) noisy force – time plots in which the peak force may be difficult to discern. Poor resolution in measurement devices often results in larger than usual standard deviations, as is likely the case here. To this end, the implementation of a new load cell is being examined.

Secondly, the results of the aforementioned tests indicate that calibration of the MSI is retained over the course of many tests. In addition to the foam samples, the above indentation tests were performed concurrently with thin film iron (II) and iron (III) samples, the results of which are reported in Section 5.3.2. Over the course of multiple tests, there is no discernable change in the operating capabilities of the MSI as the outlier measurements occur at random as opposed to the beginning or the end of the indentation testing cycle. This fact is demonstrated in Table B.2.

Table B.2. Indentation test results (control foams) in sequential order

Buna-N-Foam		**Vinyl Foam**		**Silicon Foam**	
Test	Modulus	Test	Modulus	Test	Modulus
1	131 kPa	1	182 kPa	1	214 kPa
2	110 kPa	2	164 kPa	2	228 kPa
3	175 kPa	3	164 kPa	3	204 kPa
4	178 kPa	4	154 kPa	4	129 kPa
5	152 kPa	5	203 kPa	X	-
6	162 kPa	6	159 kPa	X	-
X	-	7	192 kPa	X	-

REFERENCES

1. D.J. Leo. *Engineering Analysis of Smart Material Systems*. 2007, John Wiley & Sons, Inc.

2. A.J. Grodzinsky and J. R. Melcher. *Electromechanical Transduction with Charged Polyelectrolyte Membranes*. IEEE Transactions on Biomedical Engineering, 1976, **23**(6).

3. W. Kuhn, B. Hargitay, A. Katchalsky, H. Eisenberg. *Reversible Dilation and Contraction by Changing the State of Ionization of High-Polymer Acid Networks*. Nature, 1950, **165**.

4. M.E. Lines and A.M. Glass. *Principles and Applications of Ferroelectrics and Related Materials.* 2001, Oxford University Press Inc.

5. B. Jaffe, W.R. Cooke, and H. Jaffe. *Piezoelectric Ceramics*. 1971, The Academic Press Limited.

6. Overview of Smart Materials Technology. [cited; Available from: http://resources.edb.gov.hk/physics/articleIE/smartmaterials/SmartMaterials_e.htm.

7. L.C. Lim, K.K. Rajan, and J. Jing. *Characterization of Flux-Grown PZN-PT Single Crystals for High Performance Piezo Devices.* IEEE Transactions on Ultrasonics, Ferroelectrics, and Frequency Control, 2007, **54**(12).

8. Y. Bar-Cohen. *Electroactive Polymer (EAP) Actuators as Artificial Muscles: Reality, Potential, and Challenges.* 2001, SPIE, The International Society for Optical Engineering.

9. L.M. Swallo, J.K. Luo, I. Patel, and D. Dodds. *A Piezoelectric Fibre Composite Based Energy Harvesting Device for Potential Wearable Applications*. Smart Mater. Struct, 2008, **17.**

10. R. Guigon, J-J. Chaillout, T. Jager, and G. Despesse. *Harvesting Raindrop Energy:Ttheory.* Smart Mater. Struct., 2004, **17**.

11. V. H. Schmidt. *Piezoelectric Energy Conversion in Windmills.* Proc. IEEE Ultrasonic Symp., 1992, pp 897-904.

12. S. Horowitz, A. Kasyap, F. Liu, D. Johnson, T. Nishida, K. Ngo, M. Sheplak and L. Cattafesa. *Technology Development of Self-Powered Sensors.* 1st Flow Conf. (St. Louis, MO) 2002.

13. H.A. Sodano, G. Park, D.J. Leo, and D.J. Inman. *Model of Piezoelectric Power Harvesting Beam.* ASME Int. Mechanical Engineering Congr. And Rd&D Exp, 2003.

14. D. C. Lagoudas. *Shape Memory Alloys – Modeling and Engineering Applications.* 2008, Springer Publishing Co.

15. Shape Memory Alloys. [cited; Available from: http://www.cs.ualberta.ca/~database/MEMS/sma_mems/sma.html.

16. C. Liu, H. Qin, and P.T. Mather. *Review of Progress in Shape Memory Polymers.* Journal of Materials Chemistry, 2007, **17**.

17. S. Saddat, J. Salichs, M. Noori, Z. Hou, H. Davoodi, I.Bar-on. *An Overview of Vibrations and Seismic Applications of NiTi Shape Memory Alloys.* Smart Mater. Struct., 2002, **11**.

18. CRG Industries: Overview of SMP. [cited; Available from http://www.crgrp.net/overviews/smp2.shtml.

19. P.J. Flory. *Statistical Mechanics of Chain Molecules.* 1988, Hanser Publisher.

20. Y. Liu, K. Gall, M.K. Dunn, A.R. Greenberg, J. Diani. *Thermomechanics of Shape Memory Polymers: Uniaxial Experiments and Constitutive Modeling.* International Journal of Plasticity, 2006 **22**.

21. R. V. Beblo and L.M. Weiland. *Light Activated Shape Memory Polymer Characterization.* Journal of Applied Mechanics, 2009, **76**.

22. Oosawa, F. *Polyelectrolytes*. 1971, Dekker.

23. Hara, M. *Polyelectrolytes: Science and Technology.* 1993, Marcel Dekker Inc.

24. Eisenberg, A. and Kim, J.-S. *Introduction to Ionomers*. 1998, Wiley.

25. W.Y. Hsu and T.D. Gierke. *Elastic Theory for Ionic Clustering in Perfluorinated Ionomers*. Macromolecules, 1982, **15**.

26. L.M Weiland, Gao, Fei. *A Multi-Scale Model Applied to Ionic Polymer Stiffness Prediction*. J. Mater. Res. 2008, **23**(3).

27. J.Y.Li and S. Nemat-Nasser. *Micromechanical Analysis of Ionic Clustering in Nafion Perfluorinated Membrane*. Mech. Mater, 2000, **32**.

28. L.M Weiland, D.J. Leo. *Computational Analysis of Ionic Polymer Cluster Energetics*. Journal of Applied Physics, 2005, **97**.

29. J.L. Matthews, E.K. Lada, L.M. Weiland, R.C. Smith, and D.J. Leo. *Monte Carlo Simulation of a Solvated Ionic Polymer With Cluster Morphology*. Smart Mater. Struct., 2006, **15**(1).

30. L.M. Weiland, E.K. Lada, R.C. Smith, and D.J. Leo. *Application of Rotational Isomeric State Theory to Ionic Polymer Stiffness Predictions*. *J. Mater. Res.*, 2005, **20**(9).

31. Schmidt-Rohr, and Chen, Q. *Parallel Cylindrical Water Nanochannels in Nafion Fuel-Cell Membranes*. Nature Materials, **2008, 7**(1).

32. S. Nemat-Nasser. *Micromechanics of Acuation of Ionic Polymer-Metal* Composites. Journal of Applied Physics, 2002, **92**(5).

33. J.S. Lee, N.D. Quan, J.M. Huang, S.D. Lee, H. Kim, H. Lee, and H.S. Kim. *Polymer Electrolyte Membranes for Fuel Cells*. J. Ind. Eng. Chem., 2006, **12**(2).

34. U.S. Department of Energy, Polymer Electrolyte Membrane (PEM) Fuel Cells. [cited; Available from http://www1.eere.energy.gov/hydrogenandfuelcells/fuelcells/fc_types.html.

35. M. Shahinpoor, Y. Bar-Cohen, J.O. Simpson, and J. Smith. *Ionic Polymer-Metal Composites (IPMCs) as Biomimetic Sensors, Actuators, and Artificial Muscles – A Review*. Smart Mater. Struct., 1998, **7**.

36. B. Akle, T. Wallmersperger, E. Akle, D. J. Leo. *High Surface Area Electrodes in Ionic Polymer Transducers.* Behavior and Mechanics of Multifunctional and Composite Materials. San Diego, Ca. 10 March 2008.

37. A.J. Duncan, D.J. Leo, and T.E. Long. *Beyond Nafion: Charged Macromolecules Tailored for Performance as Ionic Polymer Transducers*. Macromolecules, 2008, **41**(21).

38. H. Tamagawa and F. Nogata. *Bending Reponse of Dehydrated Ion Exchange Polymer Membranes to the Applied Voltage*. Journal of Membrane Science, 2004, **243**.

39. S. Nemat-Nasser and S. Zamani. *Effect of Solvents on the Chemical and Physical Properties of Ionic Polymer-Metal Composites*. Journal of Applied Physics. 2006, **99.**

40. M.D. Bennett and D.J. Leo. *Ionic liquids as stable solvents for ionic polymer transducers*. Sens. Actuators A: Phys., 2004, **115** (2004).

41. D.J. Segalman, W.R Witkowski, D.B. Adolf, and M. Shahinpoor. *Theory and Application of Electrically Controlled Polymeric Gels*. Smart Mater. Struct., 1992, **1**.

42. H. Li, R. Luo, E. Birgersson, and K.Y. Lam. *Modeling of multiphase smart hydrogels responding to pH and electric voltage coupled stimuli*. Journal of Applied Physics, 2007, **(101)**.

43. Wei, Z. G., Sandstrom, R., and Miyazaki, S. *Shape-Memory Materials and Hybrid Composites for Smart Systems*. J. Mater Sci., 1998, **33**.

44. Schmidt, A. M. *Electromagnetic Activation of Shape Memory Polymer Networks Containing Magnetic Nanoparticles*. Macromol. Rapid Commun., 2006, **27**.

45. Merx, K., *GM's Grand Experiment: Miracle Materials,* Detroit Free Press, Detroit MI., 2007.

46. K.E. Gross. *Mechanical Characterization of Shape Memory Polymers To Assess Candidacy As Morphing Aircraft Skin*. 2008, University of Pittsburgh.

47. Robert S. Bortolin. *Characterization of Shape Memory Polymers for Use as A Morphing Aircraft Skin Material*. 2005, University of Dayton.

48. The Engineering Toolbox, Elastic Properties and Young's Modulus of Some Materials. [cited; Available from http://www.engineeringtoolbox.com/young-modulus-d_417.html.

49. S. Nemat-Nasser, J. Yu Li. *Electromechanical Response of Ionic Polymer-Metal Composites*. J. of Applied Phys., 2000, **87** (7).

50. J.E. Mark and J.G. Curro. *A Non-Gaussian Theory of Rubberlike Elasticity Based on Rotational Isomeric State Simulations of Network Chain Configurations. I. Polyethylene and Polydimethylsiloxane Short-Chain Unimodal Networks*. J. Chem. Phys., 1983, **79**(11).

51. Q.W. Yuan, A. Kloczkowski, J.E. Mark, and M.A. Sharaf. *Simulations on the Reinforcement of Poly(dimethylsiloxane) Elastomers by Randomly Distributed Filler Particles*. J. Polym. Sci., Part B: Polym. Phys., 1996, **34**.

52. M.A. Sharaf and J.E. Mark: *Monte Carlo Simulations on the Effects of Nanoparticles on Chain Deformations and Reinforcement in Amorphous Polyethylene Networks*. Polymer, 2004, **45**.

53. L.R.G. Treloar. *The Physics of Rubber Elasticity.* 3rd ed., 1975, Clarendon Press.